Dynamic enhancement and multi-axial behavior of honeycombs under combined shear-compression
Bing Hou

▶ To cite this version:

HAL Id: tel-00675750
https://theses.hal.science/tel-00675750

Submitted on 1 Mar 2012

**THESE DE DOCTORAT
DE L'ECOLE NORMALE SUPERIEURE DE CACHAN**

Présentée par

Mademoiselle HOU Bing

pour obtenir le grade de

DOCTEUR DE L'ECOLE NORMALE SUPERIEURE DE CACHAN

Domaine :

MÉCANIQUE-GÉNIE MÉCANIQUE-GÉNIE CIVIL

Sujet de la thèse :

Comportement multiaxiale des nids d'abeilles sous sollicitations dynamiques

Thèse présentée et soutenue à Xi'an le 26 Mars, 2011 devant le jury composé de :

Guoxing Lu	Nanyang Tech. University, Singapore	Rapporteur
Eric Markiewicz	Université Valenciennes	Rapporteur
Tiejun Wang	Xian Jiaotong University	Examinateur
Weihong Zhang	Northwestern Polytech. University	Examinateur
Yulong Li	Northwestern Polytech. University	Directeur de thèse
Han Zhao	Université Pierre et Marie Curie	Directeur de thèse

Dynamic enhancement and multi-axial behavior of honeycombs under combined shear-compression

Dissertation submitted to

Ecole Normale Supérieure de Cachan

and

Northwestern Polytechnical University

In Partial Fulfillment of the Requirements

For the Degree of Doctor of Philosophy

by

Bing HOU

Doctoral committee

Guoxing Lu	Nanyang Tech. University, Singapore	Rapporteur
Eric Markiewicz	Université Valenciennes	Rapporteur
Tiejun Wang	Xian Jiaotong University	Examinateur
Weihong Zhang	Northwestern Polytech. University	Examinateur
Yulong Li	Northwestern Polytech. University	Directeur de thèse
Han Zhao	Université Pierre et Marie Curie	Directeur de thèse

Laboratoire de Mécanique et Technologie
ENS Cachan/CNRS/UMR
61, avenue du Président Wilson, 94235 CACHAN CEDEX (France)

Acknowledgements

First of all, I would like to express the deepest gratitude to my two advisors, Professor Han Zhao in LMT-Cachan and Professor Yulong Li in NPU, for everything that they have done to help me get to where I am. I will forever appreciate their patience in teaching me from ABC, the wonderful instructions in science research as well as the caring advice for career and life.

I want to extent my thanks to my colleagues in LMT and NPU. I would like to thank Stephane Pattofatto, Dominique Saletti and Huabin Zeng for their help and also the great time to be with them during my stay in France. I'm also grateful to the group members in NPU, China, who have accompanied me for such a long time and encouraged me at any time I needed.

I also must show my appreciation to the financial support from China Scholarship Council to provide me the opportunity to study abroad. Thanks to LMT-Cachan for the kind reception and the convenience they provided to perform the research work. Thanks to 111 project of China for funding the cooperations between NPU and LMT.

I could never thank enough my family who continually supported this long journey. I could not have finished this without their love and encouragements.

Finally, I would also like to thank my doctoral committee for their assistance and suggestions.

Abstract:

This study aims at the energy absorption problems in the crash of high speed vehicles, bird impact and crashworthiness design of aircraft, and the dynamic enhancement and multi-axial behavior of honeycombs under combined shear-compression are investigated.

The study consists mainly of two parts. The first part is related to the dynamic strength enhancement of honeycombs under uniaxial compression. We firstly study this particular phenomenon of thin-walled structure by establishing three micro-size FE models in order to validate the adaptability of an inertia effect model in explaining the dynamic enhancement of micro-size thin-walled structures. Further more, the dynamic enhancement of a series of honeycombs with different cell-size, cell-wall thickness and base material is studied experimentally and the influence of these geometric parameters and the base material on honeycomb strength as well as the dynamic enhancement rate is investigated.

The second part of this study concerns the biaxial behavior of honeycombs under combined shear-compression. We firstly present a combined dynamic shear-compression loading device basing on a large-diameter Nylon Split Hopkinson Pressure Bar system (SHPB). The measuring and data processing methods are studied and validated by the full-size FEM simulation on the whole loading process. Then, a series of experiments on an aluminium honeycomb is performed with loading angles ranging from 0° (corresponding to the pure compression) to 60° both dynamically and quasi-statically. It shows a strong effect of the additional shear loading to honeycomb overall strength, where, both the initial peak and the crush strength decrease with increasing loading angles. A notable strength enhancement under impact loading is observed for all the honeycomb specimens. Images captured during quasi-static and impact tests permit for the determination of the two co-existing deforming patterns under combined shear-compression and also for indicating the influence of loading rate on the occurrence of these two patterns. Finally, the combined shear-compression tests on honeycombs are reproduced by a numerical virtual model and the separated normal and shear behaviors of honeycombs under combined shear-compression are obtained. It is found that the normal strength of honeycomb decreases with increasing shear loading and the shear strength behave in an opposite way. A significant dynamic strength enhancement found in experiments was validated again in the numerical work. A crushing envelope in normal strength vs. shear strength plane was obtained

on the basis of these simulations, which shows an isotropic expansion behavior from the quasi-static loading to the dynamic loading.

Key words: cellular material, honeycomb, dynamic enhancement, combined shear-compression, Hopkinson bars

Résumé:

Cette étude s'adresse à des problèmes d'absorption d'énergie dans le crash de véhicules à grande vitesse ou l'impact d'oiseaux et l'écrasement d'avions. L'élévation de comportement dynamique et comportement multiaxiale des nids d'abeilles sous cisaillement-compression combiné est étudiée.

Cette étude se compose de deux parties. La première partie est liée à L'élévation de comportement dynamique de nids d'abeilles en compression uniaxiale. Nous avons premièrement étudié ce phénomène particulier en établissant trois FE modèles en micro-taille et l'adaptabilité d'un modèle d'inertie pour expliquer l'élévation de comportement dynamique des structures à paroi mince en micro-taille est validée. Ensuite, L'élévation de comportement dynamique d'une série de nids d'abeilles avec des cellules de tailles et d'épaisseur des parois différentes et de matériau de base différent est étudiée expérimentalement. L'influence de ces paramètres géométriques et le matériau de base sur la force en nid d'abeilles ainsi que le taux de l'élévation est étudiée.

La deuxième partie de cette étude concerne le comportement biaxial de nids d'abeilles sous cisaillement-compression combinés. Nous présenterons tout d'abord un dispositif pour charger le cisaillement-compression combiné se basant sur un système des barres de Hopkinson viscoélastiques de grand diamètre (60 mm). Les méthodes de traitement les données sont étudiées et validées par la simulation de FE modèle en pleine dimension sur le processus de chargement entier. Ensuite, une série d'essais sur un nid d'abeille en aluminium sont réalisées avec les angles de chargement allant de 0° (correspondant à la compression pure) à 60o dynamiquement et quasi-statiquement. Il montre un fort effet de la charge de cisaillement supplémentaire à la résistance globale du nid d'abeille. Le pic initial et la résistance à l'écrasement diminuent évidemment avec l'augmentation de l'angle de chargement. Une élévation de la résistance sous chargement d'impact est observée pour tous les échantillons sous les conditions différentes de cisaillement-compression combiné. Les images capturées lors des essais quasi-statique et dynamique permettent de la détermination des deux déformations modèles coexistant sous cisaillement-compression combiné et révèlent l'influence de la vitesse d'impact sur la présence de ces deux modèles. Enfin, les tests de cisaillement-compression sur des nids d'abeilles sont reproduites virtuellement par un modèle numérique. Les comportements normaux et de cisaillement du nid d'abeille sous cisaillement-compression combinés sont séparés. Il se trouve que la force

normale du nid d'abeille diminue avec l'augmentation de l'angle de chargement et la résistance au cisaillement se comporte de manière inverse. L'élévation de la résistance dynamique observée dans les essais est validée à nouveau dans le travail numérique. Une enveloppe de crush dans le plan de la force normale vs la force du cisaillement a été obtenue sur la base de ces simulations, qui montre un comportement de dilatation isotrope du chargement quasi-statique au chargement dynamique.

Mots clés: matériau cellulaire, nid d'abeilles, l'élévation dynamique, cisaillement-compression combinée, barres de Hopkinson

TABLE OF CONTENTS

Chapter 1 Introduction

1.1 Research background

Cellular materials are defined by Gibson and Ashby in their book[1] as 'one made up of an interconnected network of solid struts or plates which form the edges and faces of cells'. The commonly used cellular materials include woods, honeycombs, metallic and polymeric foams etc. Figure 1.1 (a) shows the assembly of several kinds of metallic and polymeric cellular materials (honeycomb, foams and hollow sphere agglomerates) and Figure 1.1 (b) shows four kinds of honeycombs with different cell geometry and made of different base materials. Cellular materials have been widely used in many industrial areas because of their excellent physical and mechanical properties, i.e. improved strength/weight ratio, high stiffness in bending and outstanding capabilities in reducing noise, insulating heat and absorbing energy.

(a)
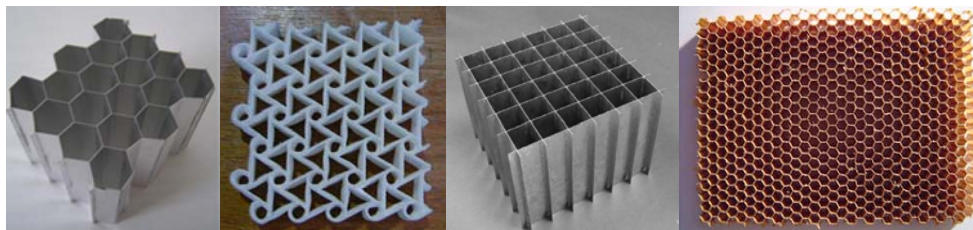
(b)

Figure 1.1 Cellular materials (a) and honeycombs (b)

In the field of mechanics, cellular materials are usually employed to improve the weight/strength ratio for applications as in railway, automotive and aircraft industries. With regard to this aspect, interests focus on the mechanical behavior for small deformations (elastic behavior and failure strength). Analytical and experimental works have been performed under various loading conditions with respect of the anisotropic nature of honeycombs. The theoretical work is based mainly on a micromechanical analysis to derive global cellular structure response from the study of a single cell[2]. Elastic and fracture models for out-of-plane crushing[3], and in-plane crushing[4], as well as for transverse shearing[3, 5], have been developed. Related topics such as fracture detection using elastic waves[6], negative Poisson's ratio honeycombs[7], and foam-filled honeycombs[8], have also been reported in the open literature.

While on the other hand, cellular materials are also used to absorb energy in accidental impacts, for example, in the unexpectable crash of high speed vehicles, in the bird impact design of aircrafts as well as the crashworthiness design of airframes etc. In such uses, the behavior of large deformation (up to 80%) is desired. Under quasi-static assumptions, many research works are performed in the past decades. While under dynamic loading, which is the real working condition for energy absorbing systems made of cellular materials, some investigations limited to uniaxial compression are reported in the open literatures[9-11].

It is found in many reported works that the strength of honeycombs under uniaxial dynamic compression is higher than under quasi-static loading[9-15], showing an obvious dynamic enhancement effect. As the impact velocity increases, some special phenomenon like shock wave effect will come forth[13, 16-27]. This dynamic enhancement feature of cellular material behavior will play an important role in the applications as energy absorber under dynamic loading, while unfortunately, up to now, the mechanism of this dynamic enhancement remains still unclear.

Actually, in the energy absorption applications, the cellular materials are not always found under unixial compression, but mostly under biaxial loading such as combined shear-compression. Firstly, this is because of the uncertainty of impact loads in accidental crash. Secondly, the components of an energy absorber are always designed with complicated shapes which results in inhomogeneous deformation and stress distribution. Finally, some cellular materials are naturally anisotropic. For example, honeycombs have out-of-plane direction much stronger than the other two

in-plane directions. Thus, it is not enough for understanding and predicting the energy absorbing characteristics of cellular material by only knowing the uniaxial compression or tension behavior, and the multi-axial experiments are required.

1.2 Research progresses

1.2.1 Dynamic enhancement of cellular materials

In the past decades, many experimental and numerical studies on the deformation mechanism, damage revolution and macro-constitutive equations are performed under quasi-static loading. For metallic honeycombs, Wierzbicki[28] has developed an out-of-plane large deformation crushing model that gives an analytical prediction of the crush pressure; Klintworth and Stronge[29] have formulated a large deformation behavior of the in-plane crushing that takes account of the localized deformation band effects. Mohr and Doyoyo[30] studied the out-of-plane crush behavior and proposed a criterion for plastic collapse initiation and propagation. As to the isotropic metallic foams, Gibson and Ashby[2] presented two micro-models for predicting the elastic properties and yielding behavior of open and close foams analytically. Based on their FE simulation results, Deshpande and Fleck[31] obtained an isotropic constitutive model at macroscopic level to describe the large deformation behavior of this kind of material.

Further investigations on cellular materials under dynamic loading indicate that these materials show some extent of strength enhancement with increasing loading rate. For examples, Goldsmith and Sackman[11] have reported some experimental works on out-of-plane crushing and on the ballistic perforation of honeycombs. They have fired a rigid projectile to a target made of honeycombs and have shown that the mean crushing pressures sometimes increase up to 50% with respect to the static results. Wu and Jiang[9], Baker et al[12], Zhao and Gary[10], Zhao et al[15], Harrigan et al[13] and Zhou and Mayer[17] have also found the similar phenomenon for metallic honeycombs. As to the isotropic foams, Deshpande and Fleck[32] studied the dynamic behaviors of Alulight and Duocel by Hopkinson experiments, and no significant loading rate effect is found for these two foams which may be due to the large scatter of data. Mukai and Kanahashi[33] have investigated Alporas foams using also a standard SHPB arrangement and reported significant rate sensitivity. Dannemann and Lankford[34] also reported rate sensitive results for Alporas foam.

For the cases under moderate impact velocities, it is of preference to attribute this strength enhancement to the inertia effect. The early theoretical work in this domain was reported by Budiansky and Hutchinson[35]. Gary[36] showed experimentally that the buckling of a column under compressive impact occurs at a larger strain and a higher force because of lateral inertia. Calladine and English[37], Tam and Calladine[38] explained in detail the role of lateral inertia in dynamic enhancement by identifying two genetic types (type I and type II) of plastically deforming structures in energy-absorbing situations. Gao et al [39, 40] studied in detail the deformation behaviors of these two structures. These two types of basic structure were used by many researchers to explain the dynamic enhancement of cellular materials. Reid and Peng[16] and Su et al[41, 42] employed it to explain the dynamic enhancement of wood. Zhao and Gary[10] found in their Hopkinson experimental results that the out-of-plane strength of honeycomb increased by 40% when the loading rate increased from 5×10^{-4}m/s to 30m/s, but the enhancement of in-plane strength was insignificant。 They explained that when honeycombs were under out-of-plane compression, they were classified into the type II structure which has a steeply falling curve, and the effect of inertia is important, while for the in-plane loading, honeycombs were similar to type I structure with a relatively flat-topped curve, and the effect of inertia is limited. Deshpande and Fleck[43] took the aluminium foams as Type I structures to explain the insignificant strength enhancement under dynamic loading. Basing on the concept of Type I and Type II structures, Zhao[44] proposed a mechanism of dynamic enhancement for thin-wall structures basing on the lateral inertia protecting effects and successfully applied it to the square tube under dynamic crushing.

When under relative high impact velocity (>50m/s), Harrigan et al[13] and Reid and Peng[16] observed in wood the significant dynamic enhancement induced by shock wave effect. In their experiments, the wood projectile was launched at a velocity of 250m/s to impact the target, and a Hopkinson bar was fixed behind the target for data measuring. A simple RPPL model was proposed by them to analyze the propagation process of shock wave. Tan and Harrigan[18] confirmed this shock wave theory in their experiments on Cymat and determined the critical impact velocity for the appearance of shock wave, which was between 44m/s and 108m/s. Lopatnikov and Gama[21] employed the so called Taloy-Hopkinson apparatus to perform the shock wave experiments on a closed-cell aluminium foam under impact velocities from 26m/s to 200m/s. Further investigations by Lopatnikov and Gama[22] divided the impact

velocity into four ranges to illustrate the conditions for generating shockwave, and the deformation and energy absorbing properties of cellular materials in range 2 and range 3 were presented. Radford and Fleck[23] studied the initiation and propagation of shock wave in aluminium foam by launching a foam projectile to impact the Hopkinson bar as well as a free mass. The influences of impact velocity, projectile length and the density of foams on shock wave were also included. Basing on the direct impact Hopkinson bars, Elnasri et al[24] and Pattofatto et al[25] designed new experiments with two different configurations which can be used to measure respectively the information before and behind shock wave front. Their experimental results confirmed the existence of shock wave in alumimun foams and the shock wave speed was also estimated. Zou et al[26] investigated the in-plane behavior of honeycombs under high impact velocity (about 100m/s) by FEM and the shock wave effect was well studied. Liu et al[27] performed similar works by FEM to investigate the shock wave effect in cellular materials.

In Reid and Peng's one-dimensional shock model, a rigid-perfectly-plastic locking (RPPL) shock model (as shown in Figure 1.2(a)) is employed for the cellular material. The plateau stress $\sigma_{plateau}$ and densified strain ε_d are two key parameters to determine the model properties. When the impact loading is applied on one end of specimen at velocity V, the assumption of RPPL behavior makes the cellular material to reach densification very easily, and then a shock front within the material initiates. The material ahead of the shock front keeps untouched by the shock wave and is with the initial stress of $\sigma_{plateau}$, density of ρ_0 and particle velocity of zero. While for the material behind the shock front, the quantities jump to be σ_d, ρ_d in densified stage and the particle velocity takes the same value to the impact velocity V (as shown schematically in Figure 1.2(b)).
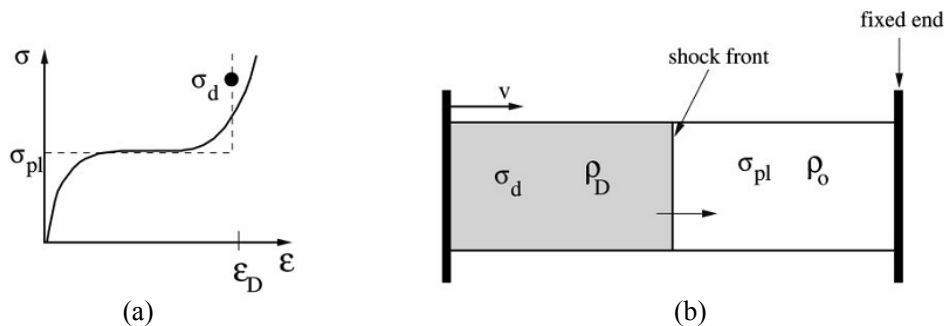
Figure 1.2 One-dimensional shock wave model (a) and its propagation (b)

Furthermore, from the Rankine-Hugoniot jump conditions through this shock front, the conservation of mass, and kinematics quantities read:

$$\rho_d(U - V) = \rho_0 U \qquad\qquad 1.1$$

$$\sigma_d - \sigma_{plateau} = \rho_0 U V \qquad\qquad 1.2$$

where U is the speed of shock front propagation. Notice that

$$\varepsilon_d = 1 - \frac{\rho_0}{\rho_d} \qquad\qquad 1.3$$

Thus, from the shock wave theory of Reid and Peng[16], the dynamic enhancement value $\Delta\sigma$ of cellular materials induced by shock wave can be calculated as:

$$\Delta\sigma = \sigma_d - \sigma_{plateau} = \frac{\rho_0 V^2}{\varepsilon_d} \qquad\qquad 1.4$$

There is another theory of compressed air pressure for explaining the dynamic enhancement of cellular materials. It is believed that dynamic tests on cellular materials are associated with the compression of air trapped in the cells; there is insufficient time for the air to escape when the loading rate is very high. Gibson and Ashby[1] have calculated the contribution of air compression to the strength of the closed-cell foams. Zhou and Mayer[17] also suggested that the air trapped in the honeycomb cells could be the main reason for the increased crush strength.

According to Gibson and Ashby's[1] calculation, the contribution of compression of the air to the strength of the cellular materials by assuming an ideal gas under isothermal compression is:

$$\Delta\sigma = \frac{p_0 \varepsilon_B (1 - 2v)}{1 - \varepsilon_D (1 - 2v) - \rho/\rho_S} \qquad\qquad 1.5$$

where, p_0 is the atmospheric air pressure, ε_D is the densification strain and v is the plastic Poisson's ratio of the foam. A similar calculation assuming adiabatic compression gives:

$$\Delta\sigma = p_0 \left[\left(\frac{1 - \rho/\rho_S}{1 - \varepsilon_D (1 - 2v) - \rho/\rho_S} \right)^{\gamma} - 1 \right] \qquad\qquad 1.6$$

where γ is the ratio of the specific heat capacities, with $\gamma = 1.4$ for air.

It is of great importance to investigate the dynamic enhancement of cellular materials for well understanding their behaviors in the use of energy absorbing designs. However, up to now, this problem keeps still an open field. The experimental data is limited and some studies even present incompatible results. For example, Hall

et al[45] and Zhao et al[15] tested the same 6061 aluminium foams and obtained nearly opposite conclusions. Moreover, the mechanism of this dynamic enhancement remains still unclear, and the existent explanations are more or less on the basis of assumptions rather than on experimental observations.

It should be noticed that the aforementioned works on dynamic enhancement of cellular materials are all under uniaxial loading. While for the multi-axial dynamic loading which is closer to the real working condition for energy absorbing uses, rare literatures are available as yet. In fact, even studies on the experimental methods for achieving dynamic multi-axial loading are rarely reported. In this paper, we studied at first the uniaxial dynamic enhancement of honeycombs by experiments and simulations, and then a new biaxial loading method based on large diameter Nylon Hopkinson bars is presented which enables further investigations on the multi-axial dynamic enhancement of honeycombs.

1.2.2 Progresses on multi-axial loading techniques

In the past decade, various multi-axial quasi-static loading methods suitable for cellular material were developed[46-58]. For example, Zhang and Ashby[3] studied separately the out-of-plane compressive and shear properties of Nomex honeycombs, but they didn't combine these two loading directions together and the experiments were actually not in real multi-axial loading. Papka and Kyriakides[46] employed a quasi-static biaxial loading machine to investigate the in-plane biaxial compression properties of honeycombs. In their facilities, the specimen was placed between four loading platens with two adjacent ones perpendicular to each other. Two adjacent platens could move independently in two orthogonal directions, while the other two are fixed and connected with load cells. Chung and Waas[47] designed a similar multi-axial loading system with Papka and Kyriakides[46], but the biaxial compressions were applied in two in-plane directions in tandem. They firstly compressed the honeycomb specimen in one direction while keeping the other one deforming freely. Then, compression in the other direction was applied and the former applied load was held constantly. Deshpand and Fleck[43] presented two multi-axial loading systems to investigate the multi-axial yielding behavior of polymer foams. One can be used to apply the tension or compression in axial direction and hydrostatic loading in radial direction and the other for achieving biaxial and hydrostatic tension test. Karagiozova and Yu[48] studied the in-plane biaxial behaviors of honeycombs by using a HKUST

biaxial loading device. Ruan et al[49] performed the triaxial compression tests on CYMAT closed-cell aluminium foams to investigate their initial failure surfaces under multiaxial compressive loading. Chen and Fleck[50] employed Arcan apparatus to investigate the combined shear-compression behavior of metallic foams. Mohr and Doyoyo[51] modified the standard Arcan apparatus using a clamped configuration to restrict the rotations of the grips and tested the combined out-of-plane shear-compression behavior of honeycombs. They estimated possible errors of ignoring the additional horizontal force produced by the clamped configuration[52] and integrated another load cell to measure it. Mohr and Doyoyo[30] also had another universal biaxial testing device which employed three load cells to measure the forces in two different directions. Based on a Zwick static test facility, Kintscher et al[53] developed a test device with the combination of a roll and a steel towing rope to apply combined out-of-plane shear-compression to a folded sandwich double-core specimen. Hong et al established two systems (so-called the independently controlled test fixture[54] and the inclined test fixture[55]) to perform the quasi-static biaxial experiment on honeycombs. These quasi-static biaxial loading methods succeed in measuring the in-plane biaxial or combined out-of-plane shear-compression behavior of honeycombs by using more than one load cell. But these methods may encounter great difficulties in migrating into dynamic loading conditions.

As to dynamic multi-axial experiments, the available referencing works are very limited. The main reason for such situations lies in the difficulties to perform dynamic multi-axial experiments because of the requirements for both a feasible multi-axial design in a tiny limited space and an accurate data measurement under these conditions. Some studies using the drop-weight or direct impact methods have been reported. For example, Chung and Waas[47] introduced biaxial loading by restricting the transversal displacement of the specimen while dropping the weight. The only found combined dynamic out-of-plane shear-compression test on honeycomb was achieved by Hong et al[55]. They designed an impact test fixture based on their quasi-static method to introduce combined dynamic shear-compressive loading. The projectile was designed to strike a complex load transfer unit in order to generate a nearly constant loading velocity. A multi-axial load cell was used to measure the normal and shear loads applied to the specimen. These methods in a drop-weight frame or high speed testing machine system might suffer from a rather poor measurement accuracy at higher loading rates.

It is well known that the Split Hopkinson Pressure Bar (SHPB) technique provides a more precise method for testing the material behavior under high loading rates. This universal experimental technique provides nearly constant loading velocities during the test, which is different to that of aforementioned works. With semicentennial development, Hopkinson bar technique is not only used for standard uniaxial test, but also can be modified and adapted to develop multi-axial dynamic testing in many special cases[56-63]. For examples, Gary and Bailly[56] presented a testing device for the experimental study of dynamic compaction of concrete based on large diameter (80mm) Hopkinson bars where the specimen is confined on the lateral surface by a metallic ring. McGee and Nemat-Nasser[57] employed similarly the constraining ring on traditional SHPB for pre-compression in radial directions while performing the compressive experiments on woven composites. Chen and Ravichandran[58] took also this method for testing the biaxial dynamic response of ceramics with lateral confinement. Rittel et al[59] invented a shear-compression specimen for Hopkinson pressure bars. The specimen is modified from a classical cylinder shape in which two diametrically opposed slots are machined at 45° with respect to the longitudinal axis and complicated stress state is achieved in the region of slots. Nie et al[60] designed an inclined specimen in Hopkinson Pressure Bars to introduce shear. Huang and Feng[61] installed a compression-torsion loading system basing on the Torsion Split Hopkinson Bar (TSHB)[62].

The above-mentioned methods basing on Hopkinson technique are designed mostly for solid materials. While for soft cellular materials, many specific problems will come forth. First, the measuring accuracy of SHPB depends on the amplitude of waves in the bars related to the resistance of the specimen. It is well known that cellular materials are very weak (for example, the strength of honeycomb is only several MPa), which produces very small strain signal in the output bar. Second, cellular materials have inhomogeneous micro-structures and the specimen should include enough unit cells to reduce as much as possible data scatter in measurements, thus, large diameter bars are desired to hold large size specimen. In order to get an accurate measurement, the use of large diameter, low impedance bars is proposed by Zhao et al[63] which can provide reliable data with good reproducibility and an improvement of impedance of about 200 times than that of a classical steel bar. This paper presents a bran-new dynamic biaxial loading method to achieve combined shear-compression on cellular materials with the use of large diameter soft Hopkinson

bars. Validating work by FEM and the experiments performed on honeycombs show that this dynamic biaxial loading method is feasible and reliable.

1.2.3 Multi-axial behavior of honeycombs

Honeycomb as one of the most common cellular materials is characterized by its obvious anisotropic properties. In the past decades, people studied a lot the in-plane and out-of-plane compressive responses of honeycombs experimentally and numerically, but most of these works were concentrated in quasi-static and uniaxial loading condition[1,64-66].

For the multi-axial behaviors, Gibson and Ashby[1] gave in their book the five elastic constants to describe the shear-compressive elastic behavior of honeycombs. The elastic buckling and brittle failure behaviors of honeycomb were also discussed. Klintworth and Stronge[67] proposed a macroscopic elasto-plastic yielding criteria for transversely crushed honeycombs. Yang and Huang[68] suggested an in-plane failure mechanism of honeycombs basing on their FE simulating results. Papka and Kyriakides[46] found from their in-plane biaxial compression experiments and simulations that the biaxial behaviors of honeycomb is much more complicated than the uniaxial compression, and the deforming mode is affected significantly by the biaxial loading states. Chung and Waas[47] applied the biaxial loading in two in-plane directions in tandem and found that the elastic modulus of in-plane compression increased when the other in-plane direction is pre-compressed. Besides, the local buckling of honeycomb changes into a mixed mode and the localization of buckling becomes more and more obvious with increasing pre-compression in the other direction. Hong et al[54] derived a quadratic yield criterion suitable for orthotropic materials by modifying Hill's quadratic yield criterion. They also analyzed in detail the microscopic crushing mechanism of honeycombs under combined loading conditions. Mohr and Doyoyo[69, 70] performed the out-of-plane combined shear-compression experiments on honeycombs by modifying Arcan apparatus and obtained the initial yield envelope and the crushing envelope at large deformation period. They also illustrated the deformation mechanism and the failure modes of honeycombs and suggested a linear fit for the crushing envelope based on their quasi-static calculating results.

As to the dynamic multi-axial behaviors of honeycomb, it is rarely reported in open literatures. The main reason as explained above is due to the lack of a feasible

dynamic multi-axial loading method. However, the research work on dynamic uniaxial compression behavior of honeycombs revealed that the strength of honeycomb displays a significant enhancement under higher loading rates. Thus, it can be imagined that the multi-axial behavior will also be influenced by loading rate and it is of great importance to pay attention to the dynamic multi-axial behaviors as well as the yielding criteria and crushing envelopes of honeycomb.

Among the limited research works on dynamic multi-axial behaviors of honeycombs, Chung and Waas[47] presented the in-plane failure envelopes of honeycombs under in-plane biaxial compression which are useful towards the development of an orthotropic continuum description of honeycombs response at macroscopic level. Hong et al[55] performed the dynamic shear-compression experiments on honeycomb at different loading states and loading velocities and the relationship between force-displacement curve and loading velocity is determined. By modifying the quasi-static biaxial yielding criteria, a macroscopic dynamic yielding criterion containing biaxial loading states is proposed.

Basing on the experimental results of honeycombs under combined shear-compression achieved by our new designed dynamic biaxial loading device, we performed further the virtual tests by means of FEM simulations in order to study in detail the biaxial behavior of honeycombs. The deformation mode and dynamic enhancement effect of honeycombs under combined shear-compression were obtained. Such virtual tests also provide separated normal and shear behaviors of honeycomb specimen, which allows for the determination of the yield envelope depicted in terms of the macroscopic shear strength vs. compressive strength.

1.3 Outline of dissertation

This thesis is mainly composed of two parts. The first part focuses on the dynamic enhancement effect of cellular materials which includes Chapter 2 and 3, where Honeycombs as well as some other thin-wall structures are investigated experimentally and numerically. Chapter 2 is going to study the dynamic enhancement of cellular materials by simulating the collapse behavior of three kinds of thin-walled structures with FEM. The mechanism of dynamic enhancement basing on lateral inertia effects is examined in detail. Chapter 3 introduced firstly the large diameter viscoelastic Hopkinson technique including the method of wave dispersion correction as well as the data proceeding method suitable for cellular materials, and

then the dynamic enhancement of 6 types of honeycombs under uniaxial compression and the influences of cell-size, cell-wall thickness and base materials on the dynamic enhancement of honeycombs were investigated.

The second part of this study refers to a new designed biaxial loading device with the use of a large-diameter Nylon Split Hopkinson Pressure Bar system (SHPB). The biaxial behavior of honeycombs under combined shear-compression is investigated with the combination of experimental works and simulations. Chapter 4, 5 and 6 are included in this part. In Chapter 4, the new designed dynamic biaxial loading device is presented as well as the validating work by full-size FEM simulation of the loading process. Chapter 5 shows the experimental results on 5052 aluminium honeycombs by using this biaxial loading device. The biaxial behaviors and deformation modes of honeycombs under different combined shear-compression loading states are obtained and the influences of loading angle on them are analyzed. Chapter 6 tries to describe the biaxial behavior of honeycombs by FEM simulations. The calculating results from the detailed honeycomb models are ensured to be in good agreements with the experimental results in terms of overall pressure/crush curves and deformation modes. Basing on the calculation results, the separated normal and shear behaviors of honeycomb under combined shear-compression as well as the macroscopic crush envelope are obtained. The experimental method presented in Chapter 5 and the numerical method in Chapter 6 supplement each other to provide a feasible way for investigating the biaxial behavior of honeycombs under dynamic combined shear-compression.

References

[1]   L. J. Gibson, M. F. Ashby. Cellular material: structure and properties, 2nd Ed., Cambridge University Press, Cambridge, UK. (1997).

[2]   L. J. Gibson, M. F. Ashby. Cellular Solids. Pergamon Press, Oxford, (1988).

[3]   J. Zhang, M. F. Ashby. The out-of-plane properties of honeycombs. Int. J. Mech. Sci. 34, 475-489 (1992).

[4]   J. Zhang, M. F. Ashby, Buckling of Honeycombs under in-plane biaxial stresses. Int, J. Mech. Sci. 34, 491-509 (1992)

[5]   G. Y. Shi, P. Tong, Equivalent transverse shear stiffness of honeycomb cores. Int. J. Solids Struct. 32, 1383-1393 (1995).

[6]   S. Thwaites, N. H. Clark. Non-destructive testing of honeycomb sandwich structures using elastic waves. J. Sound Vibration, 187, 253-269 (1995).

[7]   D. Prall, R. S. Lakes, Properties of chiral honeycomb with a Poisson's ratio of -1, Int. J. Mech. Sci. 39, 305-314 (1997).

[8]   C. L. Wu, C. A. Weeks, C. T. Sun, Improving honeycomb-core sandwich structures for impact resistance. J. Adv. Mater. 26, 41-47 (1995).

[9]   E. Wu, W. S. Jiang, Axial crush of metallic honeycombs, Int. J. Impact Engng. 19, 439-456 (1997).

[10]   H. Zhao, G. Gary, Crushing behavior of aluminium honeycombs under impact loading. Int. J. Impact Engng. 21, 827-836 (1998).

[11]   W. Goldsmith, J. L. Sackman, An experimental study of energy absorption in impact on sandwich plates. Int. J. Impact Engng. 12, 241-262 (1992).

[12]   W. E. Baker, T. C. Togami, J. C. Weydert. Static and dynamic properties of high-density metal honeycombs. Int. J. Impact Engng. 21, 149-163 (1998).

[13]   J. J.Harrigan, S. R. Reid, C. Peng, Inertia effects in impact energy absorbing materials and structures. Int. J. Impact Engng. 22, 955-979 (1999).

[14]   W. Goldsmith, D. L. Louie, Axial perforation of aluminium honeycombs by projectiles. Int. J. Solids Struct. 32, 1017-1046 (1995).

[15]   H. Zhao, I. Elnasri, S. Abdennadher. An experimental study on the behavior under impact loading of metallic cellular materials. Int. J. Mech.Sci. 47, 757-774 (2005).

[16]   S. R. Reid, C. Peng, Dynamic uniaxial crushing of wood. Int. J. Impact Engng. 19, 531-570 (1997).

[17]   O. Zhou, R. R. Mayer, Characterization of aluminium honeycomb material failure in large deformation compression, shear and tearing. J. Engng. Mater. Tech. 124, 412-420 (2002).

[18]   P. J. Tan, J. J. Harrigan. Inertia effects in uniaxial dynamic compression of a closed cell aluminium alloy foam. Mater. Sci. Tech. 18, 480-488 (2002).

[19]   P. J. Tan, S. R. Reid. J. J. Harrigan, Z. Zou S. Li, Dynamic compressive strength properties of aluminium foams. Part I: experimental data and observations. J. Mech. Phy. Solids 53, 2174-2205 (2005).

[20]   P. J. Tan, S. R. Reid. J. J. Harrigan, Z. Zou S. Li, Dynamic compressive strength properties of aluminium foams. part II: shock theory and comparison with experimental data and numerical models. J. Mech. Phy. Solids 53, 2206-2230 (2005).

[21]   S. L. Lopatnikov, B. A. Gama. Dynamic of metal foam deformation during Taylor cylinder-Hopkinson impact experiment. Compos. Struct. 61, 61-71(2003).

[22]   S. L. Lopatnikov, B. A. Gama, High-velocity plate impact of metal foams. Int. J. Impact Engng. 30, 421-445(2004).

[23]   D. D. Radford, N. A. Fleck. The use of metal foam projectiles to simulate shock loading on a structure. Int. J. Impact Engng. 31, 1152-1171(2005).

[24]   I. Elnasri, S. Pattofatto, H. Zhao, H. Tsisiris, F. Hild, Y. Girard. Shock enhancement of cellular structures under impact loading: Part I Experiments. J. Mech. Phy. Solids 55, 2652-2671(2007).

[25]   S. Pattofatto, I. Elnasri, H. Zhao, H. Tsisiris, F. Hild, Y. Girard. Shock enhancement of cellular structures under impact loading: Part II analysis. J. Mech. Phy. Solids 55, 2672-

2686 (2007).

[26] Z. Zou, S. R. Reid, P. J. Tan, S. Li, J. J. Harrigan, Dynamic crushing of honeycombs and features of shock fronts. Int. J. Impact Engng. 36. 165-176 (2009).

[27] Y. D. Liu, J. L. Yu, Z. J. Zheng, J. R. Li, A numerical study on the rate sensitivity of cellular metals. Int. J. Solids Structs 46, 3988-3998 (2009).

[28] T. Wierzbicki. Crushing analysis of metal honeycombs. Int. J. Impact Engng. 1, 157-174 (1983).

[29] J. W. Klintworth, W. J. Stronge, Elasto-plastic yield limits and deformation laws for transversely crushed honeycombs. Int. J. Mech. Sci. 30, 273-292 (1988).

[30] D. Mohr, M. Doyoyo. Experimental investigation on the plasticity of hexagonal aluminium honeycomb under multi-axial loading. J. Appl. Mech. 71, 375-385 (2004).

[31] V. S. Deshpande, N. A. Fleck. Isotropic constitutive models for metallic foams. J. Mech. Phy. Solids. 48, 1253-1283 (2000).

[32] V. S. Deshpande, N. A. Fleck. High strain rate compressive behaviour of aluminium alloy foams. Int. J. Impact Engng. 24, 277-298 (2000).

[33] T. Mukai, H. Kanahashi, Experimental study of energy absorption in a closed cell aluminium foam under dynamic loading. Scripta Meterialia 40, 921-927(1999).

[34] K. A. Dannemann, J. Lankford, High strain rate compression of closed-cell aluminium foams. Mater. Sci. Engng. A 293, 157-164 (2000).

[35] B. Budiansky, J. W. Hutchinson, Dynamic buckling of imperfection sensitive structures. In: Proceedings of 11th international congress of Applied Mechanics. Springer Verlag. Munich (1964)

[36] G. Gary, Dynamic buckling of an elastoplastic column. Int. J. Impact Engng. 2, 357-375 (1983).

[37] C. R. Calladine, R. W. English. Strain-rate and inertia effects in the collapse of two types of energy-absorbing structures. Int. J. Mech. Sci. 26(11-12), 689-701(1984).

[38] L. L.Tam, C. R. Calladine. Inertia and strain rate effects in a simple plate structure under impact loading. Int. J. Impact Engng. 11, 689-701(1991).

[39] Z. Y. Gao, T. X. Yu, G. Lu, A study on type II structures. Part I: a modified one-dimensional mass-spring model. Int. J. Impact Engng. 31, 895-910 (2005).

[40] Z. Y. Gao, T. X. Yu, G. Lu, A study on type II structures. Part II: dynamic behavior of a chain of pre-bent plates. Int. J. Impact Engng. 31, 911-926 (2005)

[41] X. Y. Su, T. X. Yu, S. R. Peng. Inertia-sensitive impact energy-absorbing structures. Part I: Effects of inertial and elasticity. Int. J. Impact Engng. 16(4), 651 (1995).

[42] X. Y. Su, T. X. Yu, S. R. Peng. Inertia-sensitive impact energy-absorbing structures. Part II: Effects of strain rate. Int. J. Impact Engng. 16(4), 673 (1995).

[43] V. S. Deshpande, N. A. Fleck, Multi-axial yield behaviour of polymer foams, Acta Materialia 49, 1856-1866 (2001).

[44] H. Zhao, S. Abdennadher, On the strength enhancement under impact loading of square tubes made from rate insensitive metals. Int. J. Solids Struct. 41, 6677-6697 (2004).

[45] I. W. Hall, M. Guden, C. J. Yu, Crushing of aluminium closed cell foams: density and strain

rate effects. Scripta Materialia 43, 515-521 (2000).

[46]　S. D. Papka, S. Kyriakides. Biaxial crushing of honeycombs-Part I: Experiments. Int. J. Solids Struct. 36, 4367-4396 (1999).

[47]　D. Ruan, G. Lu, L. S. Ong, B. Wang, Triaxial compression of aluminium foams. Compos. Sci. Tech. 67, 1218-1234 (2007).

[48]　J. Chung, A. M. Waas. Compressive response of circular cell polycarbonate honeycombs under inplane biaxial static and dynamic loading. Part I:experiments. Int. J. Impact Eng. 27, 729-754 (2002).

[49]　D. Karagiozova, T. X. Yu. Strain localization in circular honeycombs under in-plane biaxial quasi-static and low-velocity impact loading. Int. J Impact Eng. 35, 753-770 (2008).

[50]　C. Chen, N. A. Fleck. Size effects in the constrained deformation of metallic foams. J. Mech. Phys. Solids 50, 955-977 (2002).

[51]　D. Mohr, M. Doyoyo. A new method for the biaxial testing of cellular Solids. Exp. Mech. 43, 2, 174-183 (2003).

[52]　D. Mohr, M. Doyoyo, Analysis of the Arcan Apparatus in the Clamped Configuration. J. Compos. Mater. 36, 22, 2583-1594 (2002).

[53]　M. Kintscher, L. Kärger, A. Wetzel D. Hartung. Stiffness and failure behaviour of folded sandwich cores under combined transverse shear and compression. Compos. Part A 38, 1288-1295 (2007).

[54]　S. T. Hong, J. Pan, T. Tyan, P. Prasad. Quasi-staitc crush behavior of aluminium honeycombs specimens under compression dominant combined loads. Int. J. Plasticity. 22, 73-109 (2006).

[55]　S. T. Hong, J. Pan, T. Tyan, P. Prasad. Dynamic crush behaviors of aluminium honeycomb specimens under compression dominant inclined loads. Int. J. Plasticity, 24, 89-117 (2008).

[56]　G. Gary, P. Bailly. Behaviour of quasi-brittle material at high strain rate, Experiment and modeling. Eur. J. Mech, A/Solids, 17, 3, 403-420 (1998).

[57]　J. D. McGee, S. Nemat-Nasser, Dynamic bi-axial testing of woven composites. Mat. Sci. Eng. A 317 135-139 (2001).

[58]　W. N. Chen, G. Ravichandran. Dynamic compressive failure of a glass ceramic under lateral confinement. J. Mech. Phys. Solids. 45, 1303-1328 (1997).

[59]　D. Rittel, S. Lee, G. Ravichandran. A shear-compression specimen for large strain testing. Exp. Mech. 42, 1, 58-64 (2002).

[60]　X. Nie, W. W. Chen, X. Sun, D. W. Templeton. Dynamic failure of borosilicate glass under compression/shear loading-experiments. J. Am. Ceram. Soc., 90 (8), 2556-2362 (2007).

[61]　H. Huang, R. Feng, A study of the dynamic tribological response of closed fracture surface pairs by Kolsky-bar compression-shear experiment[J]. Int. J. Solids Struct. 41, 2821-2835 (2004).

[62]　J. Duffy, J. D. Cambellm, R. H. Hawley, On the use of a Torsional Split Hopkinson Bar the study rate effects in 11000 Aluminum. J. Appl. Mech. 38, 83-91 (1971).

[63]　H. Zhao, G. Gary, J. R. Klepaczko. On the use of a viscoelastic splict Hopkinson pressure bar. Int. J. Impact Engng. 19, 319-330 (1997).

[64] T. Wierzbicki, J. Huang, Initiation of plastic folding mechanism in curshed box columns. Thin-Walled Structures 13, 115-143 (1991).

[65] D. Mohr, M. Doyoyo, Nucleation and propagation of plastic collapse bands in aluminium honeycomb. J. Appl. Phy. 94 ,4, 2262-2270 (2003).

[66] D. Karagiozova, T. X. Yu, Plastic deformation models of regular hexagonal honeycombs under in-plane biaxial compression. Int. J. Mech. Sci. 46, 1489-1515 (2004).

[67] J. W. Klintworth, W. J. Stronge. Elasto-plastic yield limits and deformation laws for transversly crushed honeycombs. Int. J. Mech. Sci. 30, 273-292 (1988).

[68] M. Y. Yang, J. S. Huang. Elastic buckling of regular hexagonal honeycombs with plateau borders under biaxial compression. Compo. Struct. 71, 229-237 (2005).

[69] D. Mohr, M. Doyoyo. Deformation-induced folding systems in thin-walled monolithic hexagonal metallic honeycomb. Int. J. Solids and Struct. 41, 3353-3377 (2004).

[70] D. Mohr, M. Doyoyo. Large plastic deformation of metallic honeycomb: Orthotropic rate-independent constitutive model. Int. J. Solids and Struct. 41, 4435-4456 (2004).

Part I Dynamic enhancement of honeycombs

Chapter 2 Dynamic enhancement mechanism of thin-walled structures

It is found in experiments that the strengths of honeycombs and some other cellular materials (like metallic foams) may be enhanced at dynamic loading rates comparing with quasi-static ones. As so far, there exist mainly three explanations to this phenomenon, e.g. the shock wave effect[1-12], the compressed air theory[13-15] and the lateral inertia effect[16-25]. Among these explanations, the shock wave effect is adapted to the much high impact loading velocity (e.g. >100m/s), and is unsuitable for the cases of energy absorbing applications, where moderate loading velocities (<50m/s) are of concern. The compressed air theory can explain in some extent the dynamic enhancing behavior of cellular materials, however, the calculated enhancement from Equation 1.5 and 1.6 is a small value which disagrees with the significant enhancement observed in experiments. Thus, the inertia effect is considered as the most promising mechanism to dynamic enhancement of cellular materials under moderate impact velocities. In order to investigate the effect of inertia in promoting the dynamic strength of honeycombs, three numerical models of micro-size thin-walled structure in different complexity are installed in this chapter.

2.1 Lateral inertia effect and the simplified model

2.1.1 Lateral inertia effect

The thin-walled structures may undergo unstable buckling deformation process during the out-of-plane crush, and the inertia effect under dynamic loading is not negligible.

The early theoretical work in this domain was reported by Budiansky and Hutchinson[16]. Gary[17] showed experimentally that the buckling of a column under compressive impact occurs at larger strain and higher force because of lateral inertia.

17

Calladine and English[18], Tam and Calladine[19] explained in detail the role of lateral inertia by identifying two genetic types (type I and type II) of plastically deforming structures in energy-absorbing situations. As shown in Figure 2.1, Type I structures have a flat topped quasi-static stress/strain curve. For this type of structure, the micro-inertia plays little role under dynamic loading and the quasi-static bending mode of collapse is maintained. Type II structures display a strongly softening bending mode of collapse which is in fact an unstable buckling under quasi-static conditions. When this Type II structure is under dynamic loading, the buckling process will be delayed due to the lateral inertia effect and result in an enhancement of strength and of plastic work to the thin-walled structure under dynamic loading. Tam and Calladine[19] further figured out that this elevation in strength is sensitive to the initial misalignment of the structures and a misalignment exceeding a few degrees eliminates the micro-inertia effect. Gao et al[20, 21] also performed detailed studies on the collapse behavior of type II structure.

Langseth et al[22], Langseth and Hopperstad[23] employed this concept to explain the strength increase observed in steel and aluminium square tubes. Su et al[24, 25] have given a classification of the rate sensitivity of different structures and used them for explaining the dynamic enhancement of cellular materials. Zhao and Gary[26] considered honeycombs under out-of-plane compression as Type II structure and the out-of-plane strength is significantly affected by loading rate. While, honeycombs under in-plane loading is taken as Type I structure, and the influence of loading rate is negligible. These assumptions basing on two types of structure have obtained good validation by their experiments. Deshpande and Fleck[14] classified the metallic foams of Alulight and Duocel into Type I structure and explained the insignificant enhancement of dynamic strength.

(a) Types of structures

(b) Quasi-static force-displacement curves
for each type of structure
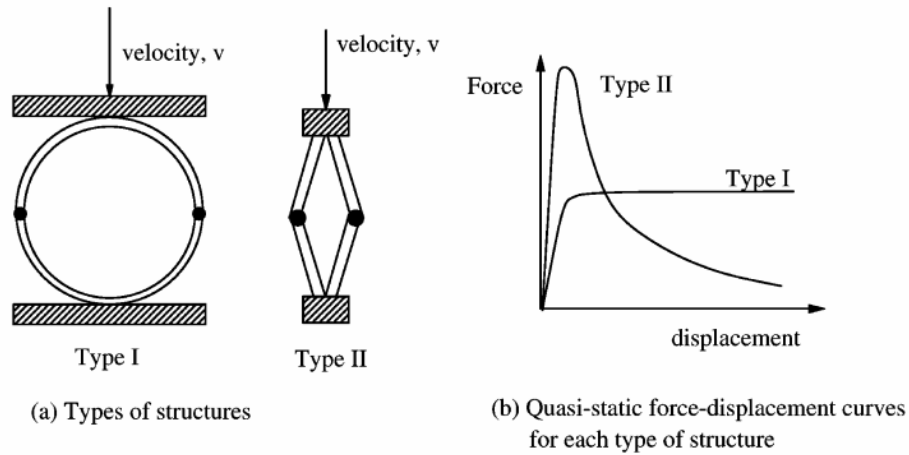
Figure 2.1 Scheme of Type I and Type II structures (a) and their force/displacement
curves under compression (b).

2.1.2 Simplified inertia effect model[27]

The lateral inertia effect proposed by Gary[17], and Calladine and English[18], can be outlined by a simplified model as proposed by Zhao[27] (shown in Figure 2.2). The model is made of two massless rigid plastic bars linked by a plastic hinge with a concentrated mass in the middle. These two bars are angled by a certain magnitude of 2θ to introduce initial imperfection to the model. The whole model is loaded by a compression on the top.
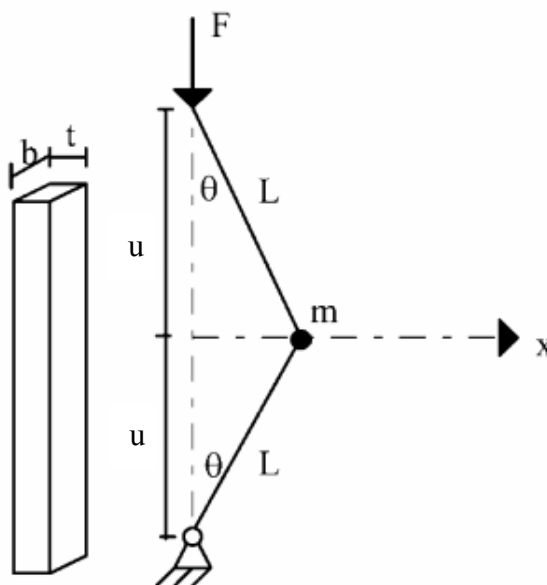
Figure 2.2 simplified inertia effect model[25]

This mechanical system follows geometrical relationship:

$$\delta \upsilon = -L \sin \theta \delta \theta \qquad 2.1$$

where L is the length of the bars, $\delta\upsilon$ is the axial displacement under compression, $\delta\theta$ is the change of angle between two bars.

Under static loading, the system will collapse once the maximum moment due to the applied force F overcomes the fully plastic moment of the plastic hinge

$$M_P = bt^2\sigma_s/4 \qquad\qquad 2.2$$

where b, t, are the geometric parameters of bar cross section (as shown in Figure 2.2), σ_s is the yield stress of hinge material. Thus, the critical force for model to collapse will be:

$$F = M_P\left|\frac{2\delta\theta}{2\delta\upsilon}\right| = \frac{\sigma_s bt^2}{4L\sin\theta} \qquad\qquad 2.3$$

It can be seen from Equation 2.3 that the critical force of this inertia effect model is related with the yield stress of base material, the geometric parameters of the cross section and the initial imperfection of the structure. If $\theta = 0^o$, the model will be always axially compressed without falling into plastic collapse.

When the model is loaded with sudden imposed higher speed, the same peak load as in the static case is reached instantly. However, the collapse of the system depends still on the motion of the concentrated mass in the middle, and the lateral velocity of the concentrated mass should be in compatibility with the vertical loading velocity, which has:

$$\frac{du}{dt} = \sin\theta\frac{dx}{dt} \qquad\qquad 2.4$$

where x is the lateral displacement of the concentrated mass.

The lateral acceleration of this concentrated mass is governed by the force transmitted to it by the bars.

$$m\ddot{x} = 2N\sin\theta \qquad\qquad 2.5$$

As the force transmitted by the bars is limited by their plastic flow stress, the acceleration of the mass has a maximum value given by:

$$m\ddot{x} \leq 2\sigma_s bt\sin\theta \qquad\qquad 2.6$$

Initially, the concentrated mass is at rest and its acceleration is limited to the value given by the Inequality 2.6. It takes time to reach the speed kinematically compatible with the vertical loading velocity. During this acceleration period, the global crushing displacement is mostly given by the compression of bars. The rotation is very small because the mass cannot move rapidly. The compressive strain reached

before collapse under impact loading is therefore higher than in the static case. If moreover, the bars are made of strain hardening material, the buckling force will be higher because the buckling strain in the bars is higher under impact loading. It should be noted that initial imperfections play a very important role here: the smaller the initial imperfection, the stronger is this inertia effect.

This simplified model provides an explanation to the dynamic enhancement of beam (or plate) structure basing on the lateral inertial effect, and its correctness has been validated in large-size structures both experimentally and analytically. Nevertheless, honeycombs are of micro-size thin-walled structure, in which, the similarity of model size and loading velocity to large-size thin-walled structure is out of knowledge and the inertia effect in elevating dynamic strength in such micro-structures need to be confirmed again.

2.2 Micro-size double-plate model for validation

We presented in 2.1 a simple analytical model from Zhao and Abdennadher[27] to illustrate the main concept of lateral inertia effect in explaining the dynamic enhancement of beam (or plate) structure. Here, this section is going to check the adaptability of this concept in micro-size thin-walled structures by building a double-plate FEM model with dimensions comparable to honeycomb. Besides, the capability of FEM in calculating the inertia effects during unstable buckling process of thin-walled structures is estimated and different numerical algorithms are also compared, which may provide a reference to the subsequent calculations on more complicated models.

2.2.1 Model installation

The simulation works are performed with commercial FEM code of ABAQUS. The scheme of this validating model is shown in Figure 2.3, which is composed of two angled plates solidly connected (common nodes). The size of the model is in the same order with honeycomb cell walls with the plate thickness $t=152\mu m$, plate width $b=1.833mm$ and height of one plate $L=1mm$, δ is the maximum deviation of plates from the vertical line, which represents the magnitude of initial imperfection of this model.

The geometry of the model should make sure that no elastic buckling occurs before the model collapse plastically. According to Euler's buckling criteria, the critical force for a beam falling into elastic buckling is as follow:

$$F_{cr} = \frac{\pi^2 EI}{(\mu L)^2} \qquad 2.7$$

and for beam with rectangular cross section: $I = \frac{bt^3}{12}$, the value of μ is related to the constraints of the beam and for the model here, $\mu = 1$. Submitting all the quantities into Equation 2.7, the critical load of such double-plate model is obtained to be:

$$F_{cr} = 9.26\text{N} \qquad 2.8$$
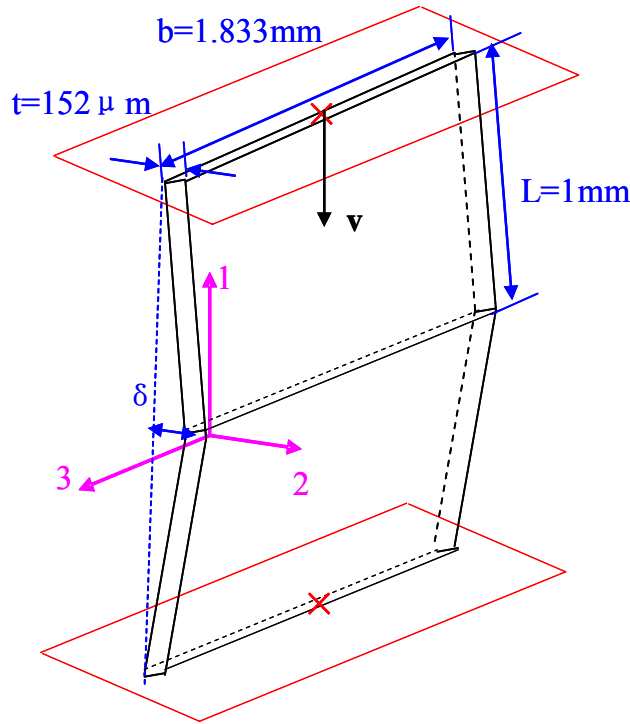
Figure 2.3 Scheme of double-plate model

Thus, in order to avoid the undesirable elastic buckle before the plastic collapse of the model, the plastic collapse load F_p should be lower than the elastic buckling load F_{cr} and then, the minimum magnitude of initial imperfection employed in this study is determined:

$$\delta_{\min} > 3.2\mu m \qquad 2.9$$

The double-plate model is sandwiched between two parallel rigid walls. One of them is fixed and the other one is moving at prescribed velocity which is applied on the reference point. For quasi-static problem, the loading velocity is 0.1mm/s and for dynamic loading 10m/s. A surface-to-surface rough contact is defined at the interfaces of double-plate model and rigid walls to make sure that no slippage occurs.

A 4-node doubly curved thick shell elements with a reduced integration, finite membrane strains, active stiffness hour-glass control (S4R) is employed to discretize the model and 15 integration points through the cell-wall thickness is set. In order to determine the appropriate element size, a convergence study was performed. It seems that the results converge when the element size is equal to or below 0.25mm. With the chosen element size of 0.25mm, our double-plate model has 132 elements.

The input material model is from the experimental stress/strain curve of 2024 aluminium alloy (as shown in Figure 2.4) with elastic modulus E＝70GPa, Poisson's ratio v＝0.35, and yield stress σ_s＝274MPa. The material behavior show obvious strain hardening property after the yielding point.
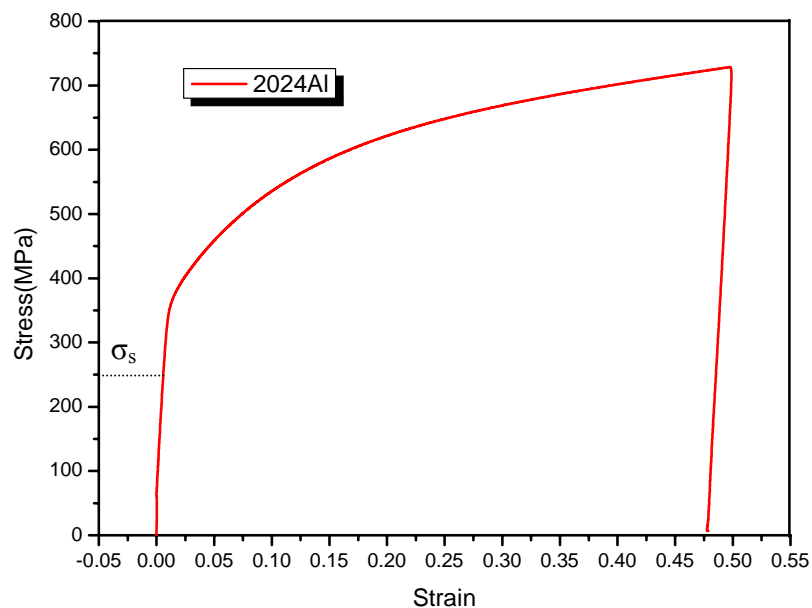
Figure 2.4 Stress/strain curve for 2024 aluminium alloy

2.2.2 Implicit and explicit

ABAQUS/Standard is usually employed for static problems. It uses implicit method such as Newton's method or quasi Newton's method as a numerical technique and has predominance in calculating accuracy. For dynamic problems, ABAQUS/Standard also

provides an implicit method with direct integration, i.e. the Hilber-Hughes-Taylor operator. This dynamic implicit analysis needs to solve the nonlinear equations simultaneously. Although a more accurate result can be expected, the cost of the calculation is very expensive, especially for the extreme problems with high nonlinearity. For example, the out-of-plane crush behavior of honeycombs is almost impossible to achieve by implicit method due to the complex nonlinear effects, e.g. the geometrical and material nonlinearity, the complex contact conditions as well as the local instability during crush.

ABAQUS/Explicit uses an explicit central-difference time integration rule and each increment is relatively inexpensive compared to the direct-integration dynamic analysis procedure available in ABAQUS/Standard, because there is no solution for a set of simultaneous equations. The explicit method is much higher computationally efficient for the analysis of large models with relatively short dynamic response time and for the analysis of extremely discontinuous or nonlinear processes. However, ABAQUS/Explicit is conditionally stable, and the stability limit is estimated by follow:

$$\Delta t \approx \frac{L_{\min}}{c_d} \qquad\qquad 2.10$$

where $L_{\min}$ is the smallest element dimension in the mesh and c_d is the wave speed. Δt is usually of a small value which makes ABAQUS/Explicit only suitable for transient high speed impact problems.

For the quasi-static simulations in this study, because of the difficulties of implicit method in calculating the large deformation process of honeycombs, an alternative method by using ABAQUS/Explicit is adopted. However, the explicit integration scheme of dynamic simulation codes usually leads to very small time increment which for example is around ten nanoseconds for the chosen element size of 0.25mm. Thus, with the loading velocity of 0.1mm/s, the computational duration for the quasi-static simulation will be too large. To overcome this difficulty, ABAQUS/Explicit provides an automatic mass scaling technique, which can be used to increase the time increment to an acceptable value by enlarging material density. The quasi-static loading conditions are guaranteed by ensuring the ratio of the kinetic energy to the strain energy as a small value with the chosen time increment. However, this technique may introduce errors to the calculating results, especially for the event in which inertia effect is important. Thus, some validating works should be performed

to estimate the potential errors. In this subsection, the implicit and explicit methods for quasi-static calculations are compared and the proper magnitude of time increment is estimated in order to give a good prediction of the quasi-static behavior with the employment of ABAQUS/Explicit+Mass scaling technique. This analysis can provide some references to the subsequent simulation on the more complicated models such as tube and honeycomb in Section 2.2 and 2.3.

Figure 2.5 displays the force/displacement curves from ABAQUS/Standard and ABAQUS/Explicit+Mass scaling technique respectively. These two methods have obvious deviation in calculating the elastic behavior of the double-plate model and the slope of the implicit curve is confirmed to be more accurate with the value close to the input material Young's Modulus of 70GPa. For the peak value, with the choice of time increment $\Delta t = 5 \times 10^{-5}$s (corresponding to a mass scaling factor of 100,000), a large difference is found between the curves from implicit and explicit method. When the time increment is reduced to be $\Delta t = 5 \times 10^{-6}$s, a good agreement of peak value is found for the implicit and explicit curves (as shown in Figure 2.5)
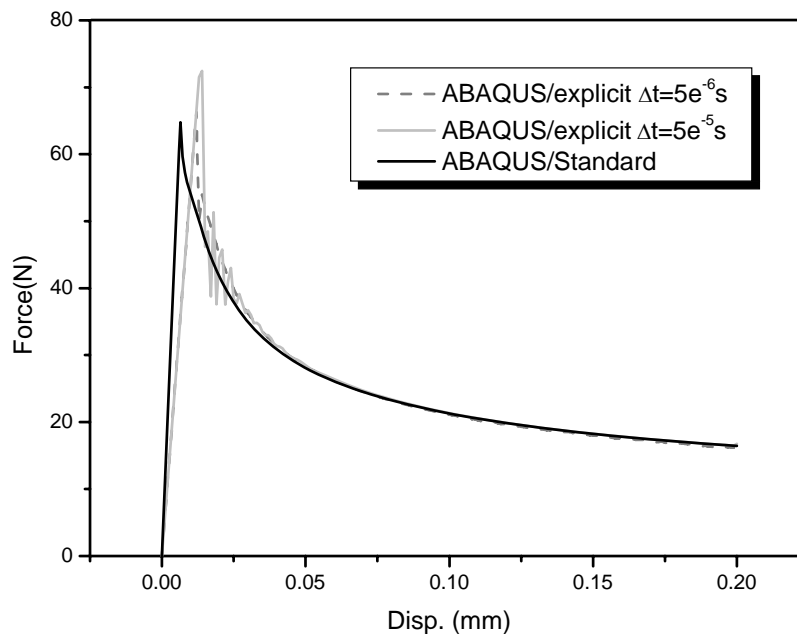
Figure 2.5 Comparison between the calculating results from ABAQUS/Explicit+Mass scaling with different time increment and the result from ABAOUS/Standard

The ratio of kinetic energy to strain energy as a function of time history is shown in Figure 2.6 for both the calculations with $\Delta t = 5 \times 10^{-5}$s and $\Delta t = 5 \times 10^{-6}$s. It is found that the ratio reaches the peak value at the moment of collapse. To ensure a quasi-

static loading condition and a rather accurate simulating result without obvious effect of inertia, the ratio between kinetic energy to strain energy should be at the order of 10^{-3}.

2.2.3 Lateral inertial effect

In order to investigate the dynamic enhancement of this double-plate model and reveal the inertia effect in the enhancement mechanism, we performed the simulations on this double-plate model with different loading rates, which are $V_{quasi\text{-}static} = 0.1$mm/s for quasi-static loading (solved by ABAQUS/Explicit + Mass scaling technique), $V_{impact}^{1} = 1$m/s, $V_{impact}^{2} = 5$m/s and $V_{impact}^{3} = 10$m/s for dynamic loading (solved by ABAQUS/Explicit). In order to facilitate the comparison with input stress/strain curve of base material, the calculated force/displacement curves are divided by plate length and cross sectional area to obtain the nominal stress/strain curves of the model. All the calculated curves are displayed in Figure 2.7.
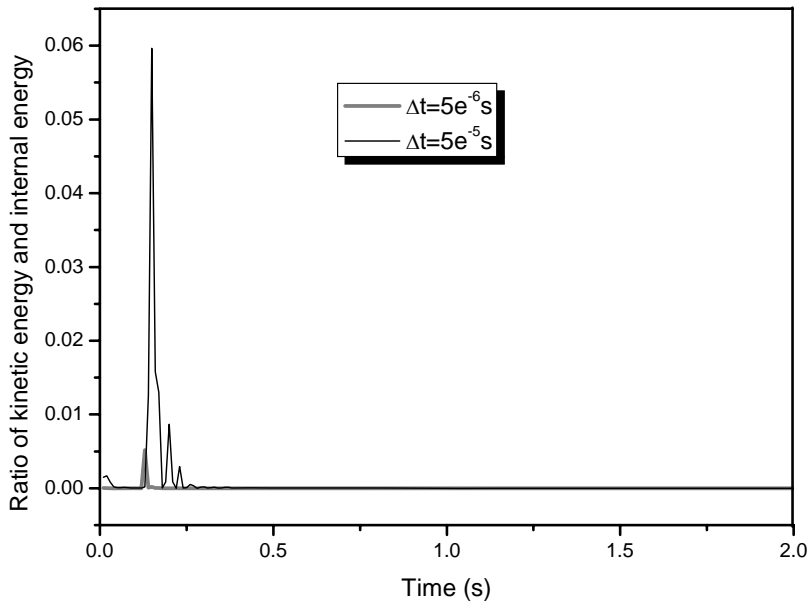
Figure 2.6 Ratio of kinetic energy and internal energy when using mass scaling technique
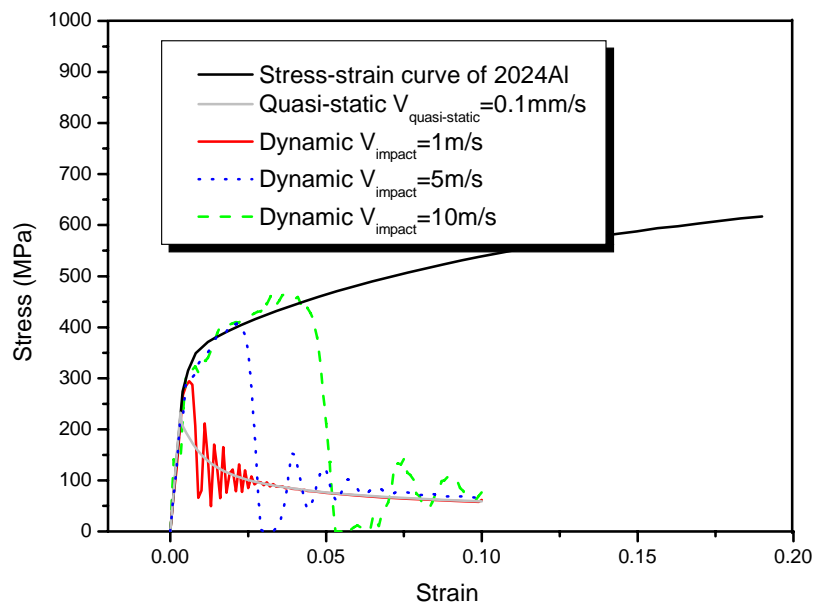
Figure 2.7 Comparison between nominal stress/strain curves of double-plate model under different loading velocities and stress/strain curve of 2024 aluminium alloy

It can be found that the peak point (collapse point at which the curve begin to decrease rapidly) of the quasi-static curve is coincident with the yield point of the material stress/strain curve, which means that the model begins to collapse when the average stress in the model reaches yield stress (this is true when the initial imperfection of the model is appropriate). While, the collapse points for all the dynamic curves are elevated along the material stress/strain curve with the increasing loading velocity. It seems that the collapse of this double-plate model is delayed and occurs at a larger plastic strain as well as higher stress. An obvious dynamic enhancement phenomenon is observed.

We further check the stress distribution along thickness direction of one element on the intersection line of two plates at the moment of collapse and the Mises stress of 15 integration points is shown in Figure 2.8. It is found that the stress distribution along thickness direction is rather uniform under quasi-static loading. While for the higher loading rates, the distribution deviates from uniformity gradually. This means that the double-plate model is deformed more in axial direction before entering into collapse at dynamic loading, and then the deviation of plates from the vertical line at collapse moment is much larger, which results in the non-uniform stress distribution along thickness under higher loading rates.
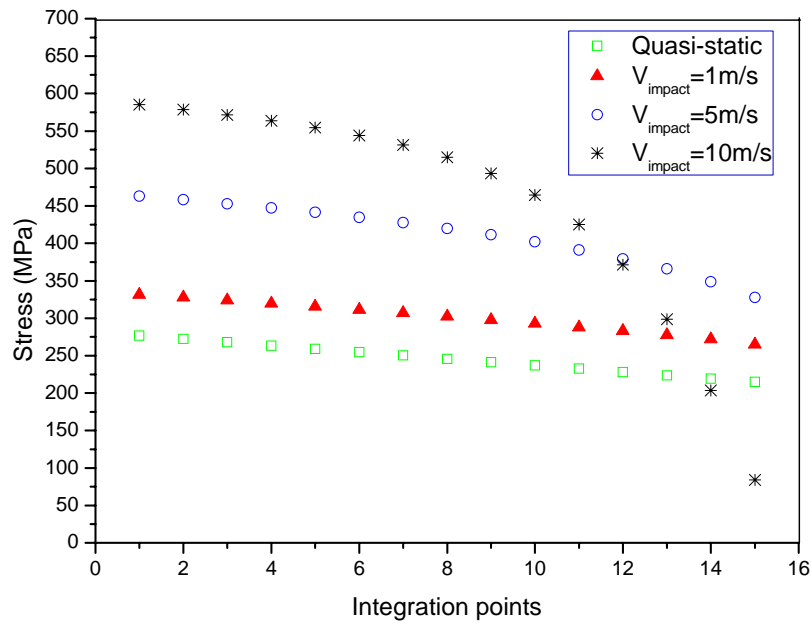
Figure 2.8 Stress distribution of double-plate model along foil thickness at different loading cases

It is indicated that the collapse behavior of double-plate model under dynamic loading is characterized by a collapse delay effect. The model undergoes larger plastic strain in axial direction before the collapse occurs and the relationship between the peak stress and collapse strain is coincident with the material stress/strain curve. It has been illustrated in Section 2.1 that this collapse delay effect has relations with lateral inertia, which prolongs the duration for lateral velocity to reach a certain value to match the axial loading velocity. In order to verify this assumption, the lateral velocity profiles of an element on the intersection line from all the loading cases are compared in Figure 2.9. The lateral velocity at collapse moment increases with increasing loading velocity and the positions of collapse move backwards in succession when the load velocity increases. These observations are in good agreement with the assumptions in 2.1.2 on the lateral inertia effect model and the validity of the proposed dynamic enhancement mechanism in a micro-size model is confirmed.
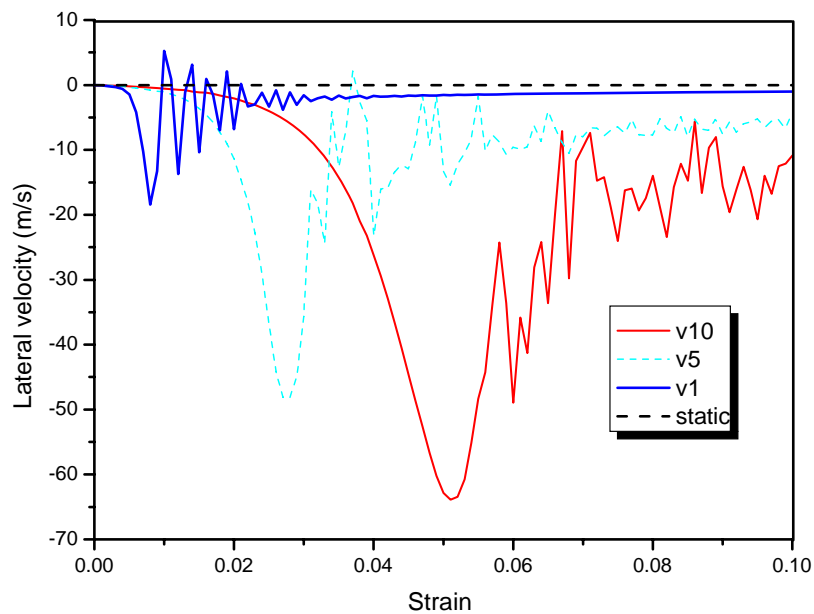
Figure 2.9 Lateral velocities of the mid-point on plastic hinge under different loading velocities

2.3 Lateral inertia effect in the crushing process of tube

It is demonstrated in Section 2.2 the lateral inertia effect in the dynamic enhancement of the simple micro-size double-plate model. However, the real cellular materials (such as honeycombs) are always with complex structure and will undergo a much more complicated crush process, which is far away from the collapse of double-plate model.

Zhao and Abdennadher[27] chose a square tube structure which is between the simple double-plate model and the complex honeycomb structure to investigate its dynamic enhancement. This section will present briefly the work of Zhao and Abdennadher[27] firstly, and then further simulation works on this subject is performed with a micro-size tube model.

2.3.1 Works of Zhao and Abdennadher[27]

2.3.1.1 Experimental and numerical results

Zhao and Abdennadher performed the compressive crushing tests on a square tube made of brass both quasi-statically and dynamically in order to investigate the

impact strength enhancement of this structure. A large specimen with dimensions of 35mm×35mm on the cross section is employed, and the thickness of the tube wall is 1.5mm. Figure 2.10 shows the dynamic and quasi-static force/displacement curves of square tube under compressive crush. It can be seen that both the initial peak and the subsequent crush behavior show obvious dynamic enhancement effects (the enhancing rate is about 34%).
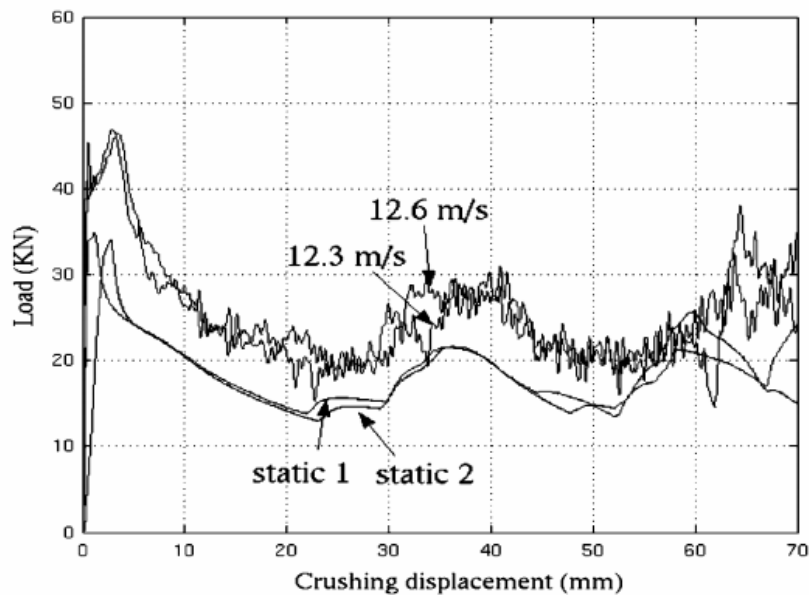
Figure 2.10 Dynamic and quasi-static force/displacement curves of squar tube from Zhao and Abdennadher by experiments[27]

Basing on the experimental results, Zhao and Abdennadher performed also the numerical studies on this problem by LS-Dyna. The calculating results displayed in Figure 2.11 show also an obvious enhancing effect under dynamic loading. The dynamic enhancement rate for the initial peak is in good agreement with the experimental one, while for the successive peak load in subsequent crushing stage, the calculated enhancing rate is smaller than the one from experiments.
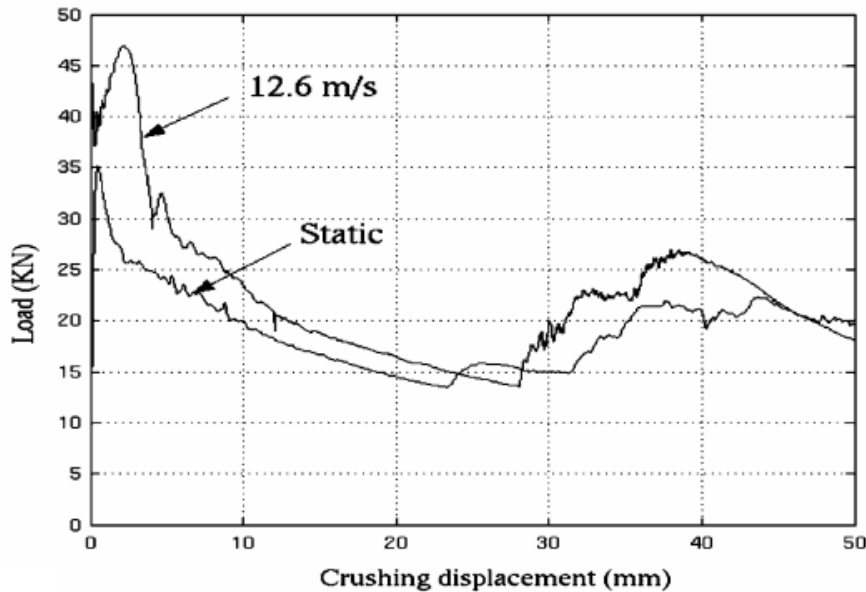
Figure 2.11 Dynamic and quasi-static force/displacement curves of squar tube from Zhao and Abddennadher by calculations[27]

2.3.1.2 Folding events in successive crushing

Zhao and Abddenadher found that the folding cycles are composed of two stages. At the start, crush is obtained by bending in the middle of the flat plates (the two trapezoids around nodes B or B' in Figure 2.12) and there exist small areas around the four corner lines (the two adjacent triangles around node A in Figure 2.12) which remain vertical and can support more external load. The second stage begins with the buckling of the corner line areas as shown on the right of Figure 2.12. The buckling of these edge zones corresponds to a decrease of the global crushing load.
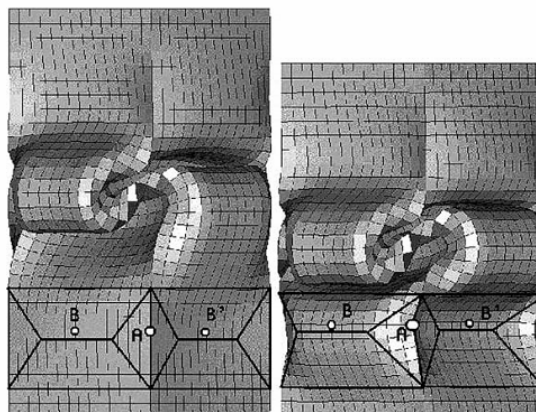
Figure 2.12 Deformation of squar tube from Zhao and Abdennadher by calculations[27]

Zhao and Abddenadher also checked the stress profile in the crushing direction, e.g., in the cross-section from node B to node A (see Figure 2.12). In Figure 2.13 (a),

31

an enhancement of 14% is observed for the corner elements corresponding roughly to the rigid wall force enhancement between the static and dynamic simulations shown in Figure 2.11. Figure 2.13(b) shows that the equivalent strain profile in the dynamic case is higher than in the corresponding static case, and this is especially true for the corner elements. The enhancement of stress and strain of corner element at dynamic loading rate can be used to explain the dynamic enhancement of tube crushing behavior.

(a）

(b）
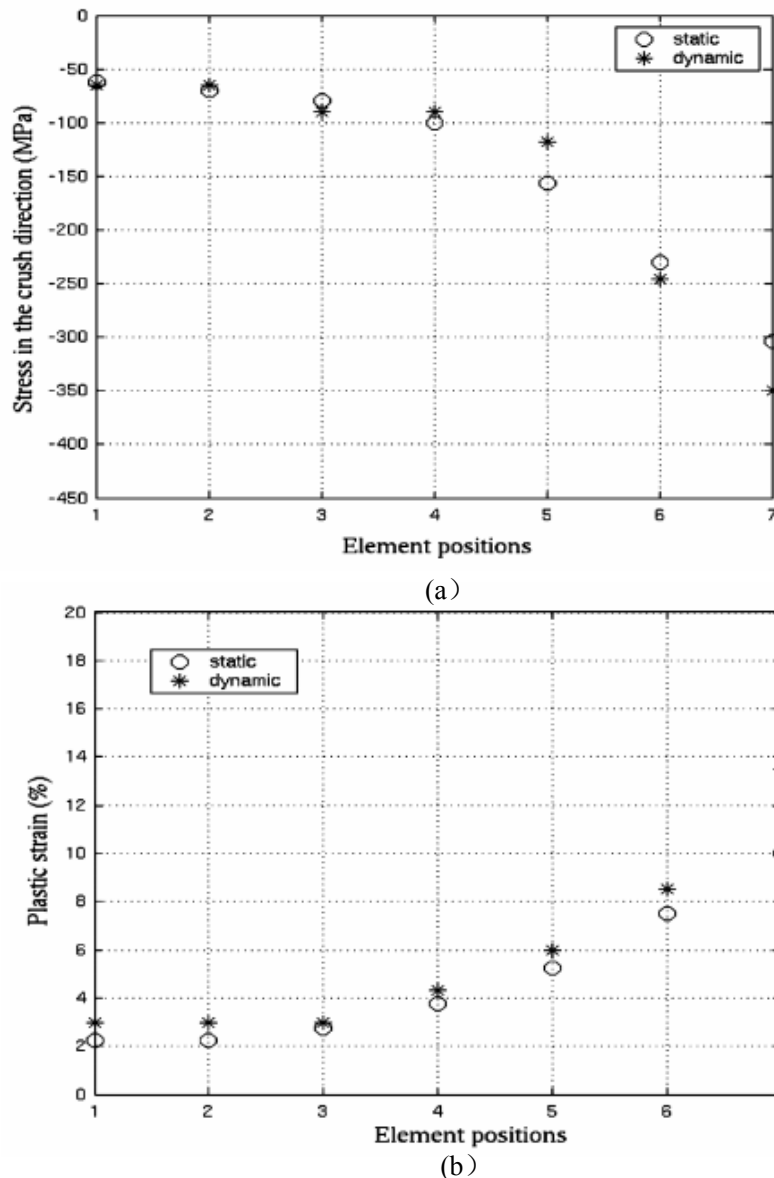
Figure 2.13 Stress (a) and strain (b) profile (from moddle to conner)[27]

2.3.1.3 Mechanism of dynamic enhancement

Zhao and Abdennadher explained the dynamic enhancement of initial peak by adopting directly the dynamic enhancement mechanism for double-plate model. It is

found in Figure 2.14 that the nominal stress of tube follows the stress-strain curve of the base material as predicted by the simplified inertia effect model.
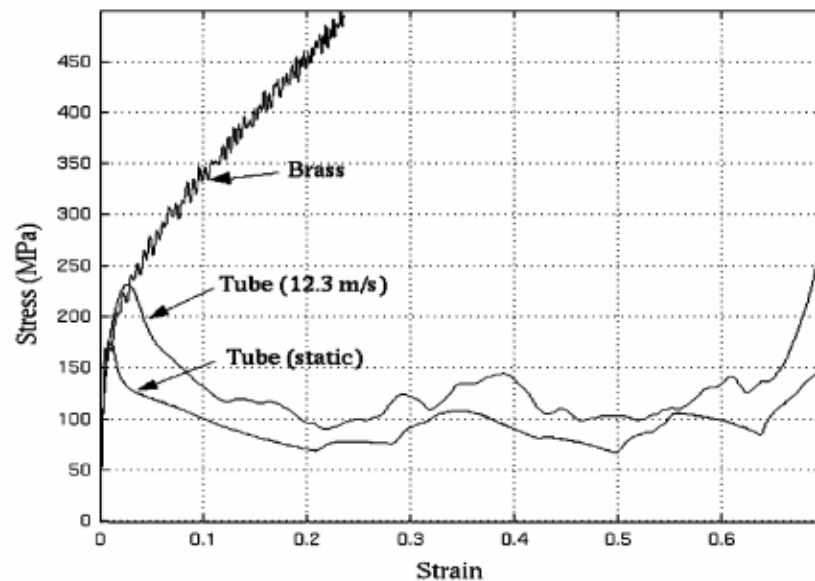
Figure 2.14 Comparison between nominal stress/strain curves of square tube and stress/strain curve of brass[27]

Nevertheless, the dynamic enhancement mechanism in successive crushing period is more complicated. Zhao and Abdennadher found that the stress and strain distributing in the corner region is obviously higher under dynamic loading than under quasi-static loading, which agrees well with the concept of inertial effect model.

In summary, Zhao and Abddennadher proposed in their work a simple model basing on inertia effect to explain the strength enhancement of square tube under dynamic loading. In order to adapt this mechanism into cellular materials, such as honeycomb, some further investigations on their work maybe helpful. First, a macro-size tube structure is employed in the study of Zhao and Abddennadher, which has obvious difference with the dimensions of thin-walled structure as in honeycomb. A dynamic enhancement mechanism which is dominated by inertia effect is supposed to have relations with model dimensions and a micro-size tube model should be involved. Second, the stress and strain elevation in square tube under dynamic compression has been validated, however, as to the reason, no direct evidence is provided in their work to show the collapse delay due to the inertia effect. Finally, the strain hardening behavior of base material is an important factor in the concept of inertia effect model, and its influence on the dynamic enhancement of cellular materials should be investigated.

Thus, the promising work of Zhao and Abddennadher on the crush behavior of square tube is continued in this study. On the installation of FE model, a micro-size tube model is firstly established in order to be comparable with the cellular materials. Secondly, the method for introducing initial imperfection is improved. At last, ABAQUS/Explicit + Mass scaling technique is employed for the quasi-static analysis. On the analysis of calculation results, the unstable deformation of corner region at the moment of collapse is checked and the delay of buckling due to inertia effect and lateral velocity compatibility are confirmed. Finally, three base materials with different strain hardening behavior are used to calculate the dynamic enhancement in the same problem and the assumption of this inertia effect mechanism is completely validated. This inertia effect model seems to be a promising mechanism for explaining the dynamic enhancement of cellular materials especially the ones with thin-walled structure.

2.3.2 Micro-size tube model

According to the symmetry of square tube, a quarter geometric model is employed with length of the model L=10mm, wall thickness t=152μm and the half width of a＝1.83mm, which are comparable to the geometry of honeycomb structure, the FE model is shown in Figure 2.15.
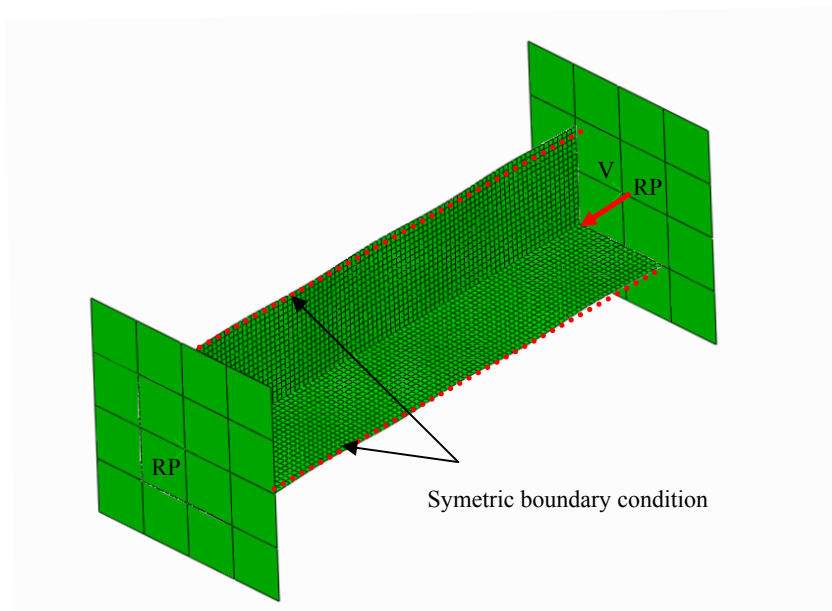
Figure 2.15 FEM model of square tube

The model is also discretized by 4-node doubly curved thick shell elements with a reduced integration, finite membrane strains, and active stiffness hour-glass control (S4R). 5 integration points is set through the cell-wall thickness. An element size of 0.1mm is employed in order to get refined stress or strain distributions. The micro-size tube model has totally 3634 elements.

The tube model is placed between two parallel rigid loading walls. A group of loading velocities are employed in the calculations, which are V_1＝1mm/s for quasi-static loading, V_2＝30m/s and V_3=60m/s for dynamic loadings. Symmetric boundary conditions are applied respectively on the two free edges of tube. General contact with frictionless tangential behavior is defined for the whole model excluding the contact pairs of rigid planes and tested honeycomb specimen, which are redefined by surface-to-surface rough contact to make sure that no slippage occurs.

Initial imperfections are necessary for calculating the crush behavior of square tubes under axial compression, especially for the quasi-static simulations. On the one hand their magnitude determines the initial peak of the force/crush curve; on the other hand, the type and distribution of initial imperfections have influence on the initial buckling as well as the successive folding system. Same initial imperfections with appropriate magnitude are introduced into the dynamic and quasi-static simulations to ensure the same folding system and facilitate the comparison. Here in this study, we introduce the imperfections from the elastic buckling modes of the tube structure. Some buckling modes of the square tube model with different order are shown in Figure 2.16. A perfect tube model without any imperfection is firstly crushed under dynamic loading to determine approximately the folding wave length (and then the order of introduced buckling mode). For the tube model here, the displacement field of Mode 10 with magnitude of 76μm, which is half of the wall thickness, is introduced into the perfect tube model in ABAQUS before applying the axial compression.

Mode 1   Mode 3

Mode 7   Mode 10
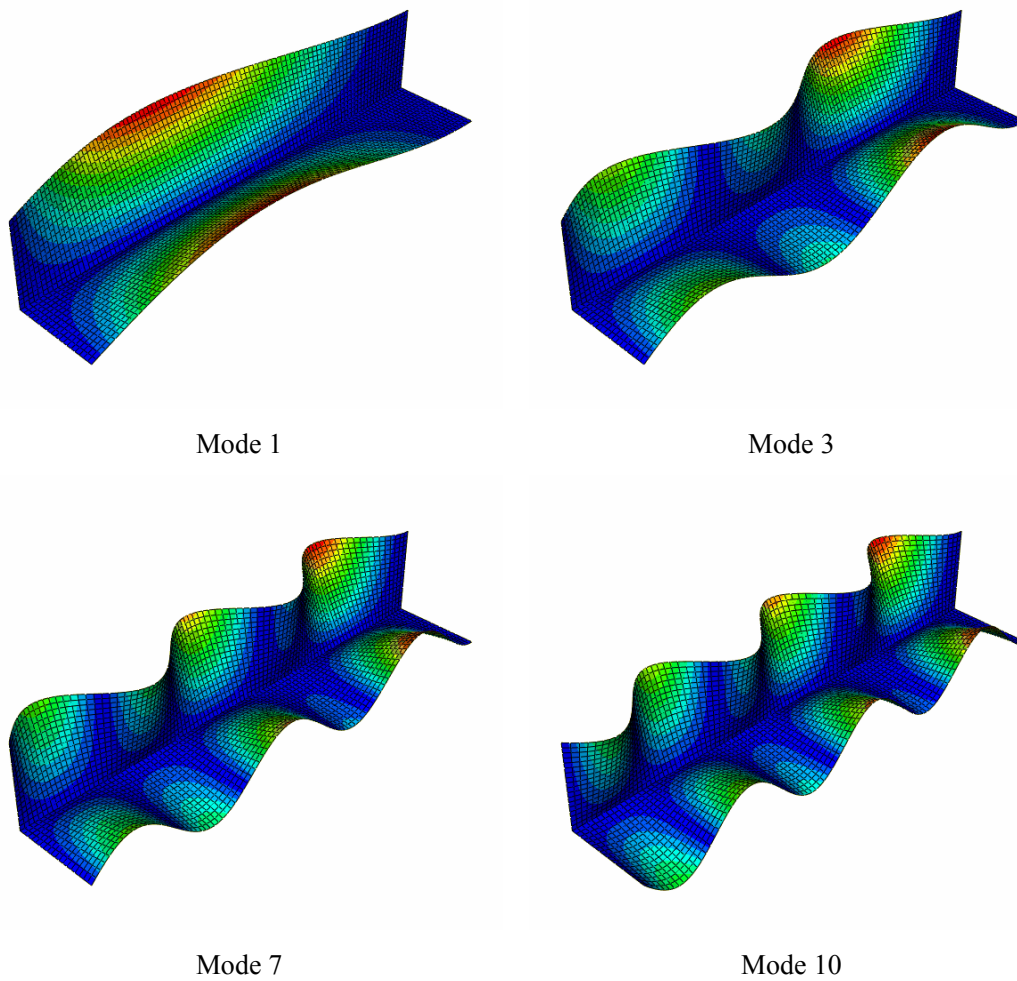
Figure 2.16 Buckling modes of square tube under uniaxial compression

The crush behavior of square tube under quasi-static loading is calculated by ABAQUS/Explicit + Mass scaling technique, and the time increment of $\Delta t = 5 \times 10^{-6}$s is employed. With this time increment, the ratio between kinetic energy to strain energy is of the order of 10^{-3}.

In order to check the influence of base material on the dynamic enhancement of square tube crush process, three base materials with different strain hardening behaviors are employed. The elastic parameters and the yield stress of these three models are the same (as shown in Table 2.1). The flow stress after yielding is given in exponential form, of which, Material 1 is fitted from the real stress-strain curve of 2024 aluminium alloy and with strain hardening exponent $m_1 = 0.21$, Material 2 and Material 3 are with $m_2 = 0.1$ and $m_3 = 0.3$ respectively. All the curves are displayed in Figure 2.17.

Table 2.1 Material parameters used in the FEM model of square tube

Material	Density $\rho(kg/m^3)$	Young's Modulus E (GPa)	Poission's Ratio v	Yield Stress σ_s (MPa)
Aluminium	2700	70	0.35	274
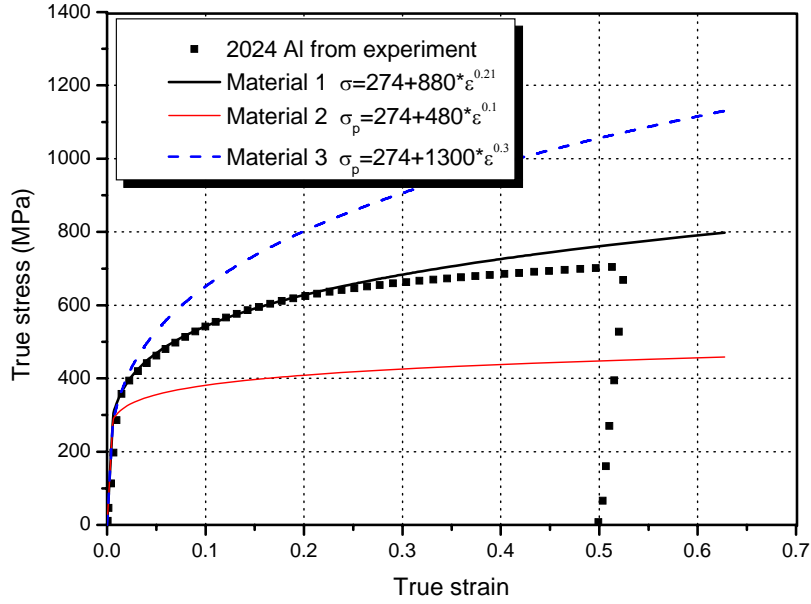
Figure 2.17 Input stress/strain curves of the square tube FEM model

2.3.3 Details on square tube crushing process

In this subsection, we are going to investigate the deformation details of the square tube in order to check the adaptability of inertia effect model to the dynamic enhancement. The complete deformation process is examined carefully and the relation between tube deforming configurations and the overall carrying capacity is determined.

Figure 2.18 presents the force/crush of square tube made of Material 1 under impact velocity of $V_2=30m/s$. The whole deforming process is from zero crush to compressive displacement of $\delta=6mm$. In Figure 2.18, segment a represents the elastic deformation period, b, d and c, e are respectively the two ascending and descending segments of in successive crush. Points A, C, B and D denote respectively the two peaks and two troughs of the curve.

The sequence of deformation configurations is shown in Figure 2.19. When the deformation starts, the tube model undergoes elastic deformation firstly (segment *a* in Figure 2.18) and obvious stress wave propagation process can be observed (as shown in Figure 2.19 (a)).

When the loading process goes further, most of the load is supported by the corner region. Figure 2.19 (b) shows the stress distribution at the moment of initial peak (corresponding to point *A* in Figure 2.18) and a stress concentration on the corner region is found. A stress distribution with alternant loading-unloading pattern is found on the tube walls, which indicate the plastic buckling of these plates region. At this moment, the corner region has only axial compressive strain although the stress has exceeded the yield stress of base material (274MPa). It should be noted that there is also possibility for the tube walls to come into elastic buckling to reach the initial peak which is decided by the magnitude of initial imperfections.

Further compression of the corner region in axial direction will finally result in bending deformation of this region, and the first fold begins to form. During this process, the axial compressive displacement is adapted by the bending deformation of the first fold material, while the other part of the tube is kept untouched. The overall carrying capacity decreases dramatically (segment *b* in Figure 2.18). The deformed configuration in this period is shown in Figure 2.19 (c).

When the bending of the first fold reaches a certain state, the first fold is completely formed and the carrying capacity of the whole model is locally minimum (point *B* in Figure 2.18 and Figure 2.19(b)). Further deformation of this part necessitates larger external force than compressing the untouched part of the tube. The neighboring material of the first fold begins to afford loading to form the second fold and the carrying capacity of this tube model begins to increase (segment *c* in Figure 2.18 and Figure 2.19(e)).

The bending of corner region of the second fold under continued axial compression corresponds to the local maximum loading capacity of the tube in successive crushing period (point *C* in Figure 2.18). The deformation configuration is displayed in Figure 2.19 (f), which is of great importance for investigating the dynamic enhancement of square tube in successive crush.

Hereafter, the formation of the second fold will repeat the first one. The bending deformation of this part increases and the carrying capacity of structure decreases continuously(segment *d* in Figure 2.18 and Figure 2.19(g)), until the third fold begin

to afford loading and the carrying capacity of the tube model increases again (segment *e* in Figure 2.18 and Figure 2.19(i)) from the trough *D* in Figure 2.18.
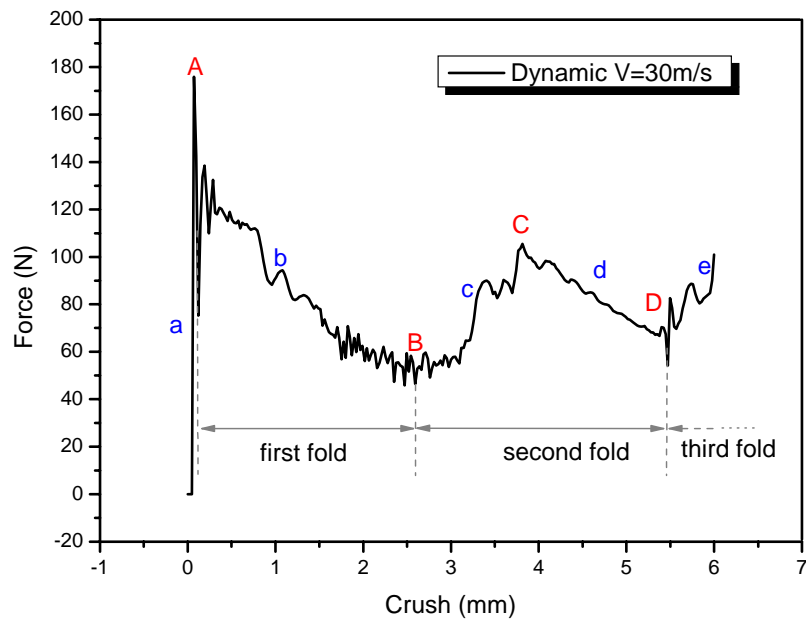
Figure 2.18 Force/crush curve of square tube under crush

a	A
(a) δ＝0.03mm	(b) δ＝0.12mm

(c) δ＝1.5mm

(d) δ＝2.55mm

(e) δ＝3.6mm

(f) δ＝3.75mm

d

D

(g) δ＝4.5mm

(h) δ＝5.46mm

e

(i) δ＝6mm
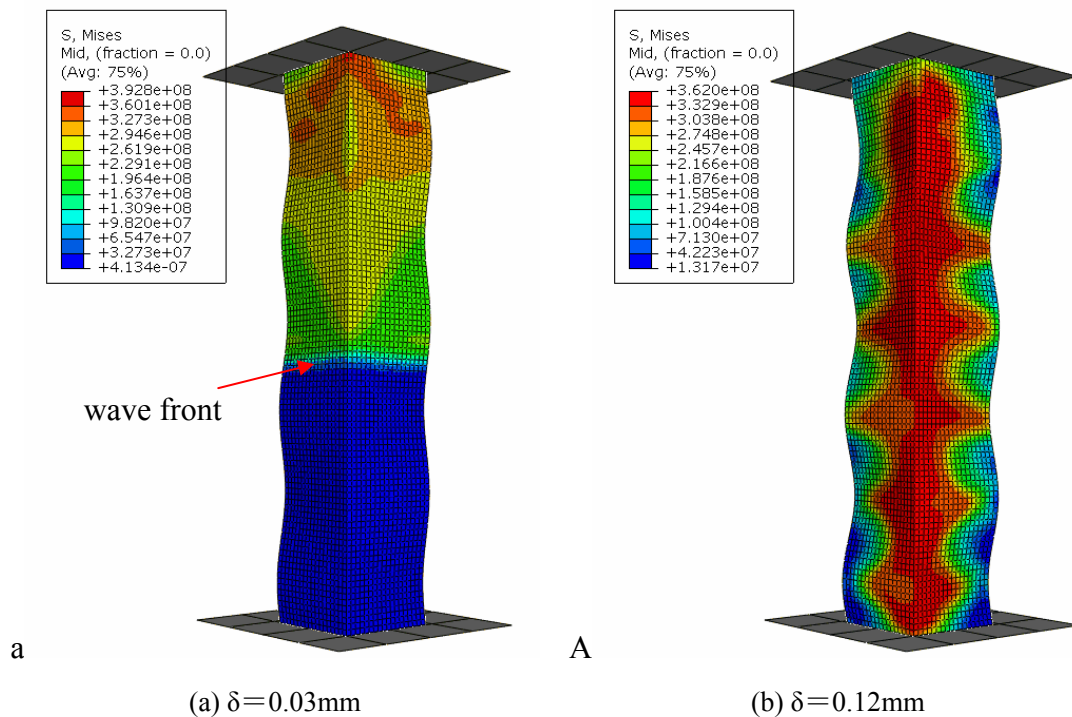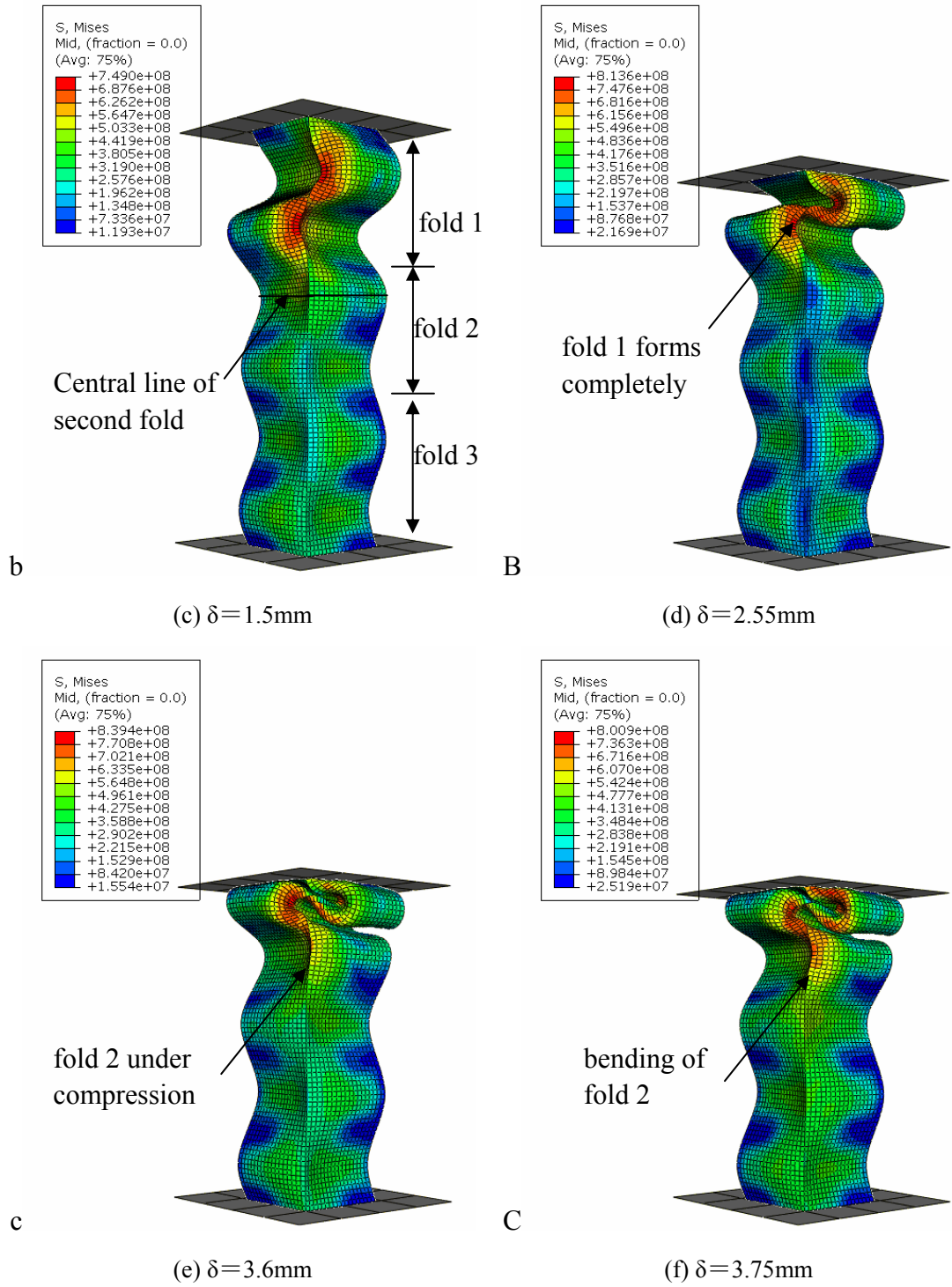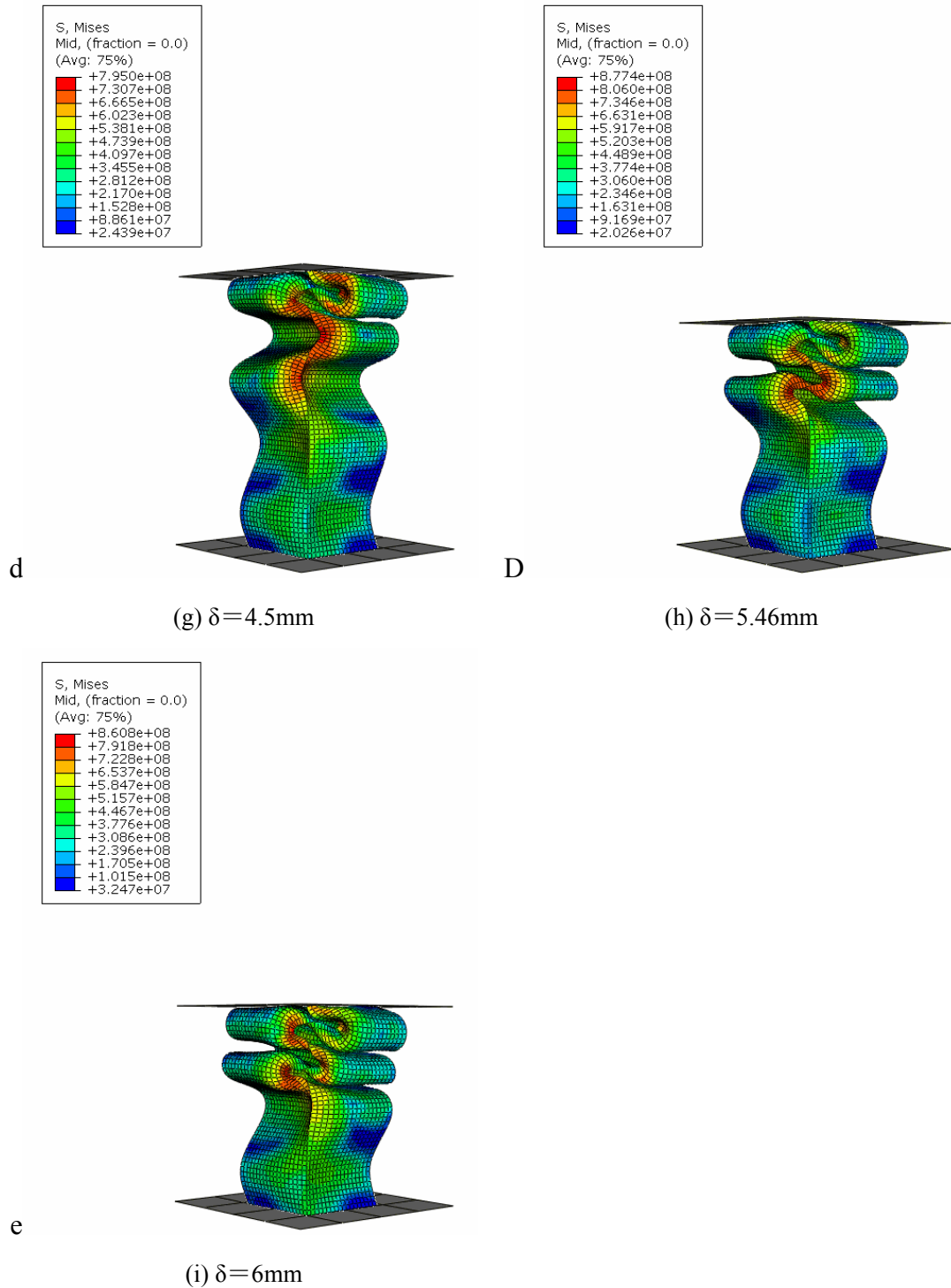
Figure 2.19 Deformation process of square tube under crush

The deformation process under quasi-static loading is similar to dynamic loading and will not be repeated here. Only the dynamic and quasi-static force/crush curves are compared in Figure 2.20. It can be found that both the initial peak and the successive peak under dynamic loading show an obvious enhancement from the quasi-static one. As the loading velocity increases, this dynamic enhancement becomes more significant.

2.3.4 Dynamic enhancement of the first peak

As illustrated in 2.2.3, the initial peak of force/crush curve of the square tube has relations with the collapse of the tube walls. This process is comparable to the collapse process of double-plate model and the validity of the inertial effect model in tube structure has been confirmed by Zhao and Abdennadher[27]. Here, we present in Figure 2.21 the stress distributions on tube walls at the moment of initial collapse for three loading cases. It is observed that the central area of one fold is under loading and the top and bottom of this part is unloading. Moreover, the stress level at the central area is found to increase with loading velocity, and the maximum
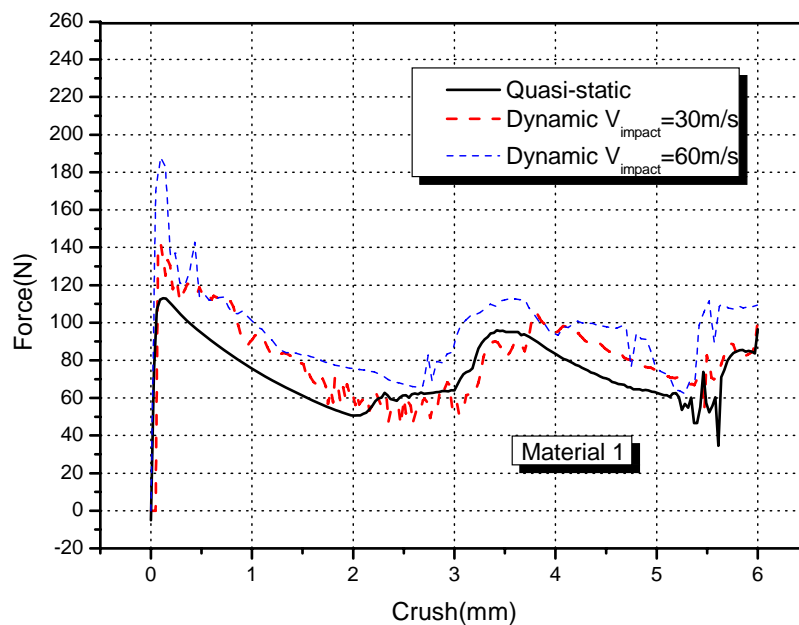
Figure 2.20 Force/crush curve of square tube under different loading rates

value of which are respectively 305MPa for quasi-static loading, 359MPa for dynamic loading with $V_2=30$m/s and 403MPa for $V_3=60$m/s.

The stress distributing along the central line is also checked for the three loading cases. As shown in Figure 2.22, the increase of loading velocity elevates not only the maximum stress but also the whole stress distribution on the tube walls, which results in finally the initial peak enhancement of the tube.

42
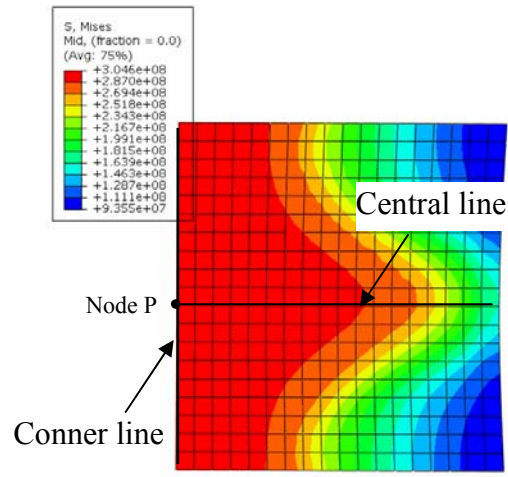
(a) Quasi-static
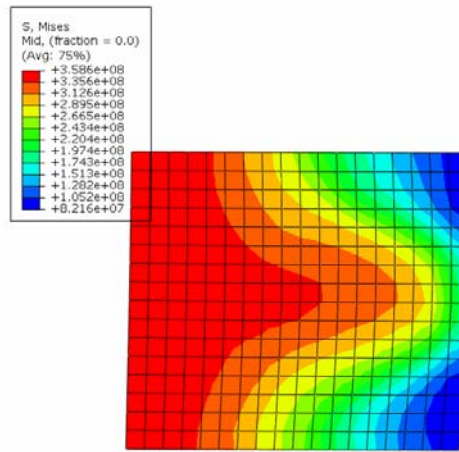
(b) $V_2 = 30\text{m/s}$
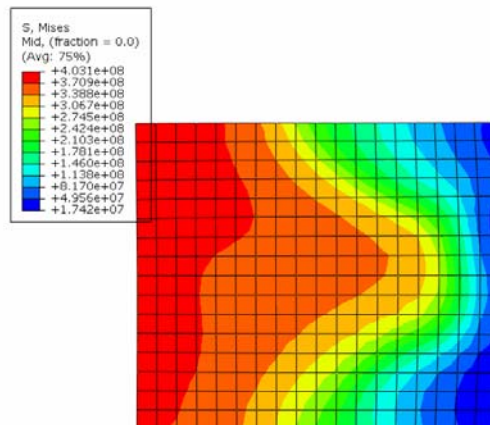
(c) $V_3 = 60\text{m/s}$

Figure 2.21 Mises stress distribution of square tube on walls under different loading rate
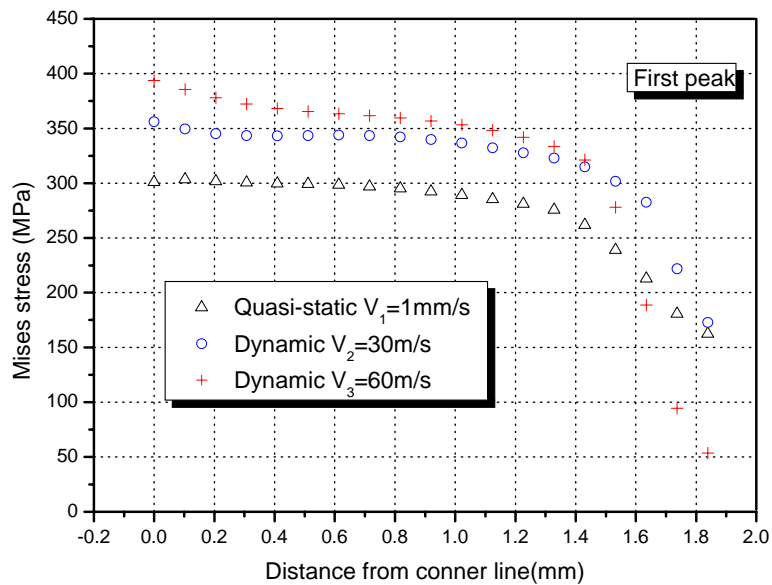
Figure 2.22 Mises stress distribution along the central line on tube walls at the moment of initial buckling

As to the reason of this elevation of stress (or strain) at the moment of initial peak, a collapse delay effect due to lateral inertia is involved. It is believed in this inertial effect model that the collapse depends on not only the stress level at the central line region, but also the lateral velocity at this part, which should be in compatible with the axial compression velocity. In order to check this, we present in Figure 2.23 the lateral velocity along central line at the moment of initial collapse. It is found that the lateral velocity of the corner region is much lower than the other positions, which means that the initial collapse of the tube model is actually related to the buckling behavior of the tube walls. The compatible lateral velocity at the plate region is found to increase with the increasing loading velocity and a longer duration is expectable for this velocity to reach the desired value under the effect of inertia. During this process, the axial compression on the tube walls continues and larger strain (and stress for strain hardening base material) is obtained.
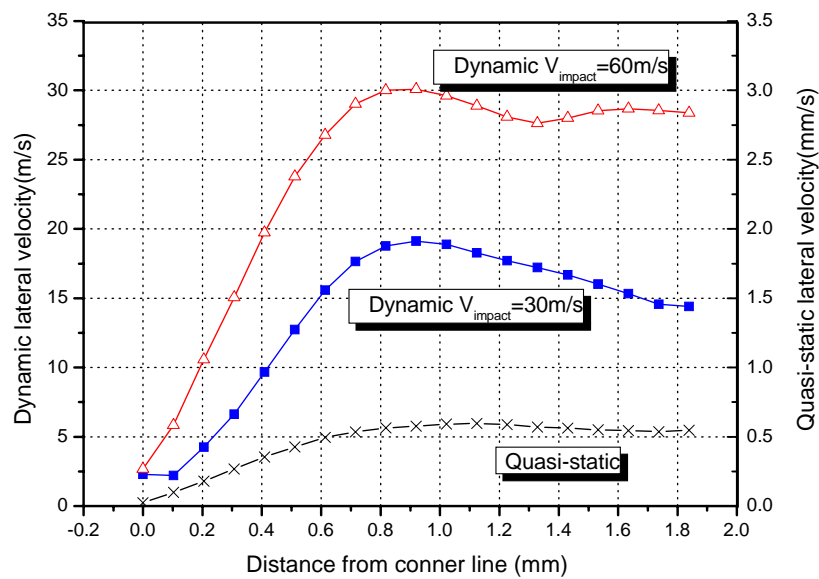
Figure 2.23 Lateral velocity distribution along the central line on tube walls at the moment of initial buckling

2.3.5 Dynamic enhancement of the successive peak

The second peak in successive crush is related to the bending of the corner line of the second fold. Stress and strain distributions along the central line of the second fold are displayed in Figure 2.24 and Figure 2.25 respectively. Similar observations with Zhao and Abdennadher[27] are found. The corner stress and strain are much higher than at the other positions and an obvious increase of these quantities at dynamic loading is found.

The enhancement of stress and strain distributions in the successive fold can be attributed to the inertia effect on the collapse of corner line. The bending behavior of corner line is also an unstable buckling process, which can be certificated by the time history of lateral velocity(as shown in Figure 2.26) of the middle node(denoted as Node *P* as shown is Figure 2.21(a)). In Figure 2.26, the lateral velocity shows a sharp change at the moment when the corner line collapses, indicating an unstable deformation process, in which, inertia effect may plays an important role. Beside, the lateral velocity increases significantly with the increasing loading velocity, which means that the collapse delay effect due to lateral inertia is more significant under larger loading velocity and a higher carrying capacity of the whole model is expectable.

45
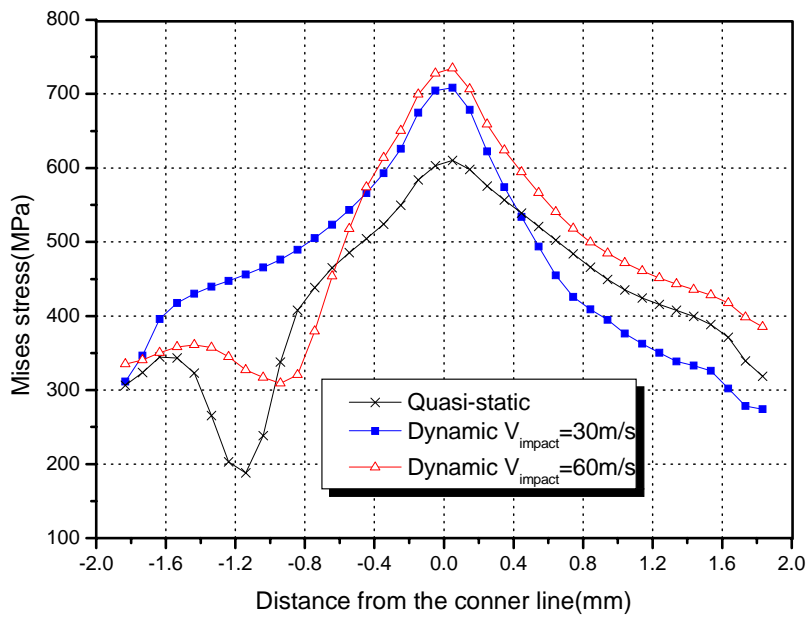
Figure 2.24 Mises stress distribution along the central line on tube walls then the conner of second fold begins to buckle
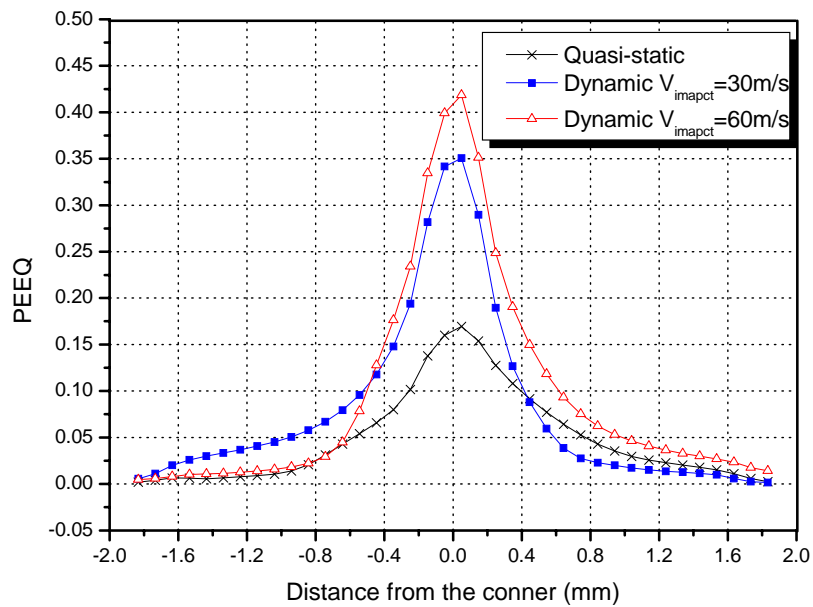
Figure 2.25 Equivalent strain distribution along the central line on tube walls then the conner of second fold begins to buckle
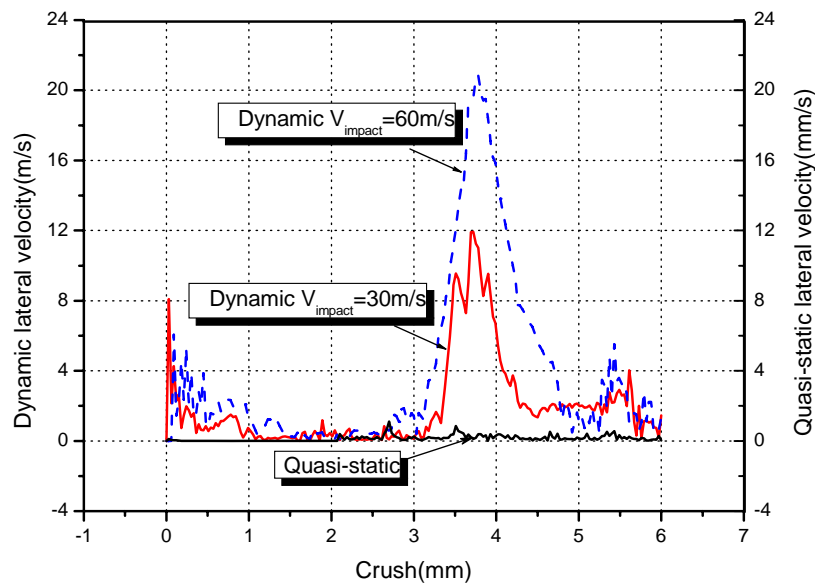
Figure 2.26 Lateral velocity of the mid-point on the conner line of second fold

2.3.6 Influence of base material on the dynamic enhancement of square tube

From the explanation presented above on the dynamic enhancement of thin-walled structures, the strain hardening behavior of base material may play an important role. When the collapse of corner line is delayed by the lateral inertia effect, the structure will be compressed in axial direction further, and the elevation of stress as well as the carrying capacity of the structure is achieved with the combination of a strain hardening base material. It is believed that the change of strain hardening behavior of the base material will also affect the dynamic enhancement properties of the thin-walled structures.

In order to make clear of this assumption, we performed the simulations on our micro-size tube model with three base materials which are with different strain hardening behaviors. The elastic parameters and the stress-strain curves of these materials are shown in Table 2.1 and Figure 2.17 respectively.

Figure 2.27-2.29 shows respectively the dynamic and quasi-static force/crush curves for three base materials. No significant difference is found for the initial peak of three quasi-static curves, which means that the initial collapse of square tube under quasi-static loading occurs at the yielding point of base material and is rarely influenced by the plastic behavior. When the loading velocity increases, the collapse

of tube walls is moved backwards along the stress-strain curve of base material and a dynamic strength enhancement is found. Higher strain hardening exponent results in a higher dynamic enhancement rate, which are 23.9% for material 1(m_1＝0.21), 16.7％ for Material 2 (m_2=0.1) and 37.8％ for Material 3 (m_3=0.3).

The dynamic enhancement rate of successive peak is also influenced by the strain hardening behavior of base materials. For material 1, the calculated dynamic enhancement rate is 8.25%, and this value increases to be 18.4% when Material 3 with higher strain hardening exponent is employed. By contrary, for material 2 with lower strain hardening exponent, this value is only 5.8％.

The calculation results displaying in Figure 2.27-2.29 have confirmed the roles played by strain hardening behavior of base materials in the dynamic enhancement of square tube structure. It worth emphasizing that the delay effect of both the initial and successive collapses of tube model due to lateral inertia are not independent from the influence of strain hardening behavior. When the material becomes "harder" with a higher strain hardening exponent, the acceleration in lateral direction is also enlarged. The desired lateral velocity is reached more quickly and the collapse point may be advanced.
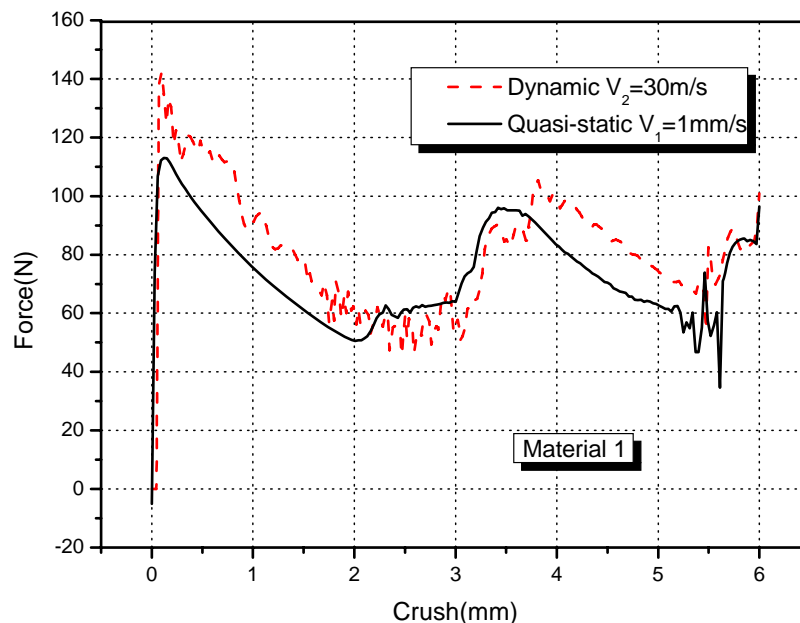
Figure 2.27 Dynamic and quasi-static force/crush curves of square tube made of Material 1
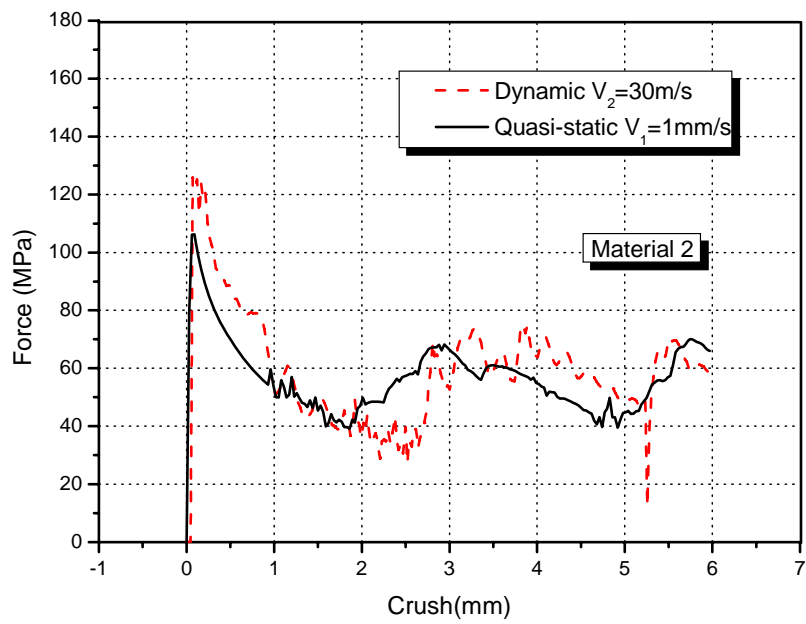
Figure 2.28 Dynamic and quasi-static force/crush curves of square tube made of Material 2
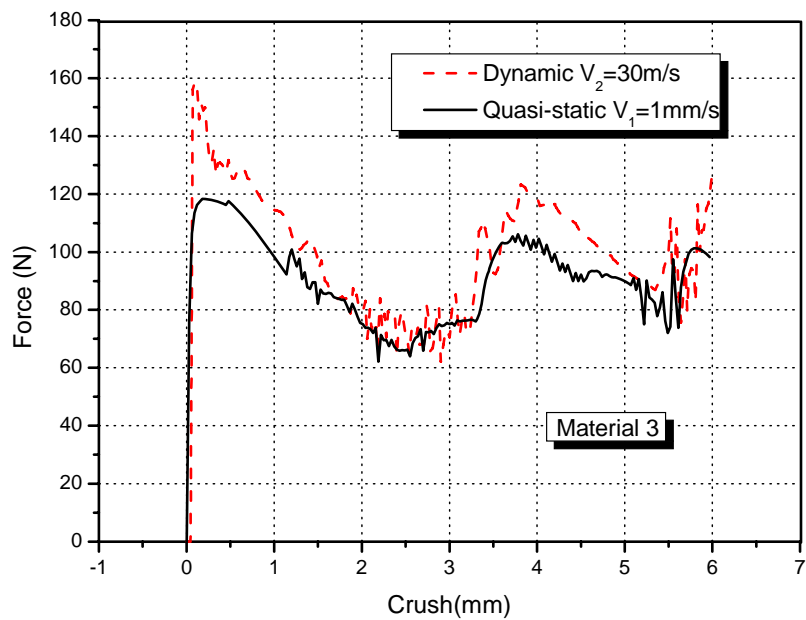
Figure 2.29 Dynamic and quasi-static force/crush curves of square tube made of Material 3

2.4 Lateral inertia effect in the out-of-plane crushing of honeycombs

2.4.1 Simplified cell-model of honeycomb

Honeycomb is a typical two-dimensional structure composed of unit *Y* configurations. The scheme of its cross section is shown in Figure 2.30. In order to reduce the calculation cost, a simplified model with only one *Y* configuration is established (denoted as cell-model) to reveal the deformation mechanism of this basic structure under out-of-plane compression as well as its dynamic enhancement behavior. It is compared in Chapter 6 of this thesis the simplified models with the full-size model in predicting the deformation behaviors of honeycombs. The cell-model is considered to be with shortages in properly simulating the symmetric boundary conditions which makes the overall force/crush curves exhibit large fluctuations comparing with the large-size model. However, simulations in this chapter aim at revealing the deformation details as well as the dynamic enhancement mechanism of honeycomb. A complex model with all the factors included should be avoided. Thus, the cell-model with only one *Y* configuration is employed to get the basic idea on honeycomb deformation under out-of-plane compression.
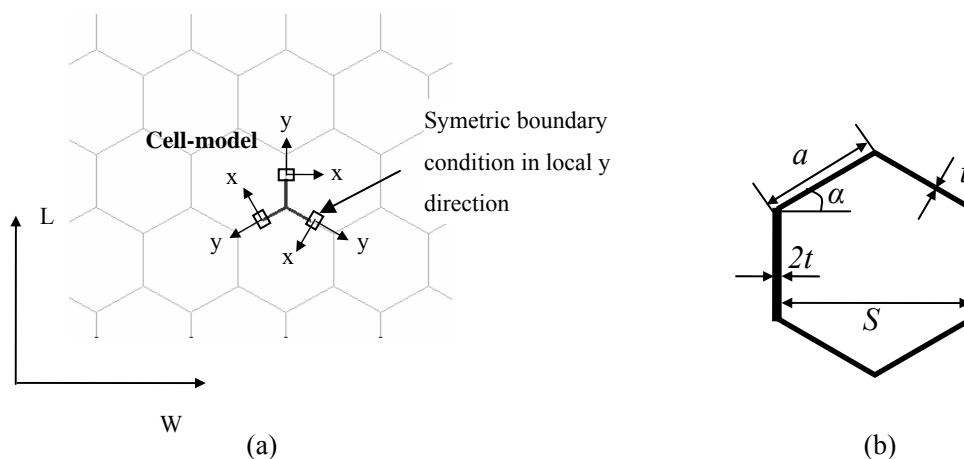
Figure 2.30 Scheme of honeycomb cross section and the unit cell-model

The cell-models installed in this study include different cell-size, cell-wall thickness and base material. The geometric parameters of all the models are listed in Table 2.2 and the base materials are the same to the ones used in square tube.

Table 2.2 Summary of geometric parameters and base materials of honeycomb cell-model

	Half side length $a/2$(mm)	Cell width S(mm)	Cell-wall thickness t(μm)	Model height h(mm)	Base material
Model 1	0.75	2.6	76	15	Material 1
Model 2	1.833	6.35	76	15	Material 1
Model 3	1.833	6.35	40	15	Material 1
Model 4	1.833	6.35	20	15	Material 1
Model 5	1.833	6.35	76	15	Material 2
Model 6	1.833	6.35	76	15	Material 3

The model is also discretized by 4-node doubly curved thick shell elements with a reduced integration, finite membrane strains, and active stiffness hour-glass control (S4R). 5 integration points is set through the cell-wall thickness are employed. An element size of 0.1mm is employed in order to get refined stress strain distributions. This honeycomb cell-model has totally 8114 elements.

The honeycomb cell-model is loaded in the same way to the square tube model. Two loading velocities with V_1=1mm/s for quasi-static loading and V_2=30m/s for dynamic loading are applied by the rigid loading plates. Symmetric boundary conditions are performed on the three non-intersecting edges of each cell wall in local y-direction (as shown in Figure 2.30). General contact with frictionless tangential behavior is defined for the whole model excluding the contact pairs of rigid planes and cell-model, which are redefined by surface-to-surface rough contact to make sure that no slippage occurs.

The way to introduce initial imperfections into the cell-model is also same to the square tube model. Buckling analysis on these two size cell-model is performed firstly to get the buckling modes of every order. The mode 20 with magnitude same to cell-wall thickness is introduced into the small cell-size model (a=0.75mm), and mode 15 for the other cell-model with a=1.833mm. The cell-models with initial imperfections introduced are shown in Figure 2.31.

The quasi-static simulations for cell-model is also finished by ABAQUS/Explicit + Mass scaling technique, and the time increment of Δt=5×10^{-6}s is employed.

<center>（a）   （b）</center>
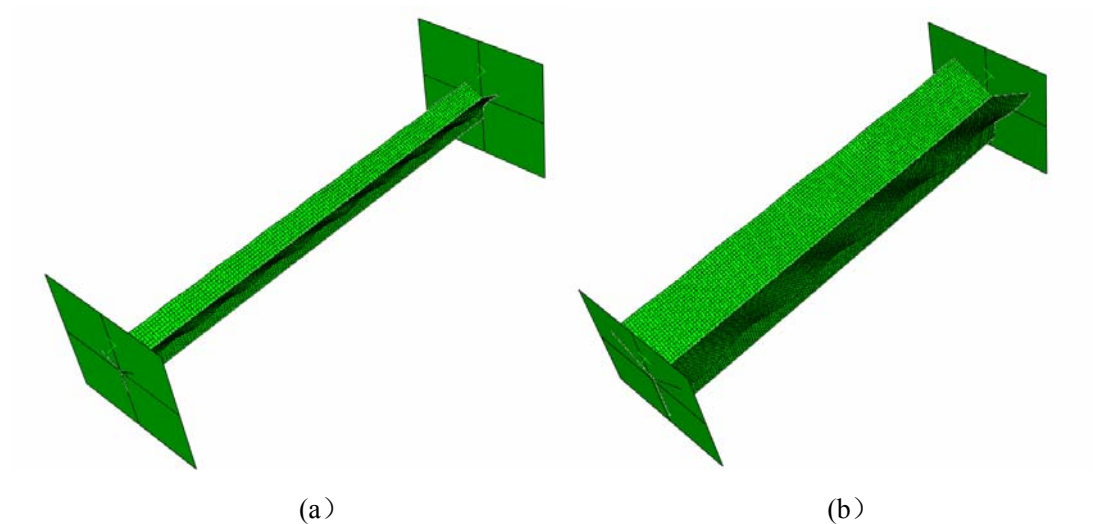
Figure 2.31 Two honeycomb cell-model with different cell-size (initial imperfection introduced)

2.4.2 Deformation details of cell-model and the dynamic strength enhancement

In the past decades, many researchers have paid much attention on the deformation mechanism of honeycombs[28-32]. Wu and Jiang[29] examined in detail the deformation process of honeycombs under out-of-plane compression. The half wavelength of each fold in successive folding process is determined. They also presented a deformation mechanism related to the formation of plastic hinge on cell walls. Mohr and Doyoyo[30] divided the honeycomb specimen under out-of-plane compression into the crushed part and the uncrushed part. The successive folding process develops with the moving of the interface of these two parts and it is believed that the macroscopic behavior of honeycombs is actually decides by the properties of this interface region. They carefully examined the unstable buckling behavior in the local interface region and proposed a deformation-induced microstructural imperfections mechanism to describe the collapse deformation process of honeycombs.

The initial collapse of honeycomb is also attributed to the buckling of cell walls, which are similar to the tube model. Thus, the dynamic enhancement of the initial peak of overall carrying capacity of cell-model can be also explained by the same concept of lateral inertia effect as in double-plate model and will not be repeated here.

As to the successive crushing process, it has been illustrated in square tube model that the corner region supports most of the external loadings and the bending of

<center>52</center>

this part determines the successive peak load in folding process, thus, the analysis on the cell-model should also be focused on the intersection line of three walls in the *Y* configuration.

Figure 2.32 shows the force/crush curve of a cell-model. Large fluctuation with each wave representing one fold formation is observed. We take the formation of the third and the forth fold for examples to illustrate the successive folding system of honeycomb under out-of-plane compression. The deformation sequence of the basic *Y* configuration is shown in Figure 2.33 (only the thick wall is displayed for sake of illustration clarity).
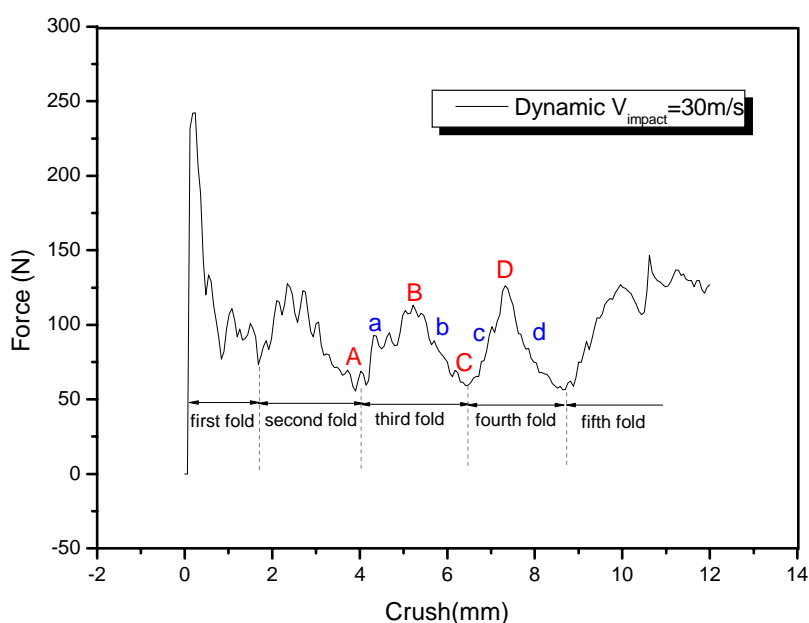
Figure 2.32 Force-displacement curve of honeycomb cell-model

The formation of the third fold begins from point *A* in Figure 2.32. At this moment, the first and the second folds have completely bended and the material of the third fold begins to support loading (Figure 2.33 (a)). The continuous axial deformation of the third fold enables the carrying capacity of the cell-model to increase gradually (Segment *a* in Figure 2.32 and the deformation image in Figure 2.33 (b)). During this process, the intersection line (as shown in Figure 2.33(a)) and its adjacent region remains straight, while the plate region has been bended significantly. The peak load of the third fold is reached (Point *B* in Figure 2.32) when the intersection line and its adjacent region begin to bend (as show in Figure 2.33 (c)), which is also an unstable deformation process as in square tube model. After this successive peak point, the overall carrying capacity decreases dramatically (segment *b*

in Figure 2.32) and the corresponding deformation of the cell model is characterized with the bending of intersection region (as shown in Figure 2.33 (c)). When the carrying capacity of the cell-model reaches the trough C in Figure 2.32, the fourth fold initiates and will repeat the above-mentioned process, i.e. the C-c-D-d process in Figure 2.32 and the deformation sequence in Figure 2.33 (e)-(h).

A

(a)

a

(b)

B

(c)

b

(d)

C   c

(e)   (f)

D   d

(g)   (h)
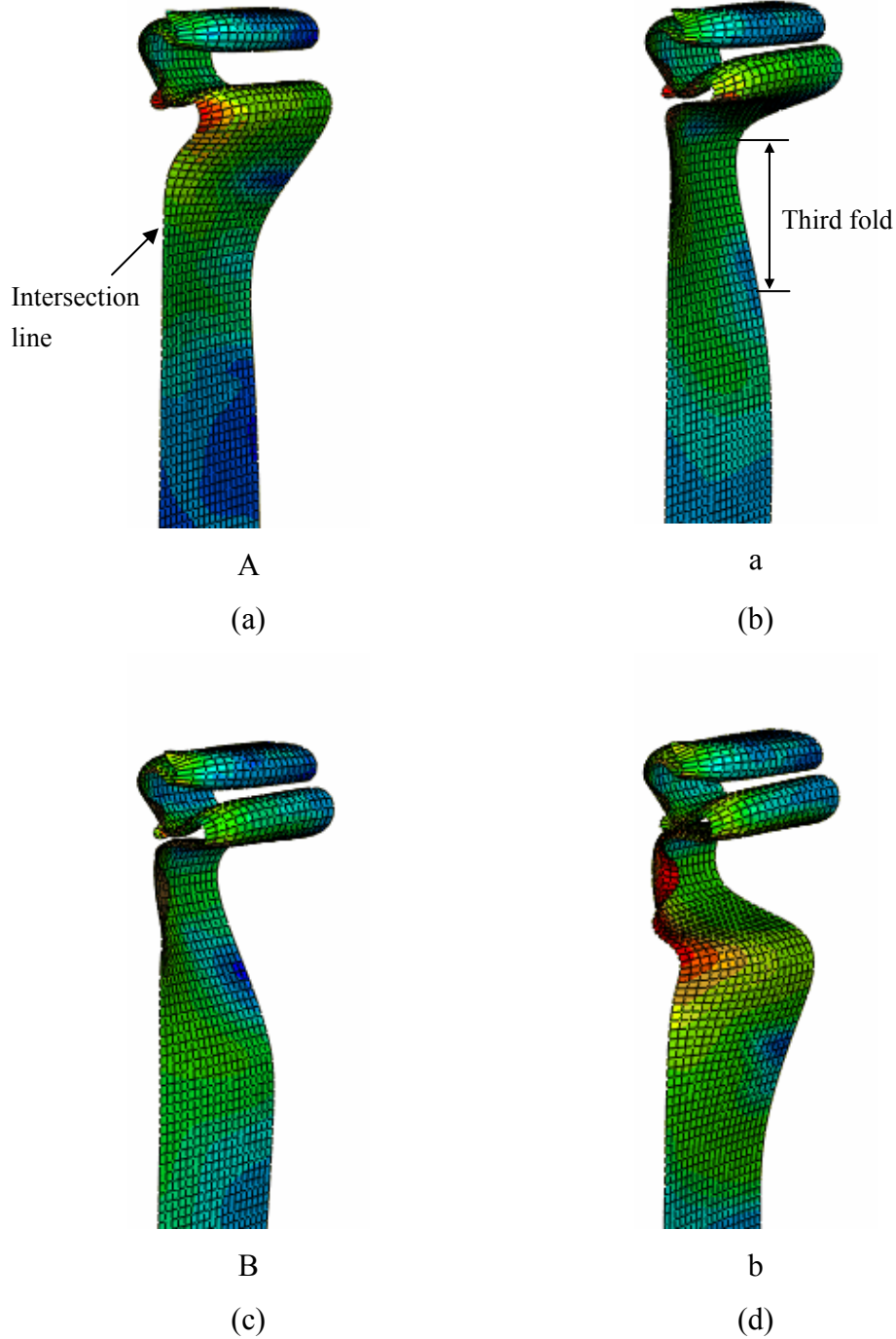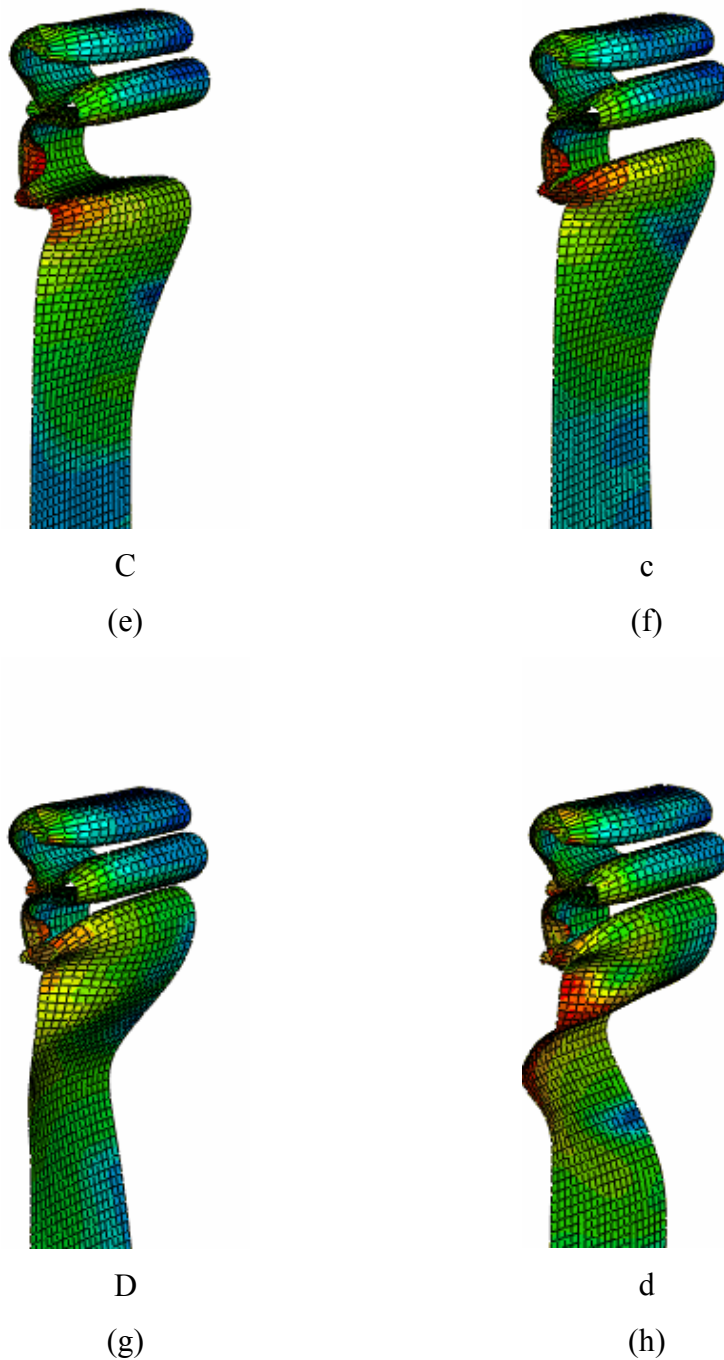
Figure 2.33 Formation of the third and the fourth folds of honeycomb cell-model

The successive crushing process of cell-model is of great similarity with the one of square tube as illustrated in Section 2.2. Thus, the mechanism of dynamic enhancement of square tube can be adapted to cell-model similarly. In fact, we do find similar proofs of the inertia effect model in explaining the dynamic enhancement of the cell-model, e.g. the lateral velocities of the intersection line of the cell-model at

the moment of collapse display an increasing trend with the increasing axial loading velocity, and the stress and strain profiles on the cell wall are also elevated at dynamic loading because of the collapse delay induced by lateral inertia effect (these similar results of cell-model is not redisplayed). Thus, the adaptability of inertia effect model in honeycomb cell-model is also validated.

2.4.3 Definitions

It is found that ABAQUS is able to simulate the inertia effect in double-plate model, tube model and honeycomb cell-model during dynamic crushing process. In this simulation work on honeycomb cell-model, further studies on the influences of cell-size, cell-wall thickness and base material on dynamic enhancement of honeycomb strength are performed subsequently, which on the one hand is going to validate again the adaptability of the inertia effect model by indicating the role of strain hardening behavior of base material, and on the other hand to estimate the capability of FEM in simulating the complex nonlinearity, the unstable buckling deformation and structural inertia effect. The calculating cases are listed in Table 2.2.

For honeycomb, we mainly concern about its initial collapse peak value and the successive crushing plateau strength. Thus, in order to clarify quantitatively the dynamic enhancement of calculated model, the quasi-static and dynamic results in terms of pressure/crush curves (defined as the force/crush curves divided by cross sectional area, see details in Section 3.2) are compared at two loading stages. Stage I is under elastic deformation from zero crush to the position of initial peak. In this stage, the initial peak value that determines the peak load in energy absorbing design of honeycombs is concerned. Stage II is the subsequent plateau stage which covers the rest part of the pressure/crush curve after the initial peak, which is the main loading stage for absorbing energy. In this stage, the average strength of the plateau is calculated by dividing the curve area of stage II (absorbed energy) by corresponding crush length, which gives:

$$\overline{p} = \frac{1}{\delta_{\max} - \delta^*} \int_{\delta^*}^{\delta_{\max}} p d\delta \qquad 2.11$$

where δ^* denotes the crush value at the point of the initial peak for each of the overall pressure/crush curve. $\delta_{\max}$ is the maximum crush of the corresponding crushing duration.

Accordingly, we can also define the dynamic enhancement rate γ to describe the phenomenon of honeycomb strength enhanced under impact loading from quasi-static loading. γ is defined for the initial peak at stage I and the average strength of plateau at Stage II respectively as follows:

$$\gamma_{peak} = \frac{p^{\mathrm{d}}_{peak} - p^{s}_{pead}}{p^{s}_{peak}} \tag{2.12}$$

$$\gamma_{plateau} = \frac{\Delta\overline{p}}{\overline{p}^{s}} = \frac{\overline{p}^{d} - \overline{p}^{s}}{\overline{p}^{s}} \tag{2.13}$$

2.4.4 Calculating results with different cell-size

Figure 2.34 displays the dynamic and quasi-static pressure/crush curves for two cell-models with different cell-size respectively (Model 1 and Model 2 in Table 2.2). It is found that both the initial peak and the successive plateau strength show an obvious dynamic enhancing behavior. However, the quasi-static curve from small cell-size model (Model 1) shows a softening behavior after the initial peak, which is different from the other curves in this study. This phenomenon is considered to have relations with the deformation mode of cell-models in successive crush process. In the quasi-static calculating result of Model 1, no distinct partition is found between the crushed part and the uncrushed part and the well-known crushing deformation mode with successive folding system is no longer adaptive. The material is compressed in axial direction even before the crush front arrives. Figure 2.35 shows the deformation configurations of this small cell-size model under dynamic loading and quasi-static loading, in which, the dynamic model keeps its untouched region straight during the successive crush process, while, the quasi-static model is globally compressed and bended after the second fold formation. Thus, the calculated dynamic enhancement during the whole successive crushing stage for Model 1 may contain large deviation, and the influence of cell-size in this loading period on the dynamic enhancement rate is suspectable. As to the reason of this deformation mode transformation, it may be related to the employment of ABAQUS/Explicit + Mass scaling technique and the choice of time increment, which need further investigation in next work.

In fact, until the second fold formation, the softening behavior of small cell-size model is not significant and the deformation mode of these two models is almost the same. It is suggested to investigate the dynamic enhancement by comparing the

second peak values of dynamic and quasi-static loading. Then, it is found that the dynamic enhancement of small cell-size model (about 3.5MPa) is higher that the one of large cell-size model (about 1.4MPa). However, because the strength of small cell-size model is also of higher value, the dynamic enhancement rate of small cell-size model (14.6%) is actually lower than the one of large cell-size model (22.1%).

(a)

(b)
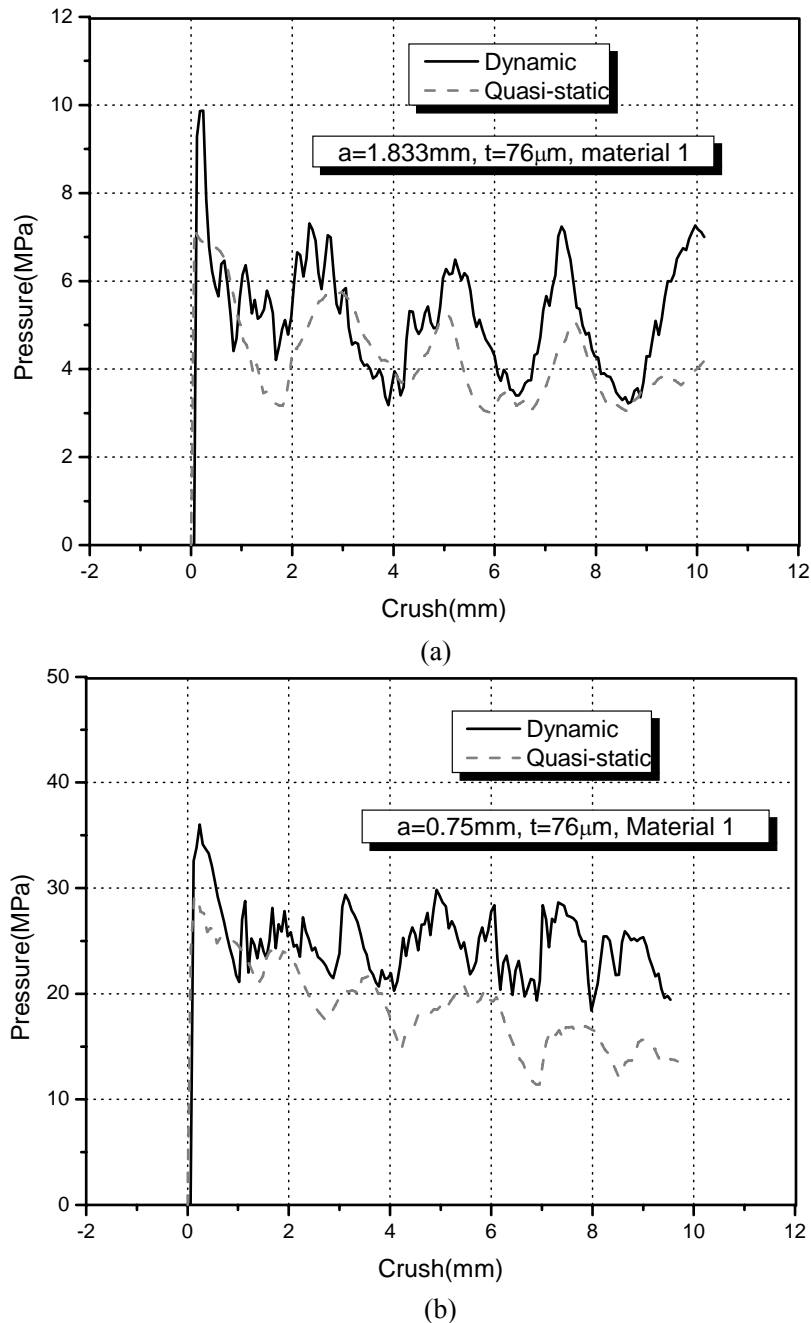
Figure 2.34 Force-displacement curve of honeycomb cell-model with different cell-size
(a)a=1.833mm; (b)a=0.75mm

(a）

(b）
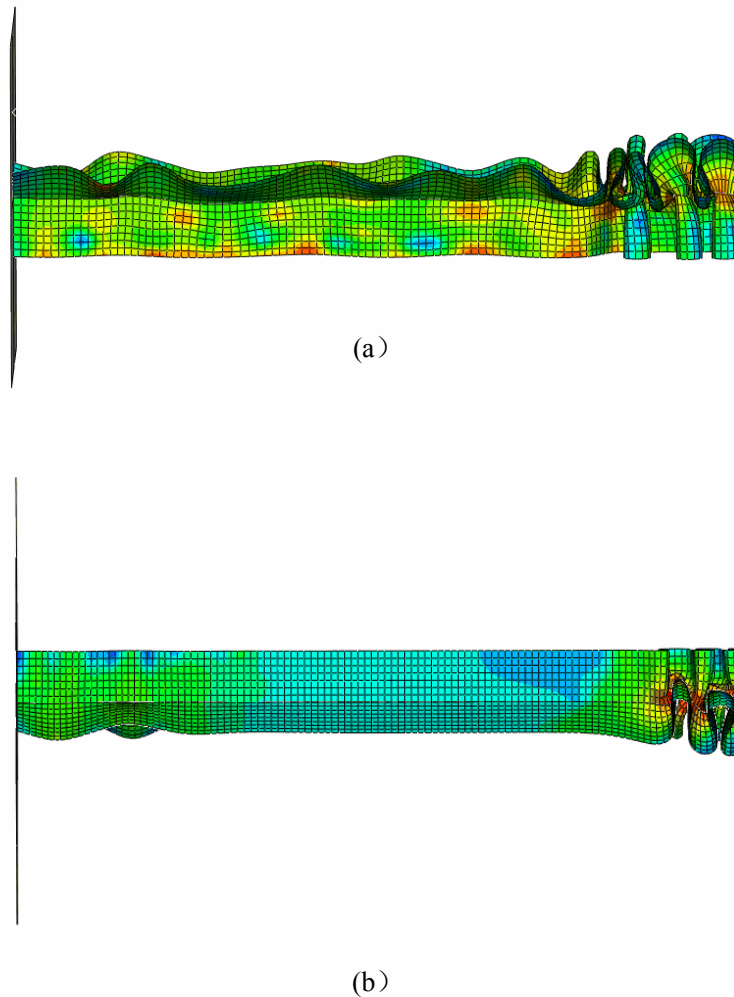
Figure 2.35 Deformation configurations of the small cell-size model under quasi-static (a) and dynamic loading

2.4.5 Calculating results with different cell-wall thickness

Figure 2.36 displays the comparison between dynamic and quasi-static curves for three cell-models with different cell-wall thickness (Model 2, 3 and 4 in Table 2.2). It can be seen that thickness has significant influence on the strength of honeycombs, i.e. both the dynamic and quasi-static curves become much lower when the thickness decreases. For the dynamic enhancement, it is found in the three figures that all the initial peaks are elevated, while for the successive plateau strength, the curves from Model 3 and Model 4 with thinner cell walls show limit dynamic enhancing behavior comparing with the thick cell-wall model (Model 2).

Further investigations are performed by calculating the average plateau strength for the presented curves. The dynamic and quasi-static strength as well as the dynamic enhancement rate for these three models are listed in Table 2.3. It is found that the dynamic enhancement Δp of thick cell-wall model is much higher than the one from thin wall model. However, because of the much lower strength of thin wall models, the dynamic enhancement rate is close to each other.

Table 2.3 Summary of dynamic and quasi-static average plateau strengthes of honeycomb with different cell-wall thickness

	t=76μm	t=40μm	t=20μm
Dynamic average plateau strength	5.16	1.87	0.586
Quasi-static average plateau strength	4.22	1.55	0.49
Dynamic enhancement Δp	0.94	0.32	0.096
Dynamic enhancement rate γ	22.3%	20.6%	19.6%

(a）

(b）

(c)
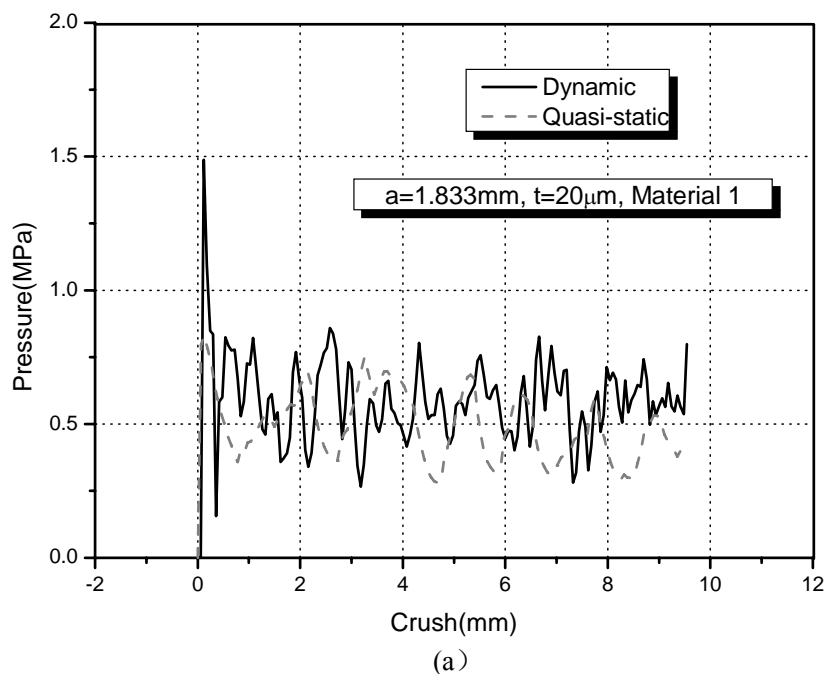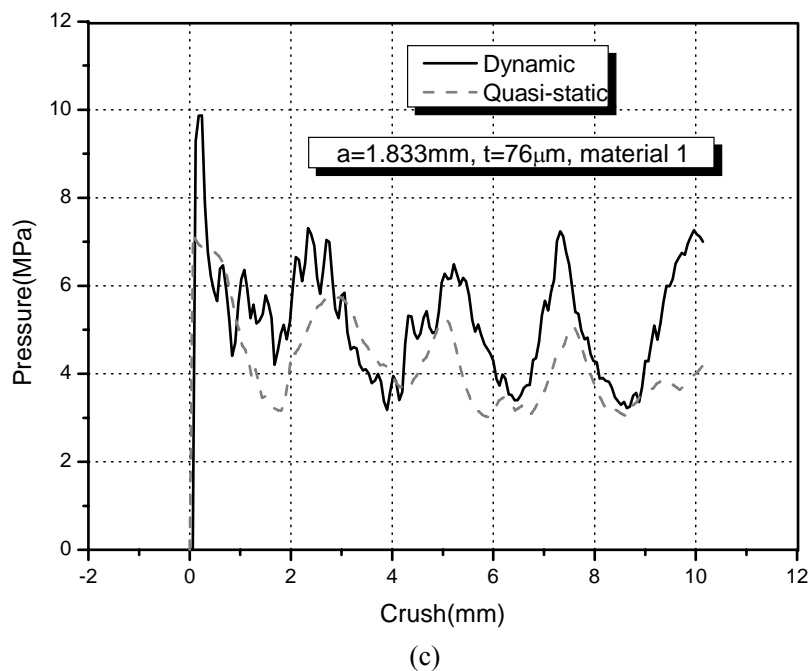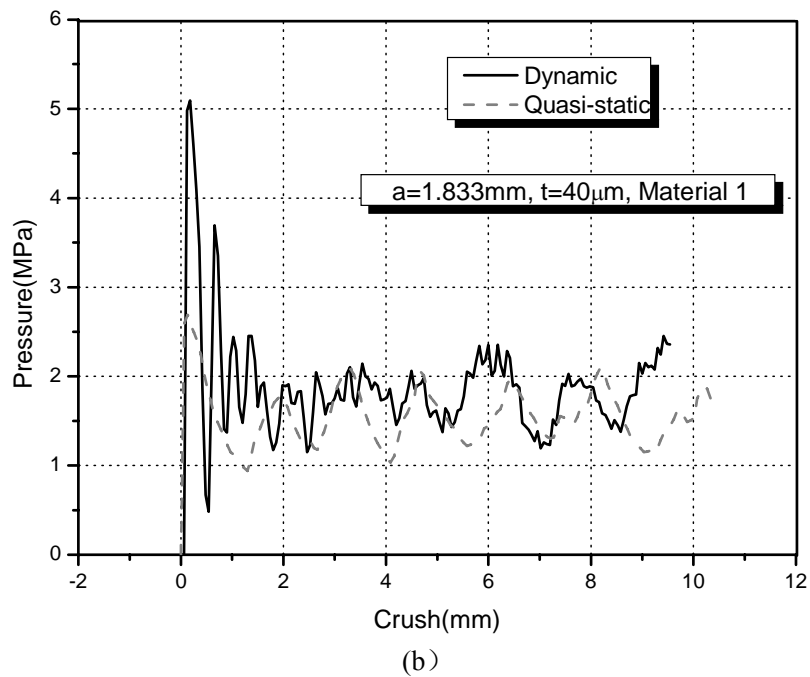
Figure 2.36 Force-displacement curve of honeycomb cell-model with different cell wall thickness (a) t=20μm; (b) t=40μm; (c) t=76μm;

2.4.6 Calculating results with different base material

Figure 2.37 displays the dynamic and quasi-static curves of honeycomb cell-models made of different base materials, which are denoted as Material 1, 2, and 3 with different strain hardening behaviors as shown in Figure 2.17 and Table 2.1.

Similarly to the results of square tube, the quasi-static initial peak is rarely affected by the change of the base material, while, the dynamic one becomes higher when the strain hardening exponent of the base material increases. This phenomenon can be explained similarly as in square tube model.

For the dynamic enhancement in successive crush stage, the average strength of the plateau is calculated for all the curves and listed in Table 2.4. It is found that different strain hardening behavior will result in different Δp, and the higher the strain hardening exponent is, the larger Δp becomes. However, the material with higher strain hardening exponent always possesses a higher strength and the dynamic enhancement rate is actually without significant difference. It is recalled that the dynamic enhancement rates for tube model made of different base materials display certain difference to each other, which is failed to calculate out in these honeycomb cell-models.

In fact, as illustrated in Section 2.2, it should be emphasized again that the influence of strain hardening exponent of base material will affect not only the stress elevation when collapse delay occurs, but also the collapse delay itself. Thus, the dynamic enhancement of honeycomb strength induced by a higher strain hardening behavior will be partly counteracted by the decrease of collapse delay duration.

Table 2.4 Summary of dynamic and quasi-static average plateau strengths of honeycomb made of different base materials

	Material 1	Material 2	Material 3
Dynamic average plateau strength	5.16	3.95	6.07
Quasi-static average plateau strength	4.22	3.31	4.77
Dynamic enhancement Δp	0.94	0.64	1.3
Dynamic enhancement rate γ	22.3%	19.3%	19.6%

(a)

(b)

(c)
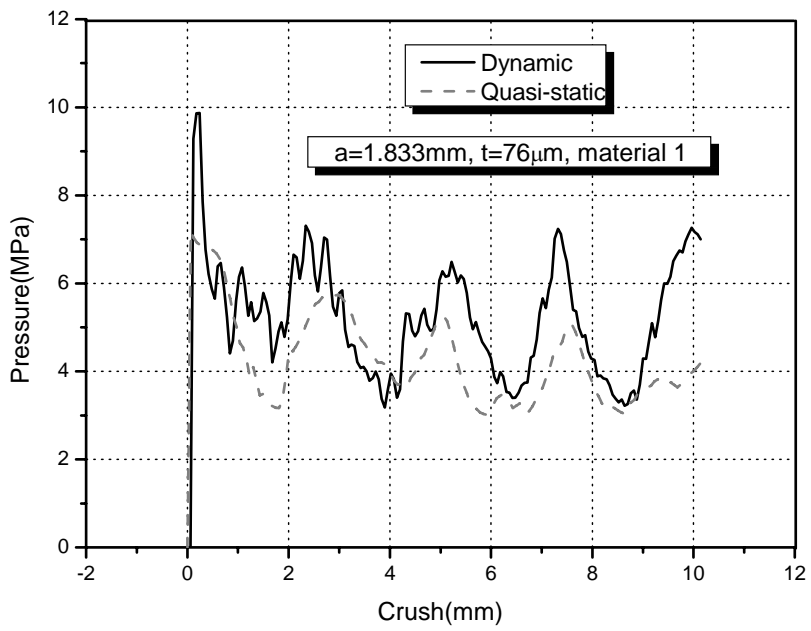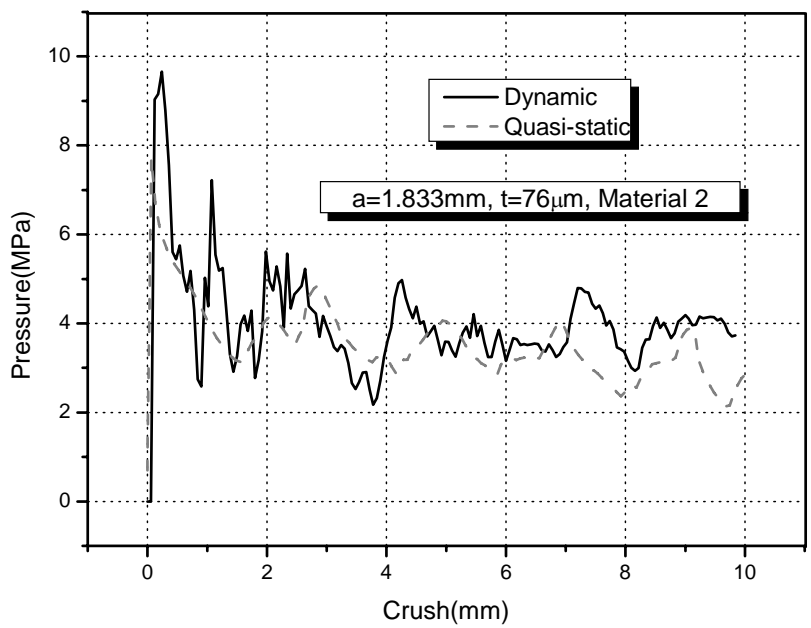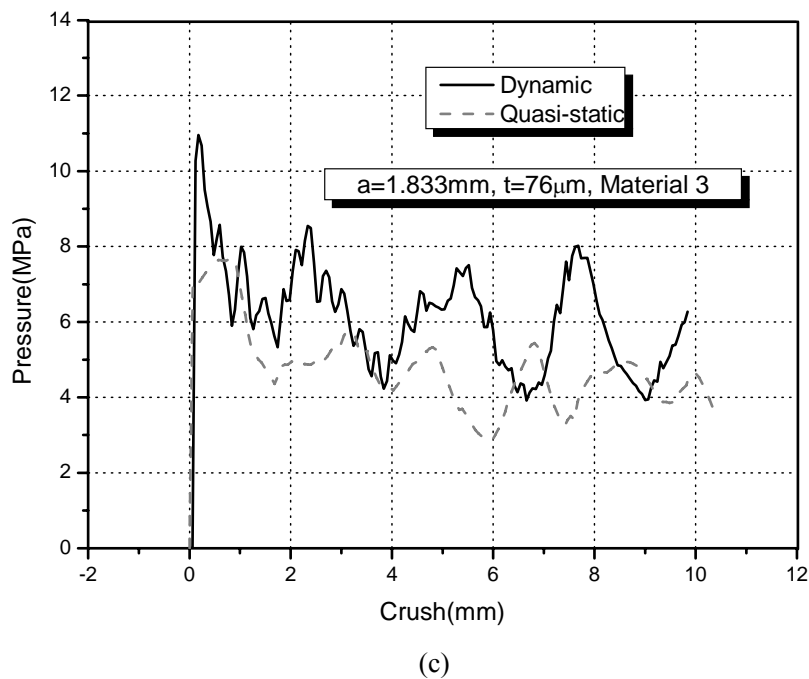
Figure 2.37 Force-displacement curve of honeycomb cell-model made of different base
materials (a)Material 1; (b)Material 2;(c)Material 3

2.5 Summary

This chapter performed a series of simulations by means of FEM in order to investigate the dynamic enhancement of thin-walled structures.

In Section 2.1, with the review of previous works on inertia effect mechanism of dynamic enhancement of cellular material, a simple model basing on lateral inertia effect from Zhao and Abdennadher was introduced. The main idea is as follow: the collapse of a thin-walled structure is an unstable deformation process and will be delayed by lateral inertia effect when under high loading velocity. Thus, the axial strain at the collapse moment will be higher under dynamic loading than under quasi-static loading. Further more, if the base material is of strain hardening property, the axial stress as well as the carrying capacity of the structure will also be elevated under dynamic loading.

In Section 2.2, validating work on this simple inertia effect model was firstly performed on a micro-size double-plate model by FEM. The capability of ABAQUS in calculating the unstable buckling problem was checked, and the shortages and advantages of different numerical methods were compared.

64

Section 2.3 checked further the adaptability of this inertia effect model in micro-size square tube. Detailed deformation process of square tube under compression was obtained firstly. Then, the dynamic enhancement was explained by the collapse delay effect, which was related with the lateral inertia of corner region material under dynamic loading. Finally, the influence of strain hardening exponent of base material on the dynamic enhancement rate confirmed again the correctness of this explanation.

In Section 2.4, we installed a simplified honeycomb cell-model containing only a unit Y configuration. Basing on this model, the deformation mechanism of honeycombs was studies firstly and the applicability of abovementioned inertia effect model to this cell-model is confirmed. Then, the influences of honeycomb cell-size, cell-wall thickness, and base material on the dynamic enhancement were investigated.

This chapter installed three models in thin-walled structure by means of FEM to investigate the mechanism of dynamic enhancement in such structures. Generally speaking, FEM is able to calculate out this dynamic enhancing phenomenon caused by inertia effect and many observations are in good agreement with the proposed explanation basing on lateral inertia effect. However, some limitations still exist for this numerical method. On the one hand, for the calculations of quasi-static problem, ABAQUS/Explicit + Mass scaling technique is employed. Although the validating work has been performed in the double-plate model, its accuracy and capability in calculating more complex problems is still not yet confirmed, especially when the problem is strongly dependent on inertia effect. On the other hand, the successive crushing process of honeycomb is very complicated and many factors, which may affect its mechanical behavior, are difficult to be included or completely described in the simulation works, such as the randomly distributed initial imperfections, the delamination of honeycomb cell walls as well as the damage behavior etc. This will also bring limitations to these numerical analyses.

References

[1]   J. J. Harrigan, S. R. Reid, C. Peng, Inertia effects in impact energy absorbing materials and structures. Int. J. Impact Engng. 22 955-979 (1999).

[2]   S. R. Reid, C. Peng, Dynamic uniaxial crushing of wood. Int. J. Impact Engng.19 531-570 (1997).

[3]   P. J. Tan, J. J. Harrigan. Inertia effects in uniaxial dynamic compression of a closed cell aluminium alloy foam. Mat. Sci. Tech. 18, 480-488 (2002).

[4]   P. J. Tan, S. R. Reid. J. J. Harrigan, Z. Zou S. Li, Dynamic compressive strength properties

of aluminium foams. Part I: experimental data and observations. J. Mech. Phy. Solids 53, 2174-2205 (2005).

[5]   P. J. Tan, S. R. Reid. J. J. Harrigan, Z. Zou S. Li, Dynamic compressive strength properties of aluminium foams. part II: shock theory and comparison with experimental data and numerical models. J. Mech. Phy. Solids, 53, 2206-2230 (2005).

[6]   S. L. Lopatnikov, and B. A. Gama. Dynamic of metal foam deformation during Taylor cylinder-Hopkinson impact experiment. Composite structure 61, 61-71 (2003).

[7]   S. L.Lopatnikov, B. A. Gama, High-velocity plate impact of metal foams. Int. J. Impact Engng. 30, 421-445 (2004).

[8]   D. D. Radford, N. A. Fleck. The use of metal foam projectiles to simulate shock loading on a structure. International Journal of Impact Engineering 31, 1152-1171 (2005).

[9]   I. Elnasri, S. Pattofatto, H. Zhao, H. Tsisiris, F. Hild, Y.Girard. Shock enhancement of cellular structures under impact loading: Part I Experiments. J. Mech. Phy. Solids 55, 2652-2671 (2007).

[10]   S. Pattofatto, I. Elnasri, H. Zhao, H. Tsisiris, F. Hild, Y.Girard. Shock enhancement of cellular structures under impact loading: Part II analysis. J. Mech. Phy. Solids 55, 2672-2686 (2007).

[11]   Z. Zou, S. R. Reid, P. J. Tan, S. Li, J. J. Harrigan, Dynamic crushing of honeycombs and features of shock fronts. Int. J. Impact Engng. 36. 165-176 (2009).

[12]   Y. D. Liu, J. L. Yu, Z. J. Zheng, J. R. Li, A numerical study on the rate sensitivity of cellular metals. Int. J. Solids Structs 46 3988-3998 (2009).

[13]   L. J. Gibson, M. F. Ashby. Cellular material: structure and properties, 2nd Ed., Cambridge University Press, Cambridge, UK. (1997).

[14]   V. S. Deshpande, N. A. Fleck. High strain rate compressive behaviour of aluminium alloy foams. Int. J. Impact Engng. 24, 277-298 (2000).

[15]   O. Zhou, R. R. Mayer, Characterization of aluminium honeycomb material failure in large deformation compression, shear and tearing. J. Engng. Mater. Tech. 124, 412-420 (2002).

[16]   B.Budiansky, J. W. Hutchinson, Dynamic buckling of imperfection sensitive structures. In: Proceedings of 11th international congress of Applied Mechanics. Springer Verlag. Munich (1964).

[17]   G. Gary, Dynamic buckling of an elastoplastic column. Int. J. Impact Engng. 2, 357-375 (1983).

[18]   C. R. Calladine, and R. W. English. Strain-rate and inertia effects in the collapse of two types of energy-absorbing structures. Int. J. Mech. Sci. 26(11-12), 689-701 (1984).

[19]   L. L. Tam, and C. R. Calladine. Inertia and strain rate effects in a simple plate structure under impact loading. Int. J. Impact Engng. 11, 689-701 (1991).

[20]   Z. Y. Gao, T. X. Yu, G. Lu, A study on type II structures. Part I: a modified one-dimensional mass-spring model. Int. J. Impact Engng. 31, 895-910 (2005).

[21]   Z. Y. Gao, T. X. Yu, G. Lu, A study on type II structures. Part II: dynamic behavior of a chain of pre-bent plates. Int. J. Impact Engng. 31, 911-926 (2005)

[22]   M. Langseth, O.S.Hopperstad, T. Berstad. Crashworthiness of aluminium extrusions:

validation of numerical simulation, effect of mass ratio and impact velocity. Int. J. Impact Engng. 22 829-854 (1999).

[23] M. Langseth, O.S.Hopperstad, Static and dynamic axial crushing of square thin-walled aluminium extrusions. Int. J. Impact Engng. 18 949-968 (1996).

[24] X. Y. Su, T. X. Yu, S. R. Peng. Inertia-sensitive impact energy-absorbing structures. Part I: Effects of inertial and elasticity. Int J impact Engng 16(4), 651 (1995).

[25] X. Y. Su, T. X. Yu, S. R. Peng. Inertia-sensitive impact energy-absorbing structures. Part II: Effects of strain rate. Int J impact Engng. 16(4), 673 (1995).

[26] H.Zhao, G.Gary, crushing behavior of aluminium honeycombs under impact loading. Int. J. Impact Engng. 21, 827-836 (1998).

[27] H. Zhao, S. Abdennadher, On the strength enhancement under impact loading of square tubes made from rate insensitive metals. Int. J. solids and struct. 41, 6677-6697 (2004).

[28] L. J. Gibson, M. F. Ashby. Cellular material: structure and properties, 2nd Ed., Cambridge University Press, Cambridge, UK. (1997).

[29]   E.Wu, W.S.Jiang, Axial crush of metallic honeycombs, Int. J. Impact Engng. 19, 439-456(1997).

[30] D.Mohr, M.Doyoyo, Nucleation and propagation of plastic collapse bands in aluminium honeycomb. J. Appl. Phy. 94, 4, 2262-2270 (2003).

[31] J. Zhang, M. F. Ashby, The out-of-plane properties of honeycombs. Int. J. Mech.Sci. 34, 475-489 (1992).

[32] S. T. Hong, D. Pan, Quasi-static crush behavior of aluminium honeycomb specimens under compression dominant combined loads. Int. J. Plasticity 22: 73-109 (2006).

Chapter 3 Experimental studies on dynamic enhancement of aluminium honeycombs

3.1 Larger diameter soft Hopkinson bar technique

3.1.1 Introduction of classical Hopkinson bar

The Hopkinson bar experimental technique finds its origin in the pioneering efforts of John Hopkinson (1872) and then his son, Bertram Hopkinson (1914)[1]. Later, Davies (1948)[2] found a method to measure the displacement of the free end of the bar using a parallel-plate condenser which enabled the direct measurement of the stress (or strain) profile in the Hopkinson bars. The third important contribution was made by Kolsky (1949)[3], who used two elastic bars with the specimen sandwiched in between, and created a technique which is known as the split Hopkinson bar method (also known as Kolsky bars). Hereafter, researchers developed this technique to adapt many special loadings. For example, Harding et al (1960)[4], Lindhol and Yeakley (1968)[5] achieved to perform tension experiments by hopkinson bars. Duffy et al[6] and Baker and Yew (1966)[7] presented the split Hopkinson torsion experiments. Nemat Nasser et al (1991)[8] proposed a technique in Hopkinson experiments to load the specimen by a single compressive pulse. Lennon and Ramesh (1998)[9] designed the high temperature Hopkinson bar systems which can be used to investigate the material behaviors under coupling of high loading rate and high temperature. Up to now, Hopkinson bar experimental technique has been widely use in testing the dynamic behavior of material in the strain rate range between 10^2/s-10^4/s.

A typical SHPB set-up is shown in Figure 3.1. It is composed of long input and output bars with a short specimen placed between them. A projectile launched by a gas gun strikes the free end of the input bar and develops a compressive longitudinal incident wave $\varepsilon_i(t)$. Once this wave reaches the bar/specimen interface, part of it $\varepsilon_r(t)$, is reflected, whereas the other part goes through the specimen and develops the transmitted wave $\varepsilon_t(t)$ in the output bar. Two gauges are cemented at the midpoints of input and output bars to record those three basic waves which can be used to investigate the constitutive behavior of the specimen.
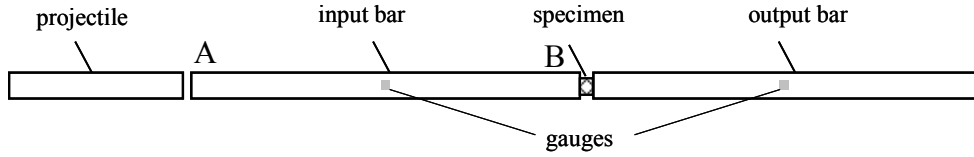
Figure 3.1. The classic compression split Hopkinson bar

It is well known that the Split Hopkinson Bars are based on several assumptions: (1) the stress wave in the bars is based on the one-dimensional wave propagation theory; (2) the stress and strain fields in the specimen are homogenous; (3) the inertia effects of specimen under dynamic loading can be ignored; (4) the friction between the specimen and the ends of input and output bars is neglectable. With these assumptions, the strain rate, strain and stress of the tested specimen can be calculated from the basic waves as follows:

$$\dot{\varepsilon}_s(t) = \frac{2C_0}{L}\varepsilon_r(t) \qquad\qquad 3.1$$

$$\varepsilon_s(t) = \frac{2C_0}{L}\int_0^t \varepsilon_r(t)dt \qquad\qquad 3.2$$

$$\sigma_s(t) = E\left(\frac{A}{A_s}\right)\varepsilon_t(t) \qquad\qquad 3.3$$

where $\varepsilon_r(t)$ and $\varepsilon_t(t)$ are respectively the reflected and transmitted strain pulses measured by strain gauges, A_s is the area of specimen cross section, L is the specimen length, A and E are respectively the cross section area and Young's Modulus of Hopkinson bars, C_0 is the elastic wave speed in bars.

3.1.2 Specific problems in cellular materials testing

The classical Hopkinson bar experimental technique has important advantages in testing the dynamic behavior of materials comparing with the other dynamic experimental methods such as an accurate data measurement. However, it is designed originally only for metallic materials, while for the brittle materials or soft materials, some modifications are necessary.

As to cellular materials, some particular problems will come forth due to the nature of these materials.

First of all, cellular materials have inhomogeneous micro-structures and the specimen should include enough unit cells to reduce as much as possible the data scatter in measurements, thus, large diameter bars are desired to hold large size specimen. It is commonly believed that each direction of the cellular material specimen should include at least six or seven unit cells to neglect the size effect. In this study, we performed part of the honeycomb experiments on $\Phi = 60$mm Hopkinson bars with the dimensions of rectangular specimen of $25 \times 40 \times 40$mm, which includes 39 complete cells on cross section (*S*=6.32mm, *S* is defined in Figure 3.8). Another part of the experiments is about small cell honeycombs (*S*=2.6mm～*S*=5.1mm), which were performed on a $\Phi=30$mm Hopkinson bars system. With the hexagonal specimens of 30mm in diameter, the small cell honeycomb specimens include 20~90 complete cells, and the experimental results show good reproducibility.

Secondly, the strength of cellular materials is usually very low, which results in a poor impedance match with the Hopkinson bars. The incident wave is mostly reflected at the bar/specimen interface and only a small part of it goes through the specimen as transmitted wave, which makes the accurate measurement of this small amplitude transmitted wave much difficult. This problem is solved by employing low impedance viscoelastic Hopkinson bars as proposed by Zhao et al[10] and Zhao and Gary[11]. In our study, the $\Phi=60$mm Hopkinson bars are made of Nylon with density $\rho＝1200$kg/m^3, wave speed C_0=1700m/s. the $\Phi=30$mm Hopkinson bars are made of PMMA and the density and wave speed are respectively 1250kg/m^3 and 2193m/s. They provide an improvement of impedance of about 200 times that of a classical steel bars.

Finally, the deformation process of cellular material is much different with solid metals. They undergo mostly non-uniform deformation with localization in micro-structures. For example, honeycomb under out-of-plane crush is in a successive folding deformation mode. Thus, the obtained information of strain rate, strain and stress from data process of classical Hopkinson bars are not suitable to describe the defomation behavior of cellular materials, which necessitates the definition of new parameters (see in 3.1.5).

3.1.3 Large diameter, viscoelastic Hopkinson bar technique

Two Hopkinson bar systems were employed in this study to perform the uniaxial out-of-plane compression on honeycombs. One is the $\Phi=60$mm Nylon Hopkinson bars in LMT (Laboratoire de Mécanique et Technologie, ENS-Cachan), with input and

output bars of 3m in length(as shown in Figure 3.2). Another one is in the Laboratory of Dynamics and Strength, NPU, which is made of PMMA with bar diameter of 30mm, and length of 2m. The use of large diameter, viscoelastic Hopkinson bars is helpful to increase the reliability and accuracy of experimental results, but will also introduce complications related to an important wave dispersion effect.

Figure 3.2. The Nylon Hopkinson bars with diameter Φ=60mm

3.1.4 Wave dispersion correction of large diameter viscoelastic Hopkinson bars

The Hopkinson bar experiments are based on one-dimensional elastic wave theory. According to this theory, the strain signals are not only known at the measuring points but everywhere in the bar because an elastic wave can be shifted to any distance without distortion if knowing the wave propagation theory. However, the one-dimensional wave theory is not always true especially for the large diameter bars, and the geometrical effects should be taken into account.

In fact, there are wave dispersion effects during the propagation of waves in elastic or viscoelastic bars. For the classical Hopkinson bars, the ratio of bar diameter and length is small enough and this wave dispersion effect is negligible. While for the Φ60mm$\times$3m Nylon Hopkinson bars and the Φ30mm$\times$2m PMMA Hopkinson bars used in this study, the wave dispersion effects should be taken into account. Moreover, because of the viscoelastic properties of the bars, the traditional correction methods on wave dispersion are not suitable anymore.

A correction based on the Pochhammer (1876) and Chree's (1889)[12] longitudinal wave solution for an infinite cylindrical elastic bar has been proposed (Davies (1948)[2]; Follansbee and Franz (1983)[13]; Gorham (1983)[14]; Gong et al, (1990)[15]; Gary et al (1991)[16]). The harmonic wave propagation in an infinite cylindrical rod has been well studied in the elastic case, even numerically (Davies (1948)[2]; Mindlin and McNiven (1960)[17]). In the case of a viscoelastic bar, a similar harmonic wave solution has been given for a cylindrical infinite bar made of the material described by the Voigt model (Coquin (1964)[18]). Zhao and Gary[19] generalized Pochhammer and Chree's longitudinal wave propagation equation to the case of cylindrical bars made of any linear viscoelastic material. This method is also employed in the experiments of this study and is introduced briefly as follows:

In Pochhammer and Chree's longitudinal wave solutions, the displacement $u(X,t)$ is written in the following form:

$$u(X,t) = \frac{1}{2\pi} \int_{-\infty}^{+\infty} u^*(X,\omega) e^{-i\omega t} d\omega \qquad 3.4$$

with
$$u^*(X,\omega) = u'^*(r,\theta,\omega) e^{i\xi(\omega)z} \qquad 3.5$$

where $u(X,t)$, $u^*(X,\omega)$ are, respectively, displacement as a function of time and of the frequency. X denotes the space vector, the components of which are r, θ, z in cylindrical coordinates.

Considering a linear viscoelastic media, the constitutive law can be written in the frequency domain as follows (Bland (1960))[20].

$$\bar{\bar{\sigma}}^*(\omega) = \lambda^*(\omega) tr\left(\bar{\bar{\varepsilon}}^*(\omega)\right)\bar{\bar{1}} + 2\mu^*(\omega)\bar{\bar{\varepsilon}}(\omega)^* \qquad 3.6$$

where $\bar{\bar{\sigma}}^*(\omega)$, $\bar{\bar{\varepsilon}}^*(\omega)$, $\lambda^*(\omega)$, $\mu^*(\omega)$ are respectively, the stress tensor, the strain tensor, and two material coefficients.

The harmonic wave displacement components $u^*(X,\omega)$ must satisfy the following dynamic equation of motion[21]:

$$\mu^*(\omega)\nabla^2\vec{u}^*(\bar{X},\omega) + \left(\lambda^*(\omega) + \mu^*(\omega)\right)\nabla\nabla \cdot u^*(\bar{X},\omega) = -\rho\omega^2\vec{u}^*(\bar{X},\omega) \qquad 3.7$$

where ∇ is the gradient operator and ρ is the mass density.

As in the case of an elastic medium, each wave displacement component $u^*(X,\omega)$ can be expressed as a function of a dilatational wave part $\Phi^*(X,\omega)$ and a distortional wave part $H^*(X,\omega)$[22].

$$\vec{u}^*(\bar{X},\omega) = \nabla\Phi^*(\bar{X},\omega) + \nabla\times\vec{H}^*(\bar{X},\omega) \qquad 3.8$$

Substituting Equation 3.8 into the dynamic equation of motion 3.7, the following Equation 3.9 and 3.10 can be obtained. These equations must be satisfied, respectively, by the dilatational and the distortional parts of the displacement.

$$\nabla^2 \Phi^*\left(\bar{X},\omega\right) + \frac{\omega^2}{C_1^2}\Phi^*\left(\bar{X},\omega\right) = 0 \qquad 3.9$$

$$\nabla^2 \bar{H}^*\left(\bar{X},\omega\right) + \frac{\omega^2}{C_2^2}\bar{H}^*\left(\bar{X},\omega\right) = 0 \qquad 3.10$$

with

$$C_1 = \sqrt{\left(\lambda^*(\omega) + 2\mu^*(\omega)\right)/\rho} \qquad 3.11$$

$$C_2 = \sqrt{\mu^*(\omega)/\rho} \qquad 3.12$$

For an infinite cylindrical bar, the assumption of the harmonic wave (Equation 3.8) means that the displacement must show an exponential variation along the axial direction of the bar. The solutions $\Phi^*(X,\omega)$ and $H^*(X,\omega)$ are then expressed in the following form:

$$\Phi^*\left(\bar{X},\omega\right) = \varphi(r,\theta,\omega)e^{i\xi z} \qquad 3.13$$

$$\bar{H}^*\left(\bar{X},\omega\right) = \left[h_r(r,\theta,\omega)\bar{e}_r + h_h(r,\theta,\omega)\bar{e}_h + h_z(r,\theta,\omega)\bar{e}_z\right]e^{i\xi z} \qquad 3.14$$

Furthermore, in the case of a longitudinal wave, owing to the axi-symmetry of the problem, the functions $\Phi^*(X,\omega)$ and $H^*(X,\omega)$ are written in a simpler form:

$$\Phi^*\left(\bar{X},\omega\right) = \varphi(r,\omega)e^{i\xi z} \qquad 3.15$$

$$\bar{H}^*\left(\bar{X},\omega\right) = h_h(r,\omega)e^{i\xi z}\bar{e}_h \qquad 3.16$$

Introducing $\Phi^*(X,\omega)$ and $H^*(X,\omega)$ given by Equation 3.15 and 3.16 into Equation 3.9 and 3.10, the function $\varphi(r,\omega)$ and $h_h(r,\omega)$ are determined. We have then[21].

$$\varphi^*\left(\bar{X},\omega\right) = A(\omega)J_0(\alpha r)e^{i\xi z} \qquad 3.17$$

$$\bar{H}^*\left(\bar{X},\omega\right) = B(\omega)J_1(\beta r)e^{i\xi z}\bar{e}_h \qquad 3.18$$

where

$$\alpha^2 = \frac{\rho\omega^2}{\lambda^*(\omega) + 2\mu^*(\omega)} - \xi^2 \qquad 3.19$$

$$\beta^2 = \frac{\rho \omega^2}{\mu^*(\omega)} - \xi^2 \qquad\qquad 3.20$$

and J_0、 J_1 are zero and first order Bessel's functions; $A(\omega)$ and $B(\omega)$ are coefficients.

The displacement can then be calculated from Equation 3.8. The homogeneous boundary conditions at the external surface of the bar ($r=a$), which must be satisfied by the solutions 3.17 and 3.18, lead to an equation relating ξ and ω as in the elastic case. A viscoelastic frequency equation is then obtained. This equation takes the same form as the classical one obtained in elasticity. However, in the present case, the argument ξ in the equation is a complex number:

$$f(\xi) = (2\alpha/a)(\beta^2 + \xi^2)J_1(\alpha \cdot a)J_1(\beta \cdot a) - (\beta^2 - \xi^2)^2$$
$$J_0(\alpha \cdot a)J_1(\beta \cdot a) - 4\xi^2 \alpha \cdot \beta \cdot J_1(\alpha \cdot a)J_0(\beta \cdot a) = 0 \qquad 3.21$$

In this equation, ξ represents the complex change in phase function of the frequency ω. Its real part gives the relation between the frequency and the associated phase velocity and its imaginary part gives the relation between the frequency and the associated attenuation coefficient.

Equation 3.21 has the same form for both elastic case and viscoelastic case. The solution of Equation 3.21 in elastic case has already been completed[20] and employed by many researchers for wave dispersion correction in Hopkinson experiments[13-15]. The main concept is as follows: At first, the signals collected by strain gauges are transformed from the time domain to the frequency domain by Fast Fourier Transform. Then, the stress wave dispersion is corrected in this frequency domain according to the function ξ from solving Equation 3.21. At last, the signals which have been corrected in the frequency domain are transformed back to time domain by FFT^{-1}.

For the case of viscoelasticity, Zhao and Gary[19] proposed a numerical method to solve Equation 3.21 by Newton's iterative method, and the detailed illustration can be found in reference[19]. The correction method of wave dispersion is the same with the one in elastic case:

Assuming that the displacement in an infinite linear viscoelastic rod is $u(r,z,t)$, the position of strain gauges is at $r=r_0$. Thus, once the dispersion relation is known, one can calculate from the measured wave $u_z^m(t)$ the wave $u_z^i(t)$ propagated at a distance Δz. Using the components in the z direction of $u(r,z,t)$ at the surface of the bar, one can write $u_z^m(t)$ and $u_z^i(t)$ as follows :

$$u_z^m(t) = \frac{1}{2\pi} \int_{-\infty}^{+\infty} \bar{u}_z(r_0, \omega) e^{i[\xi(\omega)z_0 - \omega t]} d\omega \qquad 3.22$$

$$u_z^i(t) = \frac{1}{2\pi} \int_{-\infty}^{+\infty} \bar{u}_z(r_0, \omega) e^{i[\xi(\omega)(z_0 + \Delta z) - \omega t]} d\omega \qquad 3.23$$

The wave shifting procedure is then performed numerically by the *FFT*:

$$u_z^i(t) = FFT^{-1}\left\{e^{i\xi(\omega)\Delta z} FFT\left[u_z^m(t)\right]\right\} \qquad 3.24$$

3.1.5 Data processing of SHPB for cellular materials

It has been demonstrated that the cellular materials undergo mostly non-uniform deformation with localization in micro-structures. For example, when honeycomb under out-of-plane compression is crushed in a successive folding deformation mode, the stress and strain distribution in the specimen along cell axis direction is far away from uniform. Thus, the employment of strain and stress from data process of classical Hopkinson bars which are obtained on the base of uniformity assumption are not suitable to describe the deformation behavior of cellular materials.

In fact, in the Hopkinson experiments, the three basic waves will make the knowledge of input and output forces and velocities on the two specimen faces. Further with the assumption of deformation uniformity, these quantities can be used to obtain the aforementioned stress and strain information of the specimen, while here for the cellular materials with non-uniform deformation pattern, these quantities are employed directly for describing the dynamic behavior of this kind of materials. The associated forces and particle velocities can be calculated as follows:

$$F_{input}(t) = S_b E(\varepsilon_i(t) + \varepsilon_r(t)) \qquad V_{input}(t) = C_0(\varepsilon_i(t) - \varepsilon_r(t))$$

$$F_{output}(t) = S_b E \varepsilon_t(t) \qquad V_{output}(t) = C_0 \varepsilon_t(t) \qquad 3.24$$

where F_{input}, F_{output}, V_{input} and V_{output} are forces and particle velocities on specimen faces. S_b, E and C_0 are respectively the cross section area, Young's modulus of the bars and the longitudinal wave speed. $\varepsilon_i(t)$, $\varepsilon_r(t)$, $\varepsilon_t(t)$ are the wave signals at the bar/specimen interface. It is worth noting that the Hopkinson bars here are considered as only a loading and measuring system which can give accurately the force and deformation informations on the specimen faces and without considering the deformation characteristics (uniform or non-uniform) of the sandwiched specimen between the input and the output bars. Chapter 4 of this thesis is also based on this concept to design a biaxial loading device with the SHPB system.

Figure 3.3(a) and (b) show respectively the forces and velocities on the input and output faces of honeycomb specimen under uniaxial compression experiments.
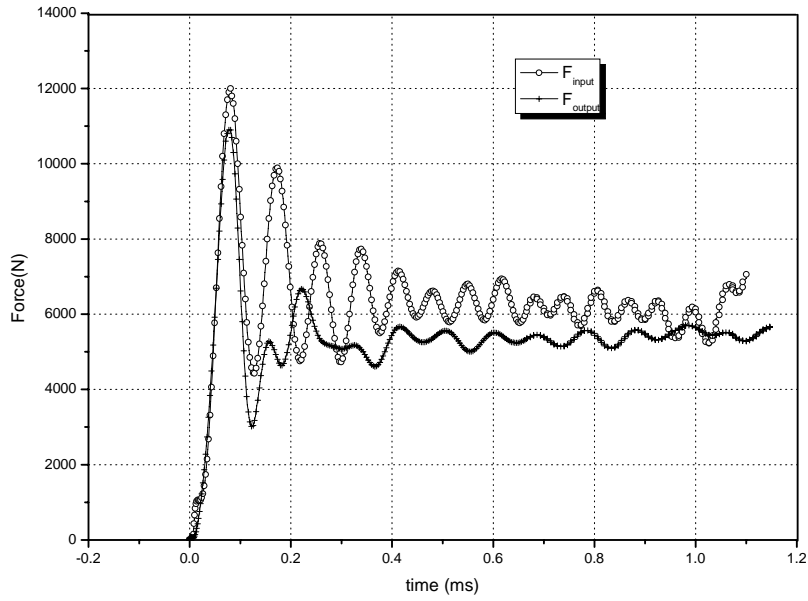
(a)
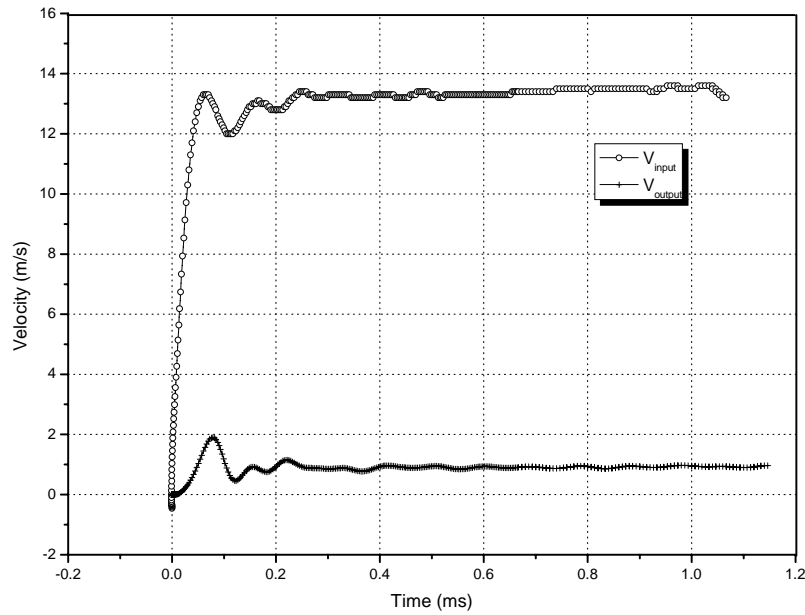
(b)

Figure 3.3 Input and output forces(a) and velcocities(b) in a uniaxial compression test

As a stress strain homogeneous field assumption is not really valid in the case of soft cellular materials with localized deformation mechanism, we use only the mean pressure $p(t)$ as a function of the crush $\Delta(t)$ to give an overall idea of the behavior of this kind of material[23]. They are defined as:

$$p(t) = (F_{input}(t) + F_{output}(t))/2S_s \qquad 3.25$$

$$\Delta(t) = \int_0^t (V_{output}(\tau) - V_{input}(\tau))d\tau \qquad 3.26$$

where S_s is the apparent area of the specimen face contacting to the beveled bars.

The pressure/crush curve of honeycomb specimen for this test is obtained and shown in Figure 3.4.
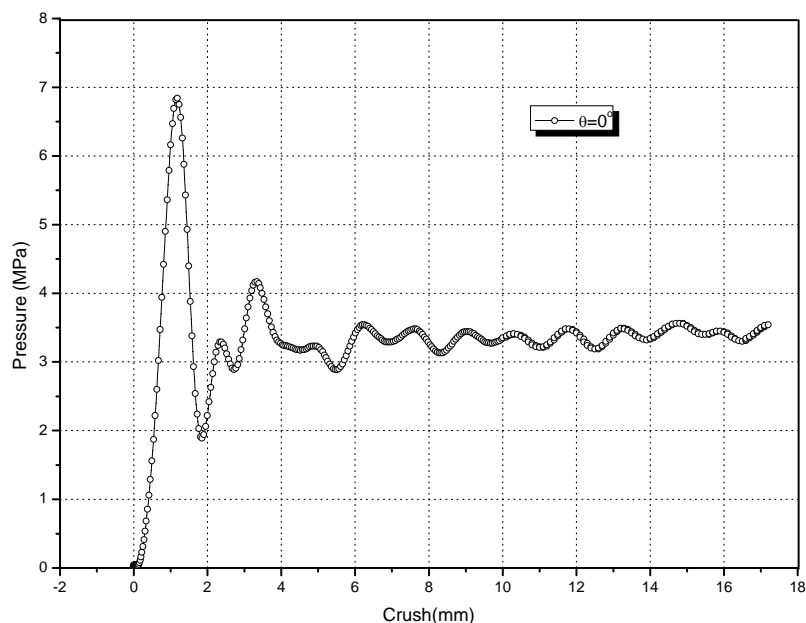
Figure 3.4. Pressure/crush curve under uniaxial compression

3.2 Quasi-static experiments for cellular materials

The quasi-static experiments under uniaxial compression were also performed in order to make a dynamic/quasi-static comparison to study the phenomenon of dynamic enhancement. A universal Tension/Compression INSTRON3369 machine in LMT is employed (as shown in Figure 3.5) for the large cell-size honeycomb made of 5052 aluminium. The experiments on small cell-size honeycomb of 3003 aluminium were performed on the universal Tension/Compression Machine of CSS88010 in Laboratory of Dynamics and Strength, NPU (as shown in Figure 3.6).

A high-speed camera (Camera Photron APX-RS as shown in Figure 3.7) was used in both quasi-static and dynamic experiments to capture the deformation configurations during the loading process. The highest resolution of this camera is 1024×1024 pixel, and the picturing speed is between 3000fps～250000fps.
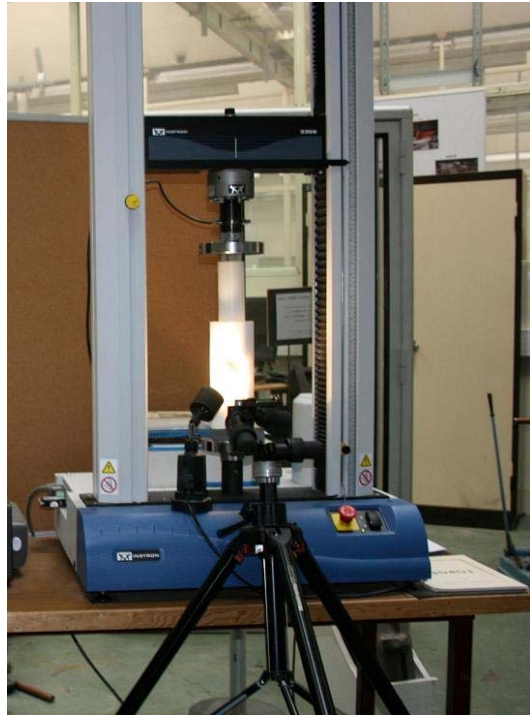
Figure 3.5 universal tension-compression INSTRON3369 machine

Figure 3.6 Universal tension-compression CSS88010 machine

Figure 3.7 High speed camera Photron APX-RS

3.3 Materials and specimens

The tested materials include a hexagonal honeycomb made of 5052 aluminium and five 3003 aluminium honeycombs with different cell-size and cell-wall thickness. The definitions of side length of hexagon a, single wall thickness t, the expansion angle α ($\alpha=30^{\circ}$ for all the honeycombs in this study), and a minimum cell diameter S are shown in Figure 3.8. The parameters of six honeycombs are listed in table 3.1 (including the geometric parameters and the relative density ρ^{*} which is defined as the ratio of the honeycomb density and the base material density).
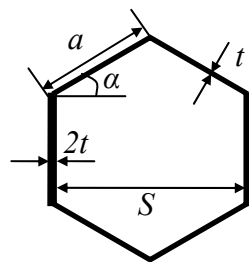
Figure 3.8 Geometry of the unit cell of hexagonal honeycomb

Table 3.1 Summary of the six honeycomb structures

	Base material	a(mm)	S(mm)	t(µs)	ρ^{*}(%)	V_{impact}(m/s)
1	3003Al	1.5	2.6	50	5.13	25
2	3003Al	2	3.46	40	3.08	27
3	3003Al	2	3.46	60	4.61	27
4	3003Al	2.5	4.33	60	3.70	26
5	3003Al	3	5.2	50	2.57	28
6	5052Al	3.67	6.35	76	3.19	15

Honeycombs have three orthotropic directions denoted as T L W (as shown schematically in Figure 3.9). The T-direction, also known as the out-of-plane direction corresponds to the axes of the honeycomb cells and is the strongest direction. The other two directions (L and W) are so-called in-plane directions referred as the ribbon direction and the width direction of honeycomb. As honeycombs are mostly under out-of-plane compression in the application of energy absorbing, thus, the material behavior in T direction is of great interest in this study.

Cubic specimens with dimension of $25 \times 40 \times 40$mm in the directions of T L W respectively are used for the 5052 honeycombs. There are 39 complete cells on the cross section of this rectangular honeycomb specimen (as shown in Figure 3.9 (a)). Another specimen of 3003 honeycomb adopts hexagonal shape for the cross section in order to include as many as possible the complete cells. The circumcircle diameter of this hexagonal specimen is 30mm. Figure 3.9 (b) shows the structure of a 3003 honeycomb specimen with $a = 2$mm.

The impact velocities of projectile in these Hopkinson experiments are summarized in Table 3.1, where the velocities for 5052 honeycombs are about 15m/s, and the ones for 3003 honeycombs are between 25~28m/s.

In order to make a comparison with the dynamic experimental results, we also performed the quasi-static experiments on these honeycombs. Thereinto, the experiments for 5052 honeycombs were carried out on an Instron3369 machine with loading speed of 0.1mm/s, while the ones for 3003 honeycombs were on a CSS88010 machine with loading speed of 0.03mm/s.

It is noted that the dynamic loading velocities for these two kinds of honeycombs are not exactly the same, and so to the quasi-static experiments. This difference is due to the experimental conditions in two laboratories and will bring in difficulties to the study of dynamic enhancement on the honeycombs made of different base materials. However, as the magnitude of velocity difference is no more than an order, here in this study, we distinguish the loading velocities only by dynamic and quasi-static, and the influence of different impact velocities at dynamic loading or of the different compression speed in quasi-static experiments are ignored.
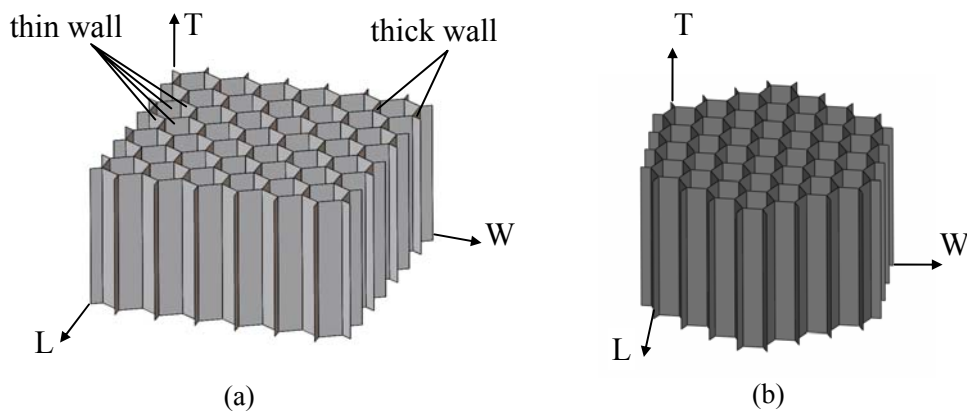
Figure 3.9 The constructed rectangular (a) and hexagonal(b) honeycomb specimens

3.4 Quasi-staic and dynamic experimental results

3.4.1 Reproducibility

As a honeycomb structure is always far from perfect, it includes all kinds of imperfections distributing randomly in the micro-structure, such as irregular cell geometry, uneven or pre-buckled cell-walls, wall thickness variation etc. These randomly distributed imperfections will affect the initial peak value of honeycomb strength significantly and bring in data scatter to the experiments. Besides, the dynamic loading will also increase the uncertainty of the experiments. Thus, the reproducibility of the experiments on honeycombs should be checked.

In the uniaxial compression experiments, we performed three repeating experiments for each dynamic case and two for quasi-static cases. Figure 3.10 shows the repeating pressure/crush curves for 5052 honeycomb under out-of-plane compression on the Φ=60mm Nylon Hopkinson bars and Figure 3.11 for the 3003 honeycomb with a=2, t=60μm on the Φ=30mm PMMA bars. It is indicated from the figures that these curves are in good agreement to each other at least in the large deformation crush period. The small dispersion at the initial deformation period for 3003 honeycomb in Figure 3.11 is probably due to the large initial imperfections of the specimens.
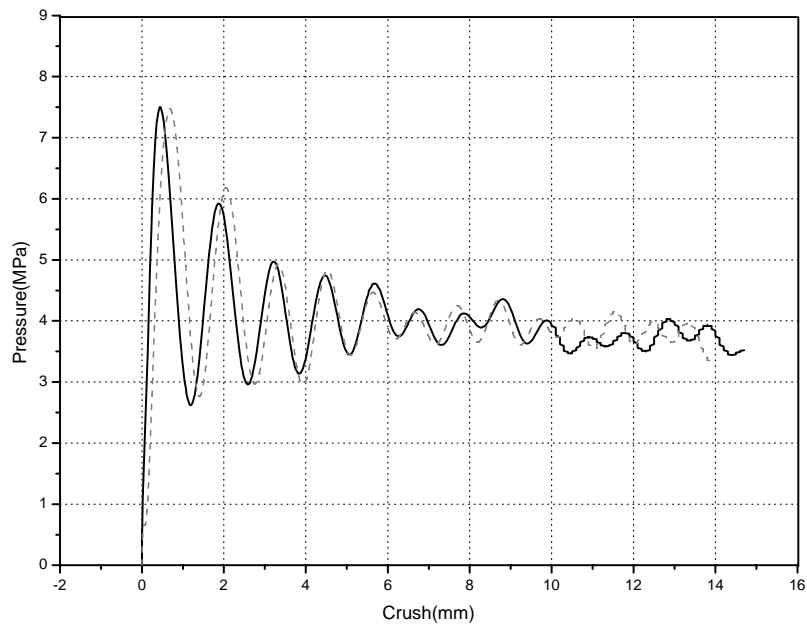
Figure 3.10 Reproducibility of impact experiment on 5052 honeycomb under uniaxial compression
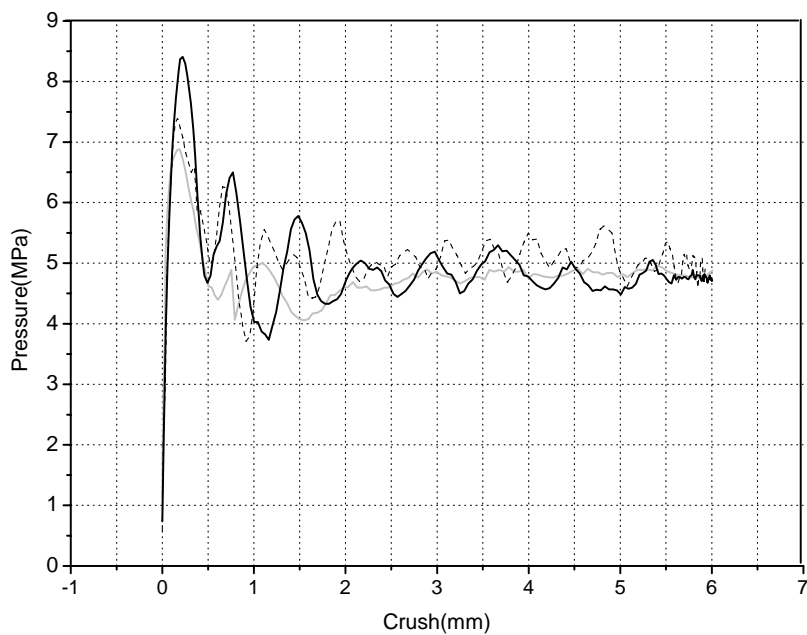
Figure 3.11 Reproducibility of impact experiment on 3003 honeycomb under uniaxial compression

The repeatability of quasi-static curves is even better than the dynamic ones which are with more fluctuations induced by wave dispersion in the Hopkinson bar experiments. The repeating quasi-static pressure/crush curves of 3003 honeycomb with a=2, t=60μm are displayed in Figure 3.12.
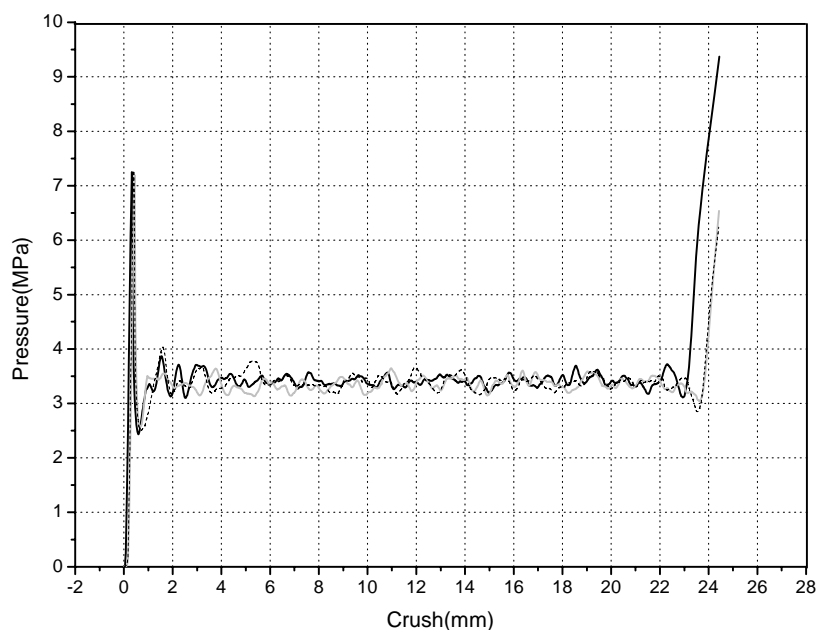
Figure 3.12 Reproducibility of quasi-static experiment on 3003 honeycomb under uniaxial compression

3.4.2 Dynamic enhancement of honeycombs

The uniaxial compressive pressure/crush curves of honeycombs under different loading rates are compared. It is found that the dynamic strengths are generally higher than the quasi-static ones for nearly all the specimens, thus, the strength of honeycomb under out-of-plane compression exhibits notable dynamic enhancement.

The dynamic and quasi-static pressure/crush curves for 3003 honeycomb with $a=2$, $t=40\mu m$ are shown in Figure 3.13. The quasi-static specimen undergoes much longer loading period comparing with the dynamic one and the associated curve includes integrally the elastic stage, the plateau stage and the densified stage. However, the dynamic loading duration is limited by the length of Hopkinson bars (a crush of only about 8mm is obtained), but can still be used to estimate the strength of honeycomb in the plateau stage. It can be seen from Figure 3.13 that the average strength of the plateau stage under dynamic loading is obviously higher than under quasi-static loading, and a significant dynamic enhancement is observed. While for the initial peak value of the pressure/crush curve, the result from quasi-static loading is higher than the one from dynamic. This abnormal phenomenon is probably because of the randomly distributed initial imperfections in honeycomb specimen which

introduces undesired data scatter of measurement. Thus, the peak values shown in Figure 3.6 cannot predict convincingly the influence of loading rate on the initial collapse behavior of honeycombs.
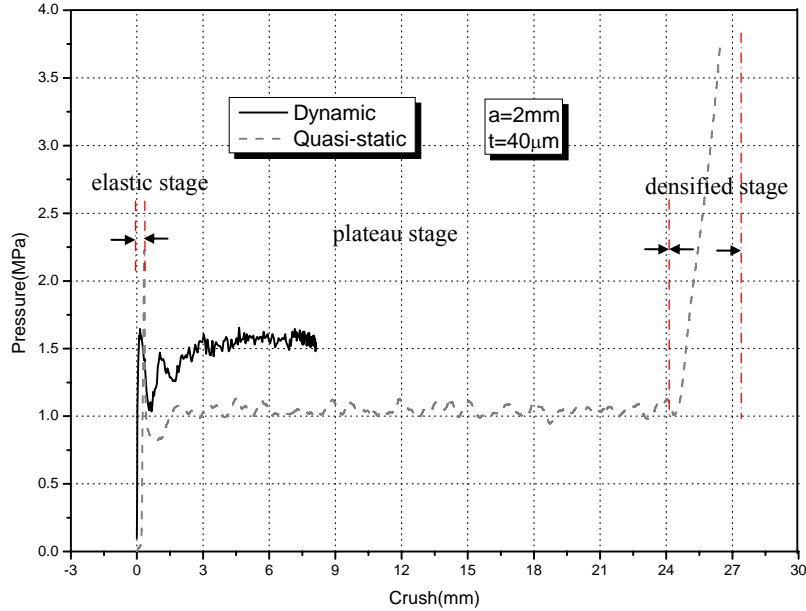
Figure 3.13 Dynamic enhancement of honeycomb pressure/crush curve

In the experiments, we mainly concern about the dynamic enhancement of honeycombs under successive crushing process. By employing the definitions of two loading stages as well as the dynamic enhancement rate in Section 2.4, the elevation of average plateau stress from quasi-static loading to dynamic loading is obtained. For the curves of 3003 honeycomb with a=2mm, t=40μm shown in Figure 3.13, the dynamic enhancement rate $\gamma_{plateau}$ at Stage II is 47.1%. It is summarized in Table 3.2 all the $\gamma_{plateau}$ for every experimental cases on six types of honeycomb.

Table 3.2 Summary of the parameters and experimental results of tested honeycombs

Cases	Base material	a/S (mm)	t (μm)	Relative density	$\overline{p}^s$ (MPa)	$\overline{p}^d$ (MPa)	$\Delta\overline{p}$ (MPa)	$\gamma_{plateau}$
1	3003	1.5/2.6	50	5.13%	2.30	2.88	0.58	25.2%
2	3003	2/3.46	40	3.08%	1.20	1.75	0.55	45.8%
3	3003	2/3.46	60	4.61%	4.00	5.51	1.51	37.8%
4	3003	2.5/4.33	60	3.70%	2.79	4.06	1.27	45.5%
5	3003	3/5.2	50	2.57%	1.24	1.96	0.72	58.1%
6	5052	3.67/6.35	76	3.19%	3.22	4.01	0.79	24.5%

Next, we are going to analyze the effects of cell-size, cell-wall thickness and the base material on honeycomb strength as well as its enhancement effect under dynamic loadings. In order to facilitate the comparison, all the quasi-static curves are cut off at crush of 8mm.

3.4.3 Influence of cell-size

By comparing Case 1 and Case 5 in Table 3.2 (with a=1.5mm, t=50μm and a=3mm, t=50μm), the influence of cell-size on honeycomb strength and $\gamma_{plateau}$ is clear. When the cell-size is doubled from a=1.5mm to a=3mm, the relative density of honeycomb decreases by 50%. It is found in Table 3.2 that the quasi-static strength for two honeycombs decreases by 46.1% which is close to the change of relative density. While for the dynamic strength, this value is only 31.9%. Thus, the dynamic enhancement rate $\gamma_{plateau}$ for these two honeycombs with different cell-size is also of obvious difference, where the one for large cell-size ($\gamma_{plateau}$＝58.1%) is much higher than the one for small cell-size($\gamma_{plateau}$＝25.2％).

Figure 3.14 displays the dynamic and quasi-static pressure/crush curves for these two honeycombs. It can be seen that for these two honeycombs with different cell-size but the same cell-wall thickness, the strength enhancement $\Delta\overline{p}$ of small cell-size honeycomb (0.72MPa) is only slightly higher than the one of large cell-size honeycomb (0.58MPa), and the significant difference of $\gamma_{plateau}$ for two honeycombs is mainly due to the change of honeycomb strength.

In the simulations of Chapter 2, the influence of cell-size on the dynamic enhancement of honeycombs has also been studied on two honeycomb cell-models with different cell-size. The deformation mode of small cell-size model under quasi-static loading varies at large deformation period, which makes the calculated dynamic enhancement rate probably contain significant errors. However, similar trend to the experimental results is found for the calculating results at early deformation period (e.g. before the second fold formation), where the two models with different cell-size are of the same deformation mode at quasi-static loading condition.
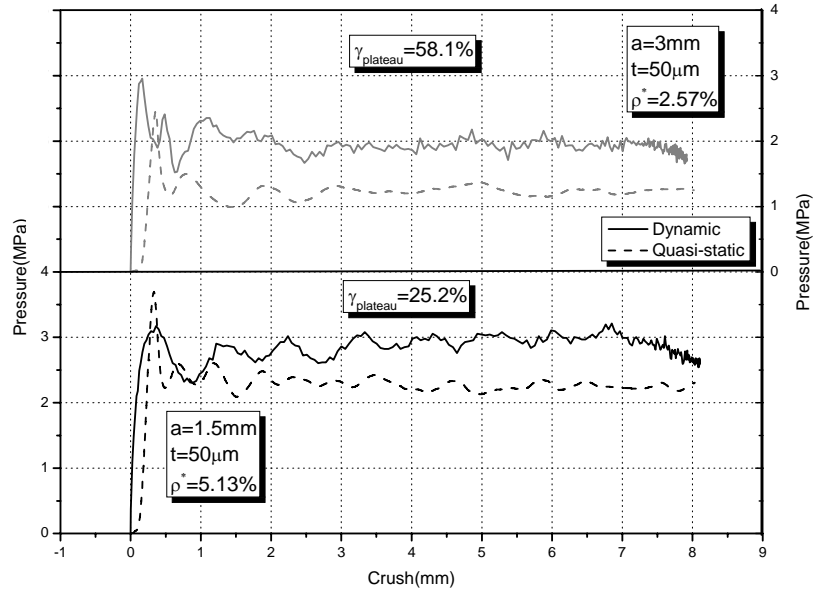
Figure 3.14 Dynamic strength enhancement of honeycombs with different cell-size

3.4.4 Influence of cell-wall thickness

The comparison between Case 2 and Case 3 in Table 3.2 (with a=2mm, t=40μm and a=2mm, t=60μm) shows that the cell-wall thickness has influence on honeycomb strength and also the dynamic enhancement rate $\gamma_{plateau}$. The cell-wall thickness affects honeycomb strength more remarkably than the cell-size. For example, when the cell-wall thickness increases from 40μm to 60μm by 50% (the relative density will also increase by 50%), the honeycomb strengths under quasi-static loading and dynamic loading increase respectively by 233% and 215%. While from the viewpoint of dynamic enhancement rate, the values of $\gamma_{plateau}$ for these two honeycombs with different cell-wall thickness are close to each other (37.8% for Case 2 with t=60μm and 45.8% for Case 3 with t=40μm).

The pressure/crush curves for honeycombs with different cell-wall thickness under both quasi-static and dynamic loadings are shown in Figure 3.15. A much bigger gap between quasi-static and dynamic curves is found for the thick cell-wall honeycomb, i.e. the strength enhancement $\Delta\bar{p}$ for honeycomb of t=60μm is much bigger than the one for honeycomb of t=40μm. However, considering the higher strength of thick cell-wall honeycomb, the dynamic enhancement rate as illustrated before shows no significant difference for these two cases. This result is also in consistent with the calculating one in Chapter2.
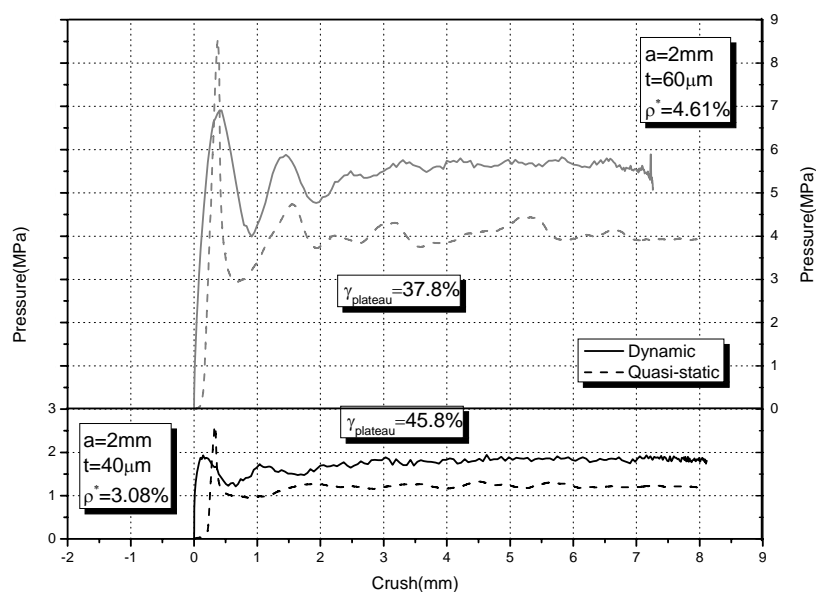
Figure 3.15 Dynamic strength enhancement of honeycombs with different cell-wall thickness

3.4.5 Influence of base material

Besides the above-mentioned cell-size and cell-wall thickness, the base material also has influence on the dynamic enhancement of honeycombs. In this study, we performed the uniaxial compressive experiments on two kinds of honeycombs made of 5052 aluminium alloy and 3003 aluminium alloy. Case 2 (with $\rho^* = 3.08\%$) and Case 6 (with $\rho^* = 3.19\%$) in Table 3.2 are with nearly the same relative density and are compared in Figure 3.16 to indicate the effects of base material on the dynamic enhancement of honeycomb strength.

In Figure 3.16, it can be seen that the strength of 5052 honeycomb is much higher than the one of 3003 honeycomb due to the stronger base material. Thus, although the dynamic strength enhancement of 5052 honeycomb (0.79MPa) is slightly higher than the one of 3003 honeycomb (0.55MPa), the dynamic enhancement rate of 5052 honeycomb (25.4％) is much lower than the one of 3003 honeycomb (45.8％).
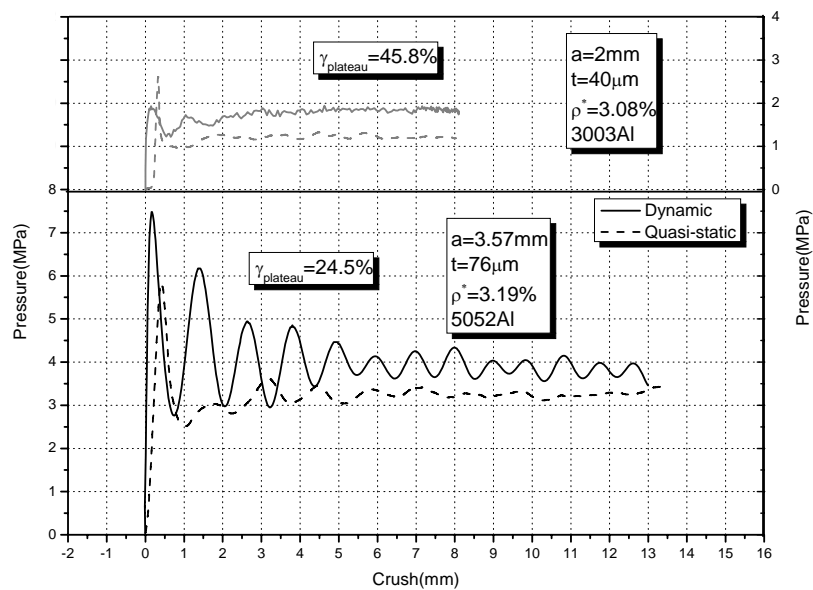
Figure 3.16 Dynamic strength enhancement of honeycombs made of different base materials

Honeycombs made of different base materials show different dynamic enhancement, which means that the stress/strain behavior of base material plays an important role in enhancing honeycomb strength under dynamic loading. In fact, we have demonstrated in Chapter 2 of this thesis the adaptability of an inertia effect model in explaining this dynamic enhancement of honeycombs. According to this mechanism, the collapse deformation of honeycomb under dynamic loading is delayed by the lateral inertia effect, and further axial deformation can be expected, which makes the axial plastic strain of honeycomb model just before collapse higher under dynamic loading than under quasi-static loading. Further more, if the base material is strain hardening, the stress as well as the loading capacity of the honeycomb model is also enhanced in dynamic loading. Thus, the strain hardening behavior of base material is considered as a key factor in enhancing honeycomb strength under dynamic loading.

It worth emphasizing that the present experimental work indicates fundamentally the influence of base material on the dynamic enhancement of honeycomb strength, however, because of the limitations of time and experimental conditions, the existing work is inadequate to make this problem clear, and further investigations are going to be performed in future works:

Firstly, the present specimens in this work are of different cell-size and cell-wall thickness, and it is necessary to find honeycombs made of different base material, but

with same geometric parameters to investigate individually the influence of base material on the dynamic enhancement of honeycombs.

Secondly, the knowledge of the specific stress/strain curves of the honeycomb base materials such as 5052 aluminium alloy and 3003 aluminium alloy is of great importance to indicate in detail this influence. However, the only found references on these aluminium alloys are from bulk material experiments, the properties of which is far away from the foils employed in honeycombs after particular material heat treatment and hardening process. Thus, we are going to perform additionally some tension experiments on small foil specimens from honeycomb cell-wall to obtain the exact stress/strain curves of base materials.

Thirdly, with the exact stress/strain curves of 5052 aluminium alloy and 3003 aluminium alloy, the numerical models in Chapter 2 can be improved, which enables the comparison between the simulation results and the experimental ones. For present, the calculated dynamic enhancement rate (mostly below 20%) is much lower than the one observed in experiment (with the maximal 58.1%), which may be due to the different base materials.

3.5 Summary

This chapter aims to study the phenomenon of dynamic enhancement of honeycombs under moderate impact velocity experimentally. A series of experiments were performed on honeycombs with different geometric parameters and made of different materials under out-of-plane uniaxial compression both dynamically and quasi-statically. The influences of geometric parameters (including cell-size and cell-wall thickness) and the strain hardening behavior of base material on the strength enhancement of honeycombs under dynamic loading were investigated.

In Section 3.1, the set-up of classical Hopkinson bars was firstly presented. Then, some specific problems associated with cellular materials in Hopkinson experiments were analyzed, which included the large data scatter produced by inhomogeneous microstructure of cellular materials, the mismatch of wave impedance between the bars and the specimen and the challenge arised from the non-uniform deformation of cellular materials to the data processing method of classical Hopkinson experiments. Finally, a large diameter viscoelastic Split Hopkinson Pressure Bar system suitable for cellular materials was presented. The associated problems like wave dispersion correction as well as the definition of mean pressure and crush are proposed to

describe the deformation behavior of cellular materials. Section 3.2 introduced briefly the quasi-static experimental method.

Basing on the proposed experimental methods, the out-of-plane behaviors of six types of honeycombs with different cell-size and cell-wall thickness and made of different base materials were investigated in Section 3.3 and 3.4. The experimental results show good reproducibility for both dynamic and quasi-static loading cases. A significant enhancement of honeycomb strength at Stage II is observed for all the tested specimens.

For the honeycombs made of the same base material and with the same cell-wall thickness, the change of cell-size affects the dynamic strength enhancement insignificantly. The fact that the dynamic enhancement rate of large cell honeycomb is much higher than the one of small cell is mainly due to the decrease of honeycomb strength by enlarging the cell-size.

While for the honeycombs with different cell-wall thickness, thick wall honeycomb has much bigger strength enhancement $\Delta \bar{p}$ than the one of thin wall honeycomb. However, considering the higher strength of thick cell-wall honeycomb, the dynamic enhancement rate as illustrated before shows no big difference for these two cases.

Beside, the base material has also significant influence on the dynamic enhancement of honeycombs.

References

[1]   B. Hopkinson. A method of measuring the pressure in the deformation of high explosives by the impact of bullets. Phil.Trans. Roy. Soc. A213, 437-452 (1914).

[2]   R. M. Davies, A critical study of Hopkinson pressure bar. Phil. Trans, Roy. Soc. A240, 375-457 (1948).

[3]   H. Kolsky. An investigation of the mechanical properties of materials at very high rates of loading. Proc. Phys. Soc. B62, 676-700 (1949).

[4]   J. Harding, E. O. Wood, J. D. Campell. J. Mech. Engng. Sci. 2, 88-96 (1960).

[5]   U. S. Lindholm, L. M. Yeakley, Exp. Mech. 8, 1-9, (1968).

[6]   J. Duffy, J. D. Cambellm, R. H. Hawley, On the use of a Torsional Split Hopkinson Bar the study rate effects in 11000 Aluminum. J. Appl. Mech. 38, 83-91 (1971).

[7]   W. E. Baker, C. H. Yew. J. Appl. Mech. 33, 917, (1966).

[8]   S. Nemat-Nasser, J. B. Isaacs, J. E. Starrett. Hopkinson techniques for dynamic recovery experiments. Proc. R. Soc.Lond. A 435, 371-391 (1991).

[9]   A. M. Lennon, K. T. Ramesh. A technique for measuring the dynamic behavior of materials

at high temperatures. Int. J. Plasticity. 14 1279-1292 (1998).

[10]   H. Zhao, G. Gary, J. R. Klepaczko. On the use of a viscoelastic split Hopkinson pressure bar. Int. J. Impact Engng. 19, 319-330 (1997).

[11]   H. Zhao, G. Gary, crushing behavior of aluminium honeycombs under impact loading. Int. J. Impact Engng. 21, 827-836 (1998).

[12]   C. Chree, The equation of an isotropic elastic solid in polar and cylindrical co-ords their solutions and applications. Cambridge Phil. Soc. Trans, 14, 250-369 (1889).

[13]   P. S. Follansbee, C. Franz, Wave propagation in the split Hopkinson pressure bar. J. Engng Mater. Tech. 105, 61-66 (1983).

[14]   D. A. Gorham, A numerical method for the correction of dispersion in pressure bar signals. J. Phys. E: Sci. Instrum. 16, 477-479 (1983).

[15]   J. C. Gong, L. E. Malvern, D. A. Jenkins, Dispersion investigation in the split Hopkinson pressure bar. Engng Mater. Tech. 112, 309-314 (1990).

[16]   G. Gary, J. R. Klepaczko and H. Zhao, Correction de dispersion pour l'analyse des petites deformations aux barre de Hopkinson, J. Physique III 1, c3-403 (1991).

[17]   R. D. Mindlin, H. D. McNiven, Axially symmetric waves in elastic rods. J. Appl. Mech. 27, 145-151 (1960).

[18]   G. A. Coquin, Attenuation of guided waves in isotropic viscoelastic materials. J. Ac. Soc. Am. 36 (6), 1074-1080 (1964).

[19]   H. Zhao, G. Gary. A three dimensional analytical solution of the longitudinal wave propagation in an infinite linear viscoelastic cylindrical bar. Application to experimental techniques. J. Mech. Phys. Solids, 43, 1335-1348 (1995).

[20]   D. R. Bland. The theory of linear viscoelasticity. Oxford University Press, Oxford (1960).

[21]   J. D. Achenbach. Wave Propagation in Elastic Solids. North-Holland Publ. Co.

[22]   K. F. Graff. Wave Motion in Elastic Solid. Ohio State University Press.

[23]   H. Zhao, G. Gary. Crushing behaviour of aluminium honeycombs under impact loading. Int. J. Impact Eng. 21, 827-836 (1998).

Part Ⅱ Multi-axial behavior of honeycombs under combined shear-compression

Chapter 4 Combined dynamic shear-compression loading technique by SHPB

4.1 Combined shear-compression loading technique

4.1.1 Combined shear-compression set-up

In order to achieve dynamic multi-axial loading on the basis of SHPB, a combined shear-compression loading device which is composed of two short cylindrical bars with one bevel end, a Teflon sleeve and two aluminium supports is proposed. The short beveled bars are placed at the interfaces of the specimen and the input and output bars as shown schematically in Figure 4.1. The two inserted short beveled bars are made of the same material and have the same diameter to the Hopkinson bars. This insures that the incident wave propagates from the input bar to the input beveled bar without significant reflections, and the transmitted wave can also travel from the output beveled bar to the output bar completely. The honeycomb specimen is placed between the two parallel bevels instead of contacting with the input and output bars directly and perpendicularly in a classical SHPB. A column sleeve made of Teflon and two aluminium supports are used to fix the whole device. Figure 4.2 shows the photograph of our combined dynamic shear-compression device.
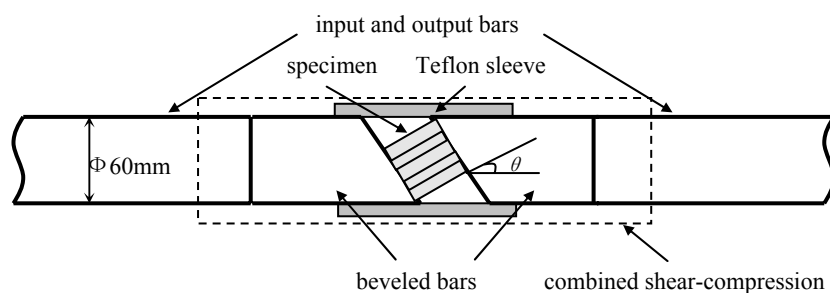
Figure 4.1 Scheme of the dynamic biaxial loading device
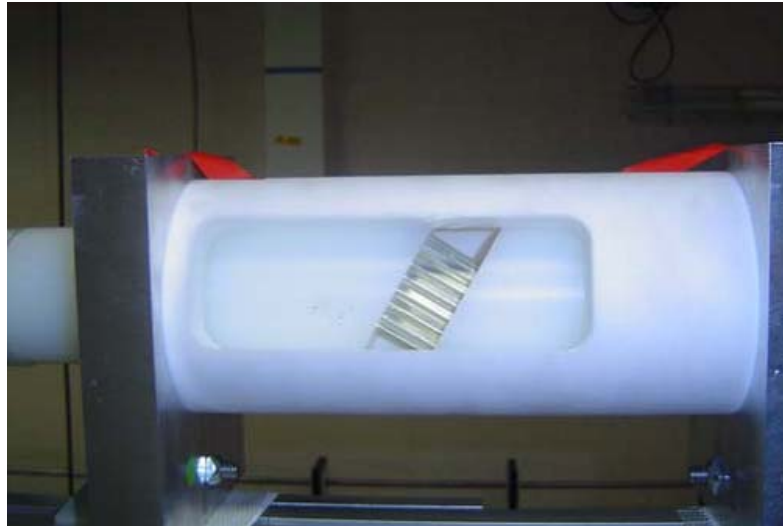
Figure 4.2 Photograph of the dynamic biaxial loading device

In the experiments, when the projectile impacts the input bar at certain velocity, a compressive incident wave $\varepsilon_i(t)$ will be developed in the input bar and propagates towards the specimen. Once this wave reaches the input bar/input bevel bar interface, it will get through the interface and propagate in the input bevel bar without any reflection because of the complete match of wave impedance between these two bars. When this incident wave reaches the input bevel bar/specimen interface, part of it is reflected (denoted as $\varepsilon_r(t)$), whereas the other part goes through the specimen and develops the transmitted wave $\varepsilon_t(t)$ in the output bevel bar and then output bar. It is worth emphasizing that the friction coefficient between the specimen and the beveled bars should be large enough to make sure that no slippage occurs during the loading period. In this way, during the process of stress wave traveling through the specimen, the specimen is loaded by the horizontal movement of input and output bevels and a combined shear-compressive loading state is achieved. For the sake of illustration convenience, loading angle θ is defined as the angle between the axes of honeycomb cells and the loading direction (as shown in Figure 4.1). Clearly, the larger the loading angle is, the more dominant the shear component becomes. With $\theta=0^o$, a pure compressive experiment is obtained.

The same measuring method with classical Hopkinson system is adopted. Two strain gauges are cemented at the midpoints of input and output bars to record the three basic waves $\varepsilon_i(t)$, $\varepsilon_r(t)$ and $\varepsilon_t(t)$ (as shown in Figure 4.3) which can be used to calculate the forces and deformation velocities of honeycombs. Then, the overall behavior of honeycombs under combined dynamic shear-compression is obtained.
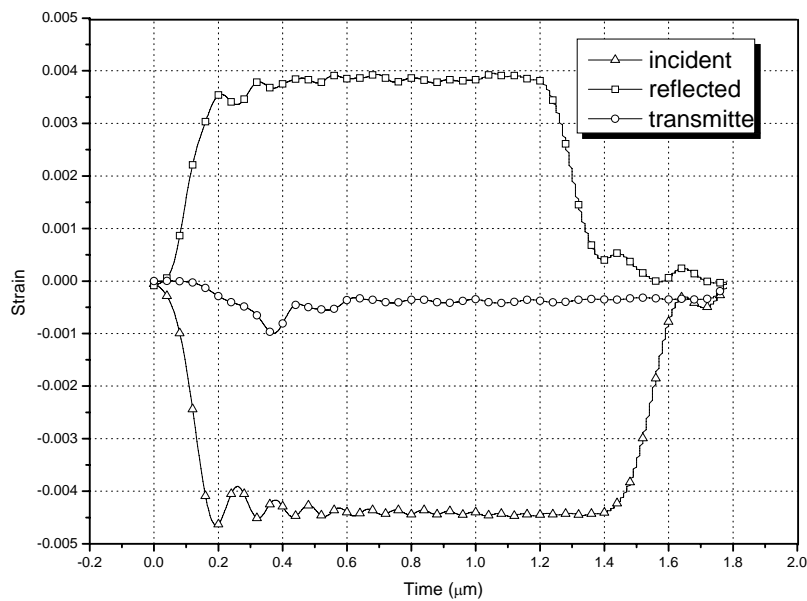
Figure 4.3 Three basic waves measured from the experiments with biaxial loading device

4.1.2 Effects of beveled bars on data process method

It has been illustrated that Hopkinson bars in fact provide both the forces on specimen faces and the deformation information (Equation 3.25 and 3.26). The feasibility of data measuring and processing method basing on one-dimensional elastic wave theory have been validated in classical SHPB as well as in large diameter viscoelastic bars, but will be challenged by the introduction of two beveled bars in the combined shear-compression SHPB system.

Firstly, the friction between the Teflon sleeve and the beveled bars is not eliminable, which will introduce difference between the forces on specimen and the forces obtained by strain gauges. The estimation of possible errors on force measurement should be performed.

Secondly, the inserted short beveled bars are not rigid and will undergo deformation during the testing. The possible errors induced by the deformation of beveled bars to the displacement measurement of specimens should also be checked.

Thus, a validating work should be carried out on this combined shear-compression SHPB system before using it to investigate the multi-axial behavior of cellular materials. In fact, the data measuring and processing method of classical SHPB can be applied directly to the combined shear-compression SHPB with following assumption:

Assumption 1: The friction between the Teflon sleeve and the beveled bars are small enough to be neglected and the specimen force can be transferred to the Hopkinson bars and deduced by the recorded strain signals.

Assumption 2: The deformation of beveled bars is elastic and small enough to be neglected, which means that the two bevels contacting with specimen keep parallel to each other during the loading process and the accuracy of deformation measured by strain gauges is ensured.

It is worth noting that the output force may contain more experimental errors such as the friction between the Teflon sleeve and the beveled bars, an imperfect contact between bar/specimen and a bad alignment etc. Thus, here for the combined shear-compression experiments, the input force is believed to be more accurate and is employed for calculating the pressure of tested honeycombs. The simulation work in Chapter 6 shows also that the input force can be easily reproduced while the output force is difficult to simulate in an idealized testing condition. The pressure and crush of honeycombs under combined shear-compression can be calculated as follows:

$$p(t) = F_{input}(t) / S_s \qquad\qquad 4.1$$

$$\Delta(t) = \int_0^t (V_{output}(\tau) - V_{input}(\tau)) d\tau \qquad\qquad 4.2$$

4.2 Validation of the combined shear-compression method by FEM

4.2.1 FEM model installation

In order to verify those two assumptions suggested in Section 4.1 and to evaluate the potential errors, a numerical analysis of the whole loading system is performed. Such a virtual numerical test allows for the comparison between the forces and the velocities derived from the strain history at the measuring points in the pressure bars and those located at the interfaces between beveled bar ends and specimen faces.

The virtual experiment using FEM is performed via ABAQUS/Explicit in order to clarify these uncertainties. We established an entire model using the actual size of experimental apparatus, composed of the projectile, the input and output bars, the inserted beveled bars, the Teflon sleeve and the specimen, to simulate the whole loading process. The computation for loading angle $\theta = 30^o$ is taken for instance.

The geometrical model was discretized by 8-node linear brick elements with reduced integration and hourglass control (C3D8R). An element size of 0.5 mm was chosen for the bars and the Teflon sleeve, while for the bevels and specimen, smaller elements with sizes of 0.3 mm and 0.15 mm were used respectively. A convergence study on element size shows that the used elements are small enough for obtaining reliable results within reasonable calculation expense. With the used element sizes, the model has 164316 elements in total. A part of the meshed FEM model around the biaxial loading device area is shown in Figure 4.4
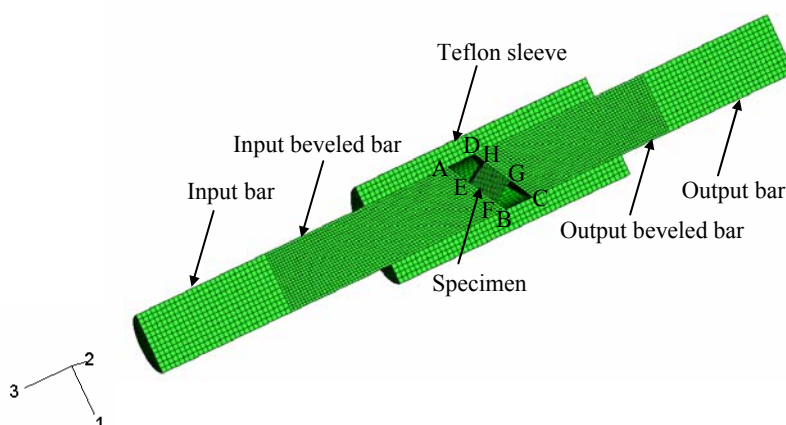
Figure 4.4 Finite element model of SHPB with biaxial loading device (part show and view cut by X_1X_3 plane)

A crushable foam model available in this code (see Section 18.3.5, Abaqus Analysis User's Manual) is chosen to describe the constitutive behavior of the specimen. The parameters are identified with the experimental data of the studied honeycomb under quasi-static out-of-plane uniaxial compression (the pressure/crush curve is shown in Figure 4.5). In fact, as the specimen takes only a small part in the whole model, its elastic behavior (Young's Modulus, Poisson Ratio) is not very important in the calculation. Under plastic regime, the Poisson's ratio is set to zero and lock strain is determined rather roughly. The only dominant parameter σ_s is defined as the average level of plateau stress of the curve shown in Figure 4.5. For the other parts of the model, linear material with elastic constants of Nylon and Teflon is used for bars and sleeve respectively. All the material parameters are listed in Table 4.1.

Surface-to-surface contact with penalty contact method is employed for all the contacts. At the interfaces between the specimen and the beveled bars, a no sliding condition is applied. The interfaces between the Nylon bars and the bevels are given

frictionless contact property. The friction force between the Teflon sleeve and the Nylon bevels is estimated with the penalty friction formulation and the friction coefficient is set to be 0.05.
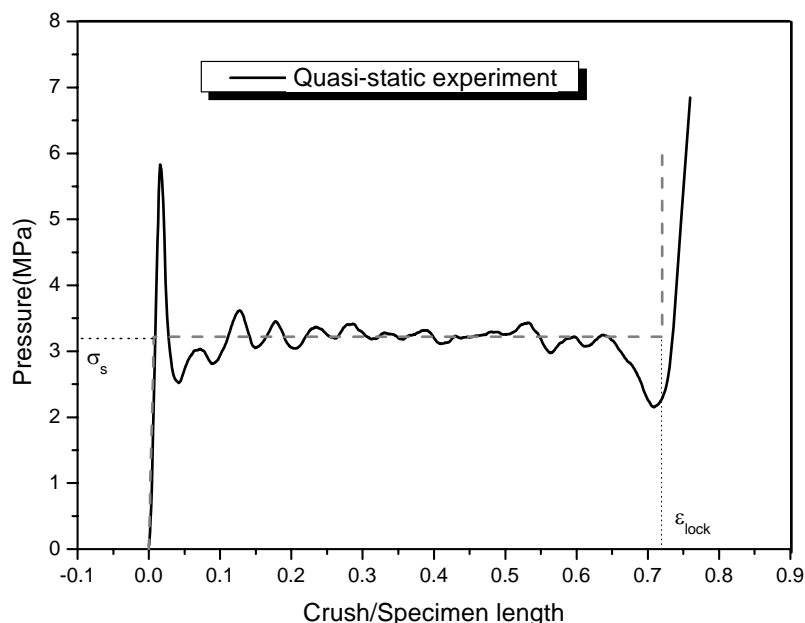
Figure 4.5 Pressure/crush curve of honeycomb under quasi-static pure compression

Table 4.1 List of the material parameters used in the simulations

	Density ρ (kg/m³)	Young's Modulus E (MPa)	Poission's Ratio v	Plastic Possion's Ratio v_p	Yield Stress σ_s (MPa)	Lock Strain ε_{lock}
Honeycomb	82.6	450	0.35	0	3.22	0.72
Nylon	1120	3370	0.3	-		
Teflon	2200	1500[1]	0.46[1]	-		

The projectile has an initial velocity of 15m/s in axial (X_3) direction which is the real impact velocity measured in our experiment. The external surface of the Teflon sleeve is restricted on three translational displacements. For the Hopkinson bars, lateral displacements (in the X_1 and X_2 directions) are restricted on their external surface at four sections corresponding to the positions of the supports.

4.2.2 Comparison between three basic waves

Figure 4.6 shows the comparison between the calculated strain signals and the experimental ones. The incident and reflected waves from experiments and

simulations are rather in good agreement. The large oscillations in the simulated incident and reflected waves are, for a large amount, due to elastic bars assumption in simulation. In the real test, the oscillation is smaller because of the viscoelastic feather of the bars which tend to generate less oscillating incident wave. However, such oscillations do not affect the main feature (movement and stress) of the beveled ends. For the transmitted wave, there are some differences, especially for the peak value, which may imply some imperfect contact or alignment in the real test.
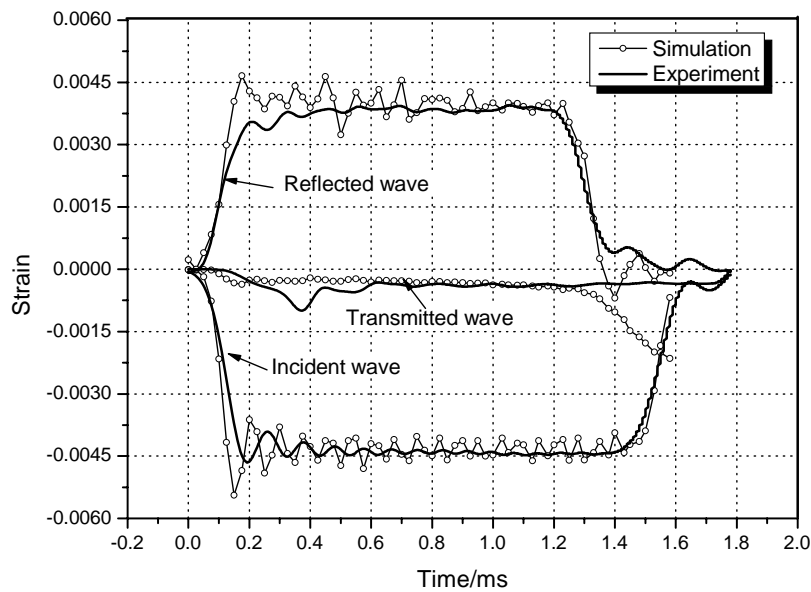
Figure 4.6 Comparison of basic waves between simulation and experiment

4.2.3 Estimation of friction between beveled bars and Teflon sleeve

In order to validate the accuracy of the force measurement and to estimate the influence of friction between the beveled bars and the Teflon sleeve, the following quantities are extracted from simulation data. The force derived from the bar F_{bar} is obtained from the strain on the input bar using the data processing method of SHPB (Eqation 3.25). The force at the bar/specimen interface $F_{specimen}$ is the X_3 component of total force due to the contact pressure and the frictional stress between the specimen and the input bevel which can be picked up directly in simulations. The friction force $F_{friction}$ is the X_3 component of the total force due to friction between the input bevel and the Teflon sleeve.

Figure 4.7 shows the comparison between these three quantities, indicating that $F_{friction}$ is a small value comparing with F_{bar} and $F_{specimen}$ and can be neglected without leading to significant error on them.
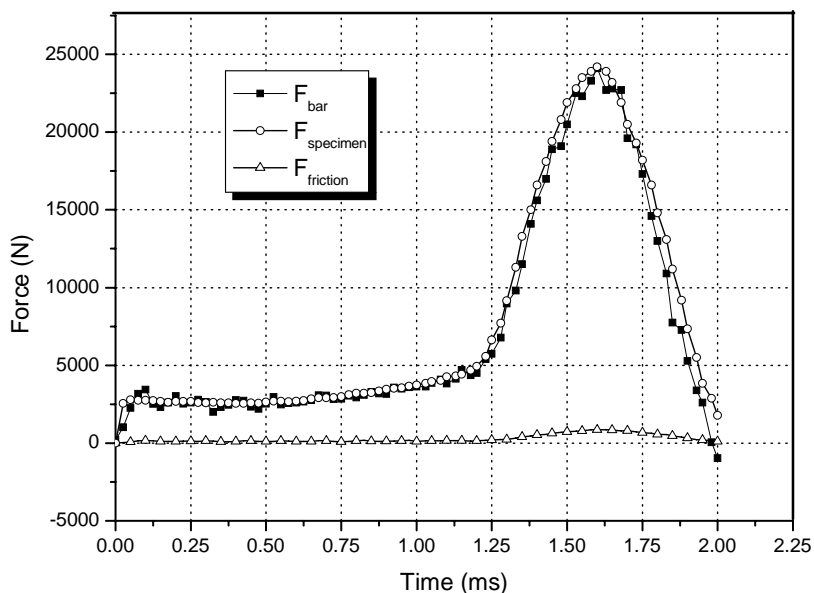
Figure 4.7 Comparison between the input bar force, the specimen force and the frictional force

4.2.4 Estimation of the beveled bar deformation

In order to verify the assumption of identical axial displacements of the beveled ends, we depict the axial displacements for the positions located at longer major axe of ellipse of bevels at the instant when the specimen strain is maximal. In Figure 4.8, the positions *A*, *B*, *C* and *D* correspond to the four free end nodes and *E*, *F*, *G*, *H* are the four edge contact points between specimen and bevels (Figure 4.4). It is found that the two bevels of each beveled bars are not in parallel any more but with certain elastic deformation. This elastic deformation is included in the deformation measurement from strain gauges and will act as an error in this combined shear-compression experiments. It is indicated in Figure 4.8 that this displacement difference of 0.17 mm between the contact region of specimen and free end nodes of bevels will approximately result in an error of 1.31 %.
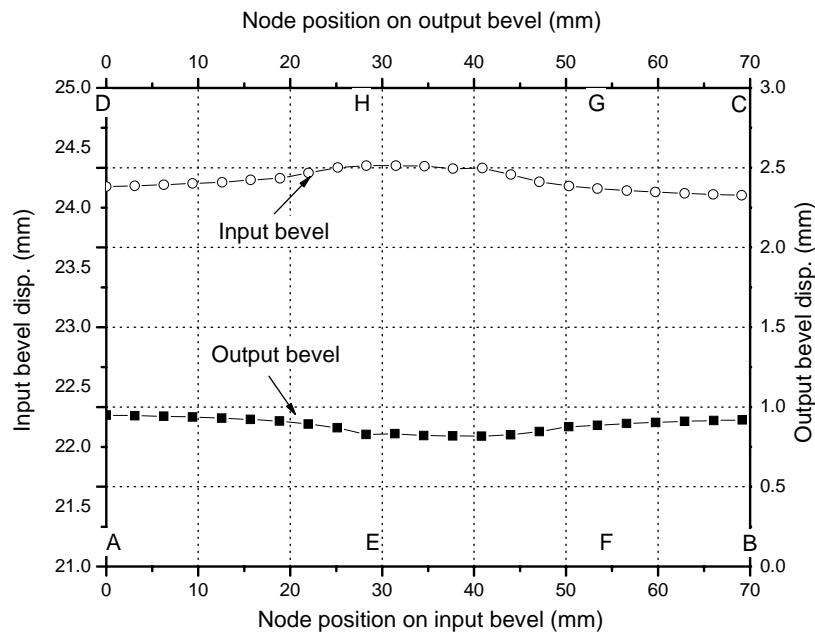
Figure 4.8 Displacement distribution on input and output bevels along major axes

4.3 Quais-static combined shear-compressive experiments

The quasi-static experiments under combined shear-compression were also performed in order to make a dynamic/quasi-static comparison. A universal Tension/Compression INSTRON3369 machine with the same combined shear-compression device is employed (as shown in Figure 4.9).
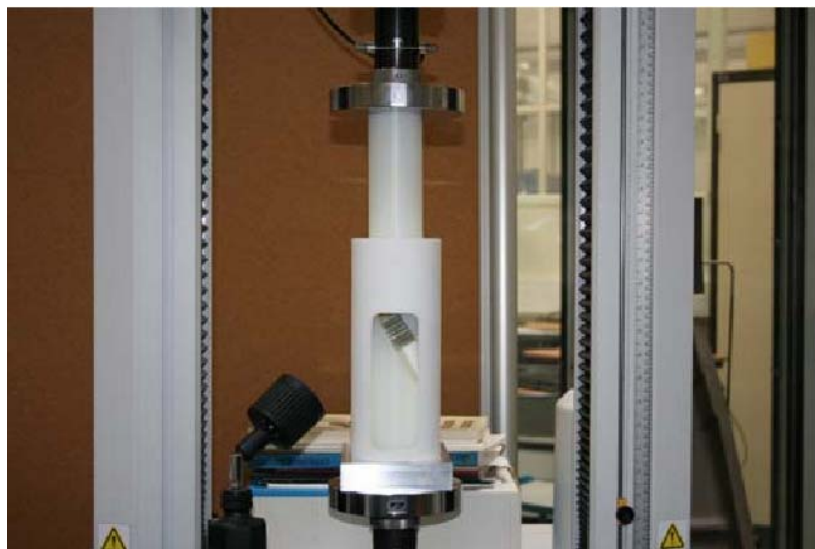
Figure 4.9 Photograph of quasi-static loading set-up with INSTRON machine

Similar to the dynamic combined shear-compression loading method, it should be assured that no slippage occurs between the beveled bars and the specimen. Then, the recorded displacement and force information by the displacement and load cells on the machined can give the quasi-static biaxial behavior of honeycombs under combined shear-compressive loading.

4.4 Summary

This chapter presented a new combined shear-compression loading method by introducing two short beveled bars into a large-diameter Nylon SHPB set-up and a uniaxial INSTRON machine to investigate the combined shear-compression behavior of honeycomb under dynamic and quasi-static loadings.

The influence of the introduced beveled bars on the measurements of forces and velocities in this combined shear-compression SHPB system was analyzed and the data processing method was determined.

Finally, the verification of such a design by means of FEM analyses revealed that the force and velocity components in the axial direction of the pressure bar for foam-like specimen under combined shear-compression could be well measured from Hopkinson bar and the possible errors induced by the bevels were also estimated.

References

[1]. P. J. Rae, D. M. Dattelbaum. The properties of poly (tetrafluoroethylene) (PTFE) in compression. Polymer, 45, 7615-7625 (2004).

Chapter 5 Experimental results of honeycombs under combined shear-compression

5.1 Material and specimen

In this study, the honeycomb specimens chosen for our combined shear-compression experiments are of 5052 honeycomb which has been presented in Chapter 3 for uniaixal compressive experiments. This hexagonal honeycomb possesses a relative density of $\rho^* = 3\%$ with single wall thickness t=76μm, the expansion angle α=30°, and a minimum cell diameter S=6.35mm (as shown schematically in Figure 5.1(a)). It has three orthotropic directions denoted as T L and W, where T-direction, also known as the out-of-plane direction corresponds to the axes of the honeycomb cells and is the strongest direction. The other two directions (L and W) are so-called in-plane directions referred as the ribbon direction and the width direction of honeycomb (Figure 5.1(b)).

Cubic specimens are used in dynamic and quasi-static experiments with dimension of 25×40×40 mm in the directions of T L and W respectively which means there are 39 complete cells in the cross section of the honeycomb specimen. There is then more than 6 cells in any direction so that the size effect is normally not important.
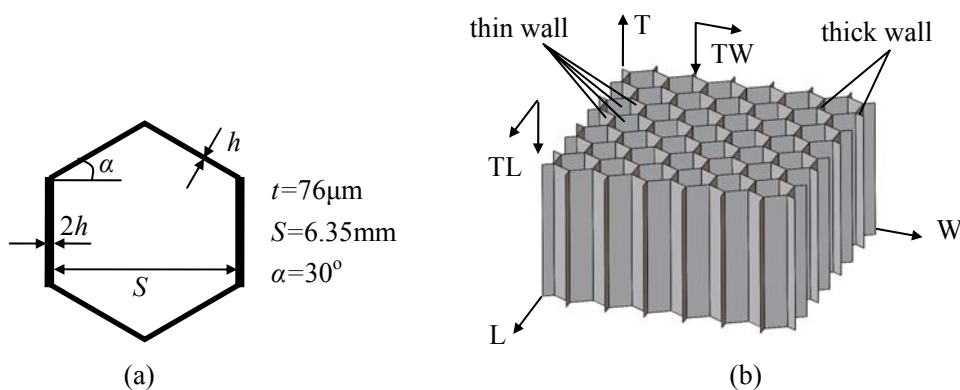
Figure 5.1 The geometry of unit cell (a) and the constructed honeycomb specimen (b)

5.2 Experimental results of honeycombs

By using the combined shear-compressive loading method presented in Chapter 4, a series of experiments on honeycombs at seven different loading angles and in two loading planes was performed both quasi-statically and dynamically. The seven loading angles ranges from $\theta=0^o$ (corresponding to a pure compressive loading) to $\theta=60^o$ (loading state with shear component the most dominant) with every ten degree. The two loading planes of out-of-plane shear-compression are respectively the TW and TL planes in honeycomb structures. A high-speed camera was used in both quasi-static and dynamic experiments to capture the deformation configuration during the loading process.

5.2.1 Reproducibility

This improved SHPB enables the combined dynamic shear-compressive loading on cellular materials, however, the large modifications on classical SHPB increase the complexity of experiments and the reliability. Thus, the repeatability of the data measurement should be checked in the first instance.

In order to illustrate the reproducibility of the tests, three repeating experiments are conducted for each loading case. Figure 5.2 displays the dynamic pressure/crush curves for $\theta=40^o$ in TW loading plane. Despite of the fluctuations of these curves which are probably due to wave dispersion, the three curves show only a small dispersion for both the initial peak value and the average strength in plateau region, indicating that the experimental results are reliable. The reproducibility of quasi-static experimental results are also confirmed as shown in Figure 5.3 the pressure/crush curves of $\theta=60^o$ in TL loading plane.

Nevertheless, for a minority of the specimens, a large scatter of the pressure/crush curves under same loading conditions can also be found. Figure 5.4 presents the three repeating experimental results for $\theta=50^o$ in TW loading plane, in which two curves are in good agreement to each other, while the third one is much higher. It is explained in Section 5.4 that this diversity of honeycomb behavior under the same combined shear-compression is related to the different deformation modes. This bifurcation of honeycomb deformation mode is in fact a nature property of this thin-wall structure with unstable buckling in out-of-plane crush and is irrelevant to our combined shear-compression technique.
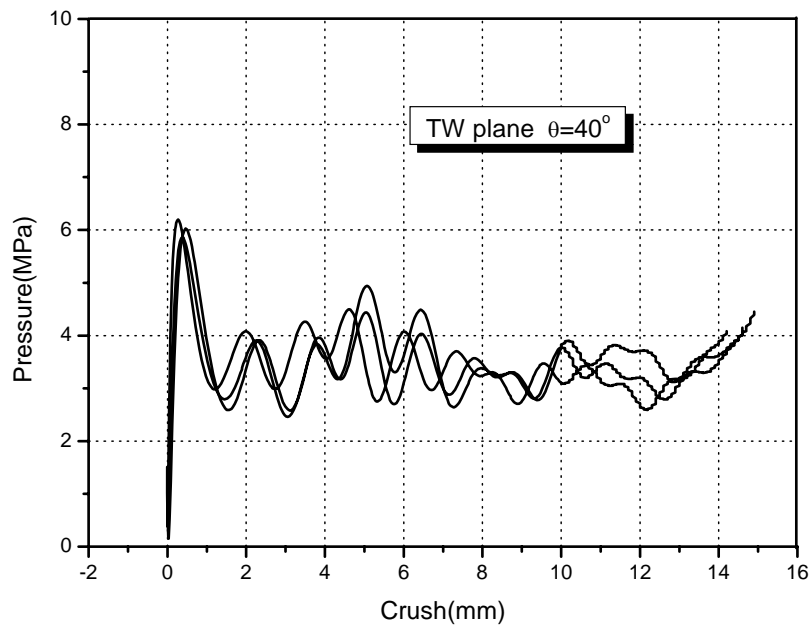
Figure 5.2 Reproducibility of impact experiment on honeycomb under dynamic combined shear-compression (TW plane, θ=40$^{\text{o}}$）
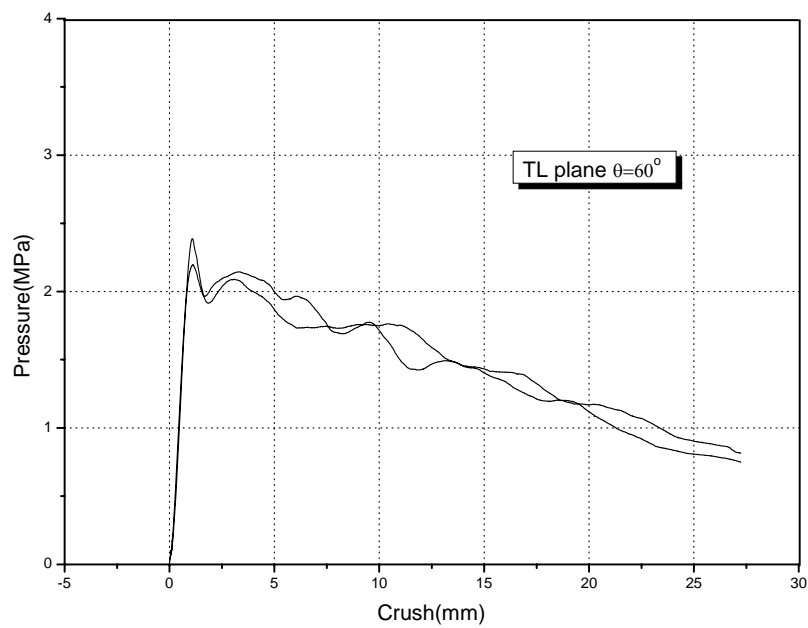
Figure 5.3 Reproducibility of impact experiment on honeycomb under quasi-static combined shear-compression (TW plane, θ=40$^{\text{o}}$）
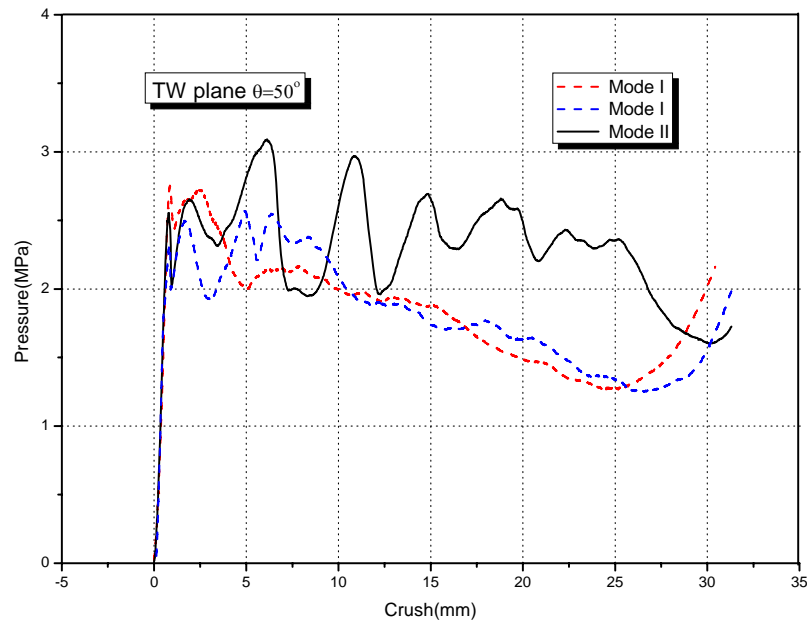
Figure 5.4 Bifurcation of honeycomb behavior under the same combined shear-compression loading (Quasi-static, TW plane, $\theta=0^{o}$).

5.2.2 Dynamic experimental results under combined shear-compression

5.2.2.1 TW loading plane

The pressure/crush curve of honeycomb under combined shear-compression at $\theta=30^{o}$ in TW plane is shown in Figure 5.5. It is well known that a typical out-of-plane pressure/crush curve of honeycomb under uniaxial compression consists of an initial peak denoting the first plastic collapse of the microstructure, a long stress plateau related to the successive folding process and a densification stage. It has been observed in combined quasi-static shear-compression experiments all of these three deformation stages of honeycomb. But here for the dynamic one in Figure 5.5, the first two stages can be well identified from the curves of our experiments, while the densification stage is absent due to the limitation of loading duration of SHPB. It should be noted that, in this study, all the curves are cut at $\delta = 13mm$ for both dynamic and quasi-static results in order to facilitate the comparison.

The influence of loading angle θ on the biaxial behaviors of honeycomb under combined shear-compression is investigated by presenting the pressure/crush curves of five loading angles together in Figure 5.6 (the curves of $\theta=10^{o}$ and $\theta=20^{o}$ are very close to the ones of $\theta=0^{o}$ and $\theta=30^{o}$ and are not included for display clarity). Some

interesting findings are as follows: Firstly, the slope of the ascending segment to reach the initial peak varies with loading angle θ as shown in the enlarged subfigure in Figure 5.6. Secondly, the initial peak value decreases with increasing θ, which indicates easier initial collapse of honeycomb at larger loading angle. Thirdly, the average level of the plateau stress becomes lower as the loading angle θ increases and the capacity of honeycomb is in fact weaker at more dominant shear loading.
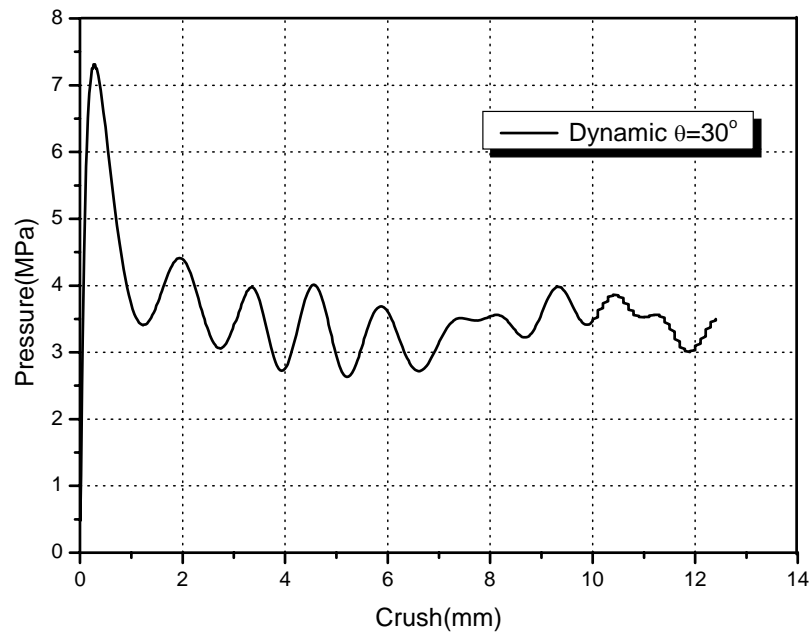
Figure 5.5 Dynamic Pressure/crush curve of honeycomb (TW plane, $\theta=30^{o}$)
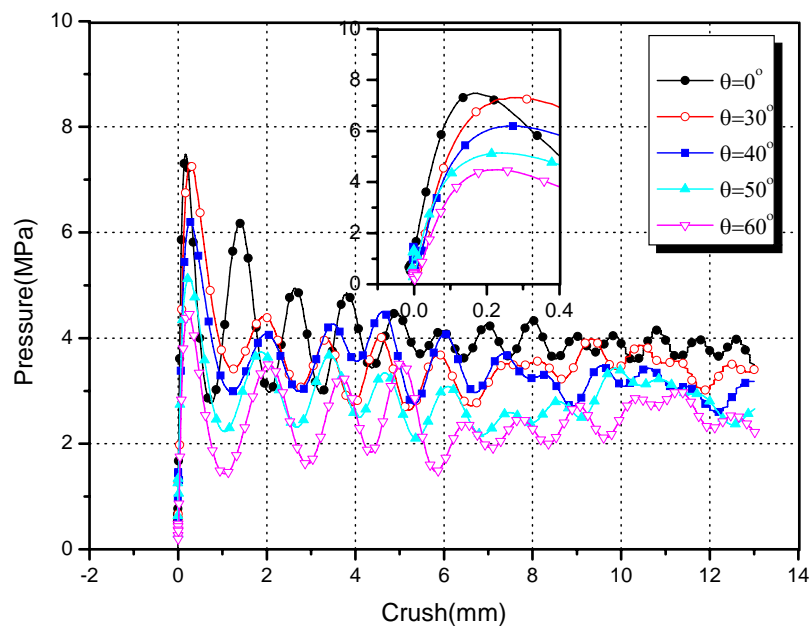
Figure 5.6 Dynamic pressure/crush curves of honeycombs in TW plane at different loading angles

In order to study quantitatively the influence of loading angle θ on the overall biaxial behavior of honeycombs, two loading stages as defined in Chapter 2 are also employed for the analysis of combined shear-compression experimental results. Stage I is under elastic deformation from zero crush to the position of initial peak. In this stage, the initial peak values are concerned. Stage II covers the rest part of the pressure/crush curves after the initial peak and ends at 13mm crush. Consequently, we calculated the average strength of stage II by dividing the curve area of this plateau deforming period (absorbed energy) by corresponding crush length, which gives:

$$\bar{p} = \frac{1}{\delta_{max} - \delta^*} \int_{\delta^*}^{\delta_{max}} p\, d\delta \qquad\qquad 5.1$$

where δ^* denotes the crush value at the point of the initial peak for each of the overall pressure/crush curve. δ_{max} is the maximum crush of the corresponding crushing duration, which in this study is taken as 13mm.

Table 5.1 Summary of dynamic behavior of honeycombs under TW plane combined shear-compression

Loading angle θ	0°	10°	20°	30°	40°	50°	60°
Peak value of Stage I (MPa)	7.48	7.38	7.35	7.31	6.20	5.14	4.49
Average strength of Stage II (MPa)	4.01	3.88	3.71	3.56	3.43	2.86	2.45

The distribution of initial peak values and average plateau strengths of honeycombs under TW plane shear-compression are displayed in Figure 5.7. It can be seen that these two quantities are all in a descending trend with the loading angle.

5.2.2.2 TL loading plane

The combined shear-compression experiments on honeycombs are performed in both TW plane and TL plane. Figure 5.8 presents the pressure/crush curves of honeycombs at $\theta = 30^o$ and in both TW and TL loading planes and no obvious difference is found for either the elastic region or the plateau crushing stage. However, due to the anisotropic characteristic of honeycomb structure, the deformation mode of honeycombs under different biaxial loading directions is supposed to be different. The detailed analysis on honeycomb deformation modes can be found in Section 5.3.
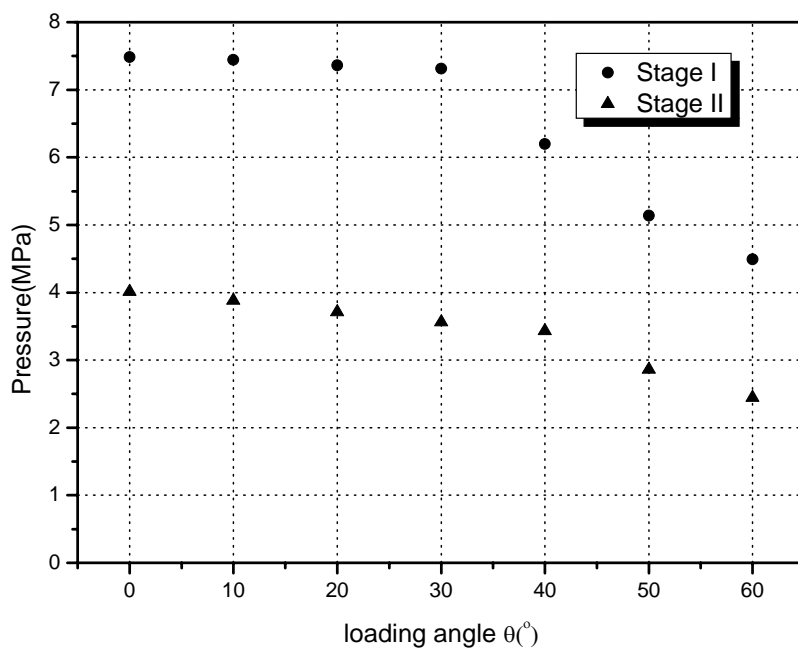
Figure 5.7 Initial peak value and average plateau strength of honeycombs in TW plane and at different loading angle
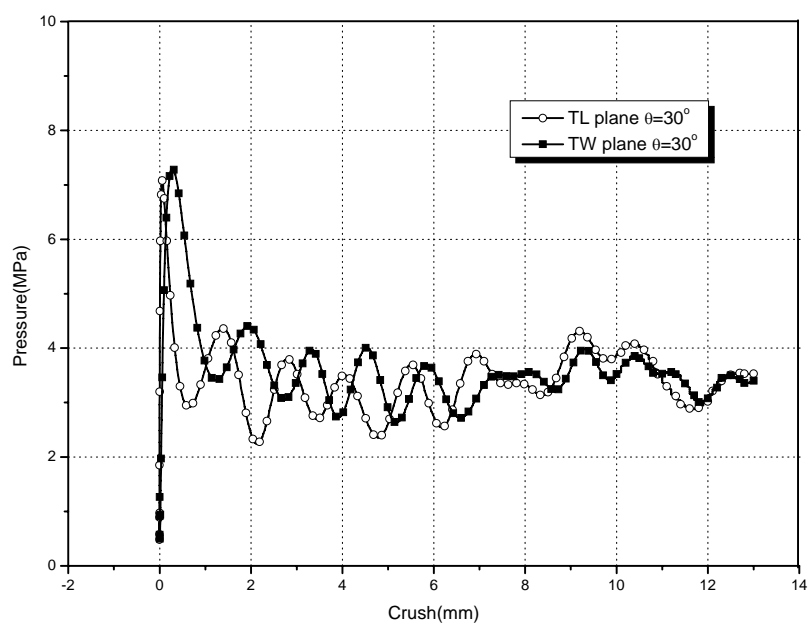
Figure 5.8 Dynamic Pressure/crush curves in two loading plane at $\theta=30^{o}$

The pressure/crush curves of every loading angles in TL plane are shown in Figure 5.9 (excluding the ones of $\theta=10^{o}$ and $\theta=20^{o}$). Similar to the results of TW loading plane, the level of these curves decreases monotonously with increasing loading angle.

In Figure 5.10, the initial peak value and the average strength from both the experimental results of TW and TL loading planes are compared and no significant effect of the out-of-plane biaxial loading direction on honeycomb behavior is found.
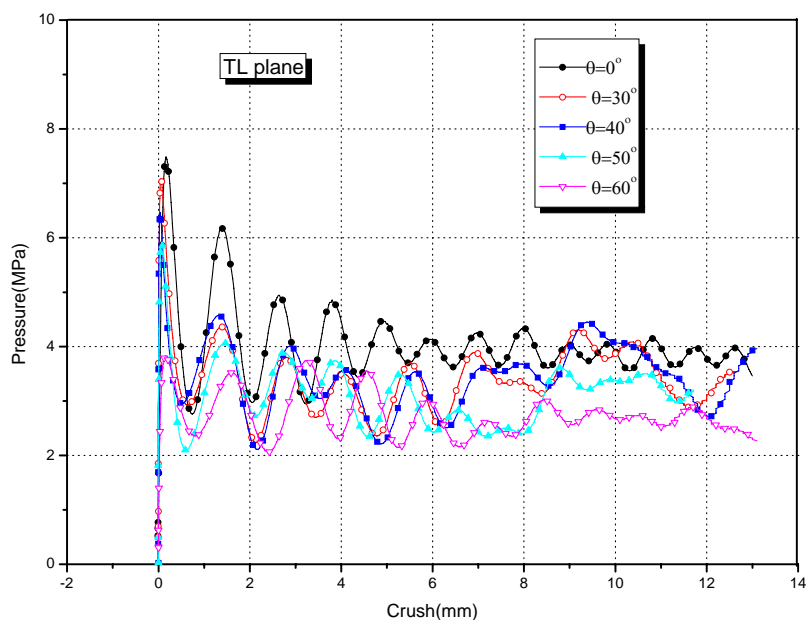
Figure 5.9 Dynamic pressure/crush curves of honeycombs in TL plane at different loading angles
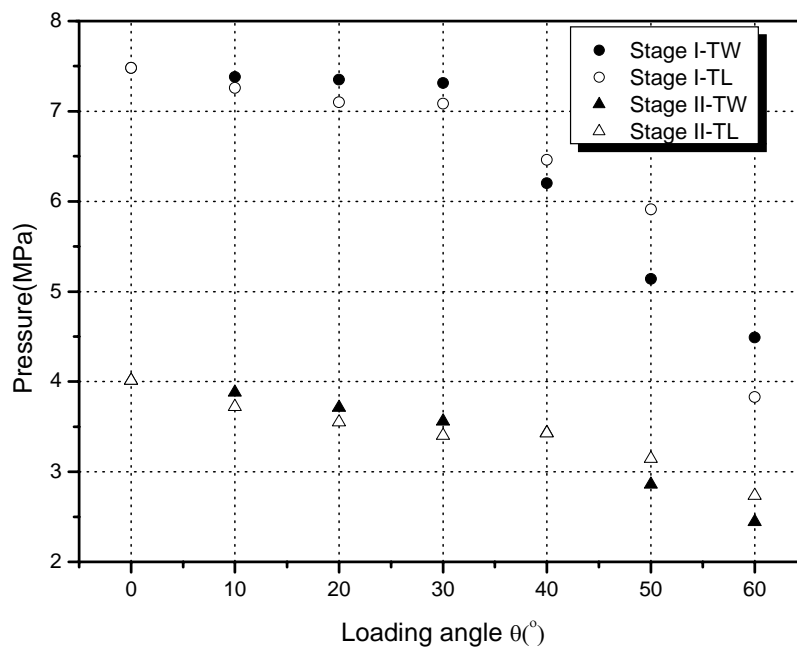
Figure 5.10 Initial peak value and average plateau strength of dynamic honeycomb behavior in TW and TL planes at different loading angle

5.2.3 Quasi-static experimental results under combined shear-compression

The combined quasi-static shear-compression experiments were also performed at seven loading angles and in two loading planes in order to make a comparison with the dynamic experiments.

5.2.3.1 TW loading plane

The experimental results under quasi-static loading are shown in Figure 5.11. All the curves are cut off at 13 mm crush in order to facilitate the comparison with the dynamic results. It is found that the level of these quasi-static curves decreases with loading angle, which is similar to the dynamic results. Besides, additional differences with respect to dynamic experiments are found. Firstly, the quasi-static overall pressure/crush curves are smoother than the dynamic ones. Secondly, the initial peak of quasi-static curves is not as significant as the corresponding dynamic one at every combined loading, and the difference of the ascending slope of each curve is much larger than the dynamic results. Further investigation on the deformation details from the captured images reveals a slight slippage between the specimen and the bevels at the beginning of this combined quasi-static shear-compression test. This may cause errors in predicting the properties of honeycomb in the elastic regime for the quasi-static experiments. Finally, as viewed from the plateau level of each curve, the quasi-static ones are all lower than the corresponding dynamic ones, which shows an obvious effect of dynamic enhancement of honeycombs under combined shear-compression.

All the initial peak values and average strengths of seven quasi-static pressure/crush curves with different loading angles in TW plane are listed in Table 5.1 and displayed in Figure 5.12.

In Figure 5.12, an obvious descending trend was observed for both the initial peak value and the average strength despite of a few particular data points. It is also found that the difference between the initial peak value and the average strength under combined shear-compression is much smaller than under uniaxial compression.
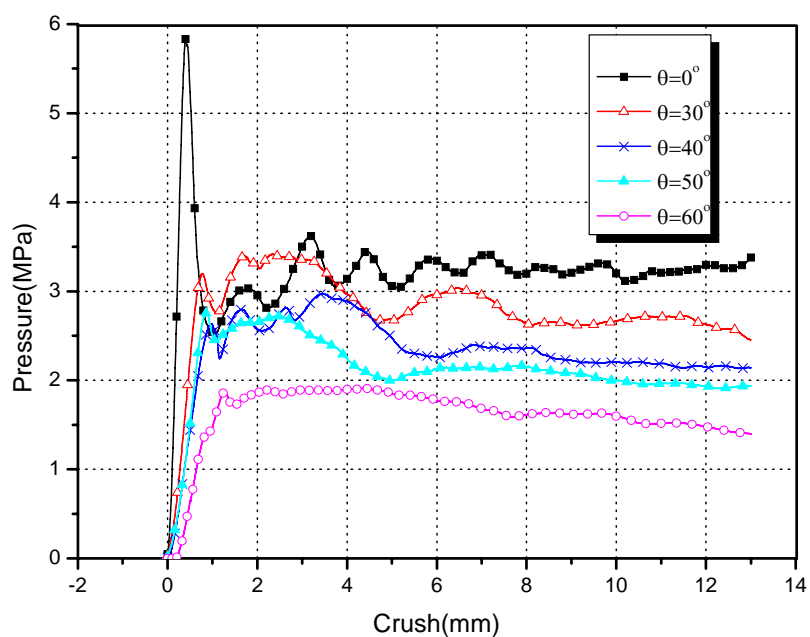
Figure 5.11 Quasi-static Pressure/crush curves of honeycombs in TW plane at different loading angles

Table 5.2 Summary of quasi-static honeycomb behaviors in TW plane

Loading angle θ	0°	10°	20°	30°	40°	50°	60°
Peak value of Stage I (MPa)	5.83	4.58	3.59	3.2	2.63	2.75	1.87
Average strength of Stage II (MPa)	3.22	3.50	3.20	2.92	2.41	2.18	1.65
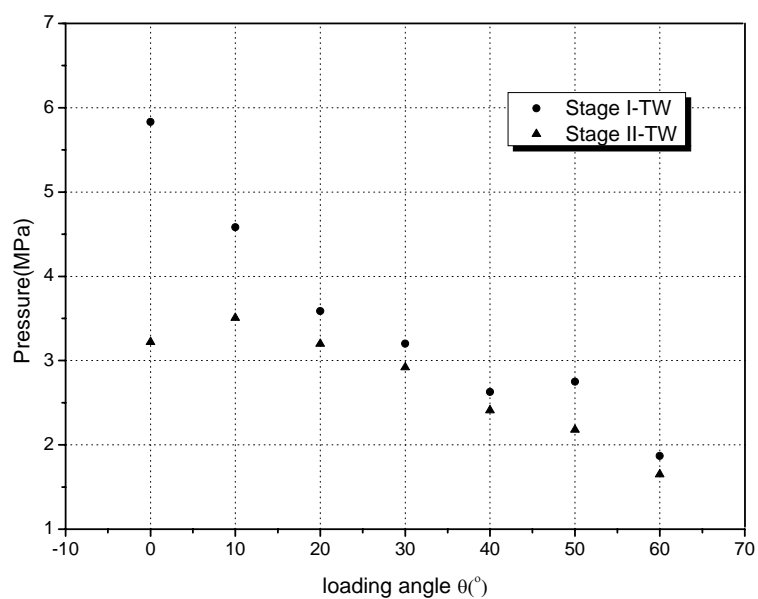
Figure 5.12 Initial peak value and average plateau strength of honeycombs quasi-static behavior in TW plane at different loading angle

5.2.3.2 TL loading plane

The pressure/crush curves at different loading angles are summarized in Figure 5.13, and similar descending behavior of the curve level with loading angles can be observed as in Figure 5.11 for the TW loading plane. Comparison between the initial peak values and the average strengths in TW and TL planes is also performed and the result is shown in Figure 5.14.
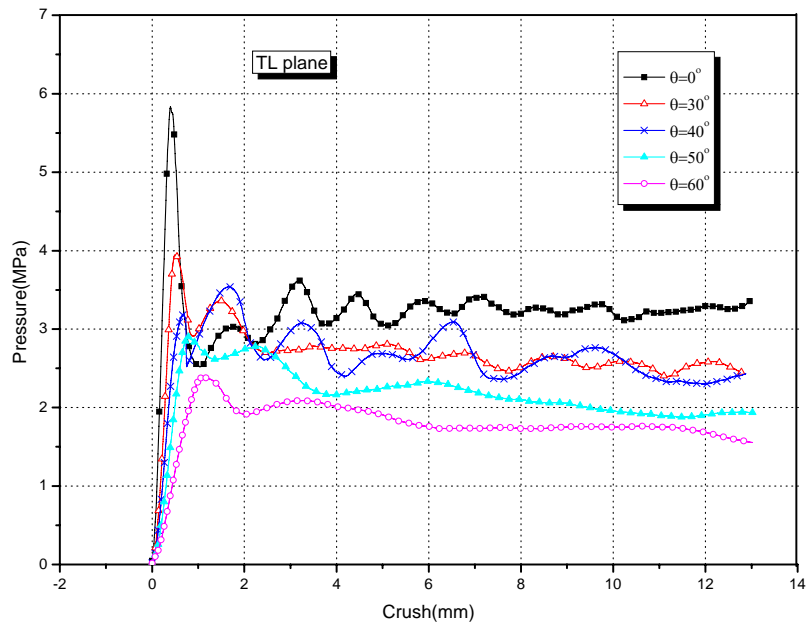
Figure 5.13 Quasi-static pressure/crush curves of honeycombs in TL plane at different loading angles
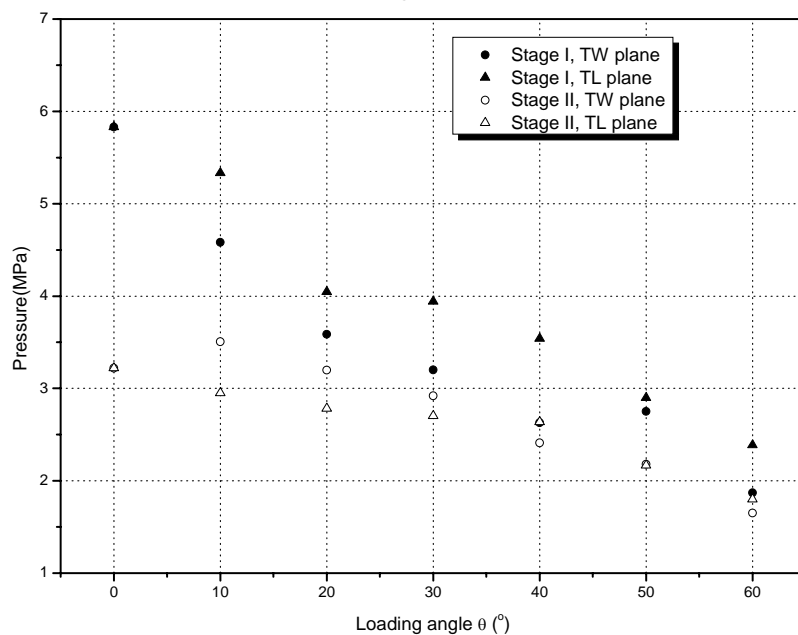
Figure 5.14 initial peak value and average plateau strength of quais-static honeycombs behavior in TW and TL planes at different loading angle

5.2.4 Comparison between dynamic and quasi-static results

It is recalled that the dynamic enhancement of honeycombs under uniaxial compression has been extensively studied both experimentally and numerically in chapter 3 and chapter 4 of this thesis. Here, we are going to investigate the dynamic strength enhancement behavior of honeycombs under combined shear-compressive loading, which has rarely been refered in open literatures.

5.2.4.1 TW loading plane

Figure 5.15 presents the quasi-static and dynamic pressure/crush curves in TW plane for both the uniaxial compression and the combined shear-compression. In order to make a clear comparison, only a representative case of combined shear-compression with $\theta=50^{o}$ is displayed. It can be found in Figure 5.15 that the strength of honeycombs shows obvious dynamic enhancement effect not only under uniaixal compression, but also under combined shear-compression.
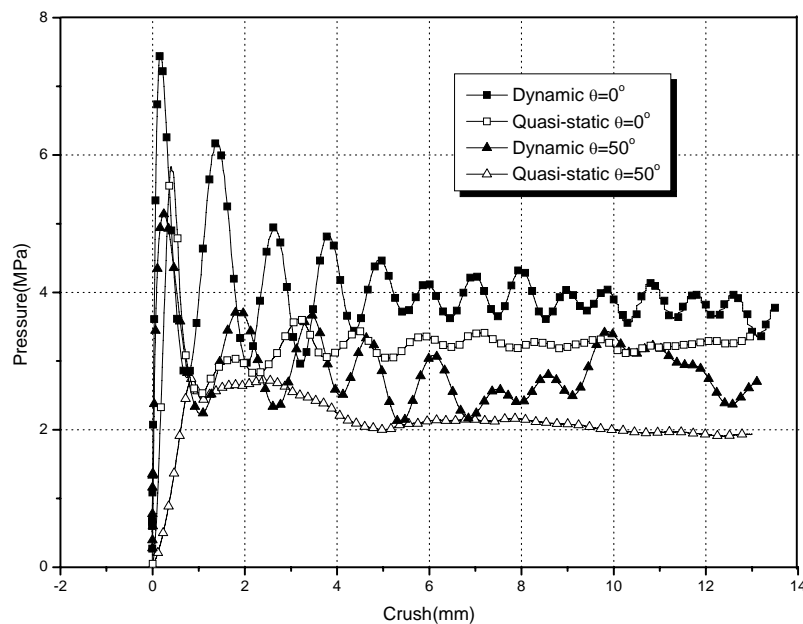
Figure 5.15 Quasi-static and dynamic pressure/crush curves in TW plane at $\theta=0^{o}$ and $\theta=50^{o}$

This dynamic enhancement phenomenon of honeycombs strength is also found for the other loading angles of combine shear-compression. All the initial peak values and average strengths at plateau stage are listed in Table 5.3 and drawn in Figure 5.16, which indicate more clearly the difference between dynamic results and quasi-static ones.

The initial peak values of stage I are correlative with the initial imperfections in honeycomb structures and may contain some uncertainty. Regardless of the potential errors of the quasi-static results at initial deformation for the combined loading cases, it can be seen from Figure 5.16 (a) that the initial collapse strength of honeycomb under dynamic loading is significantly higher than under quasi-static loadings. The dynamic enhancement rates are between 34.5％ and 162％. The comparison of crushing strength at stage II between dynamic and quasi-static results is shown in Figure 5.16(b). An enhancement varying from 10.5% to 48.5% is found from the dynamic curves to the quasi-static ones.

Table 5.3 Comparison between dynamic and quasi-static results at two loading stages (TW plane)

	Loading angles θ	0°	10°	20°	30°	40°	50°	60°
Stage I	Quasi-static initial peak value (MPa)	5.83	4.58	3.59	3.2	2.63	2.75	1.87
	Dynamic initial peak value (MPa)	7.48	7.38	7.35	7.31	6.20	5.14	4.49
	Dynamic enhancement rate	34.5%	30.8%	77.7%	128%	136%	86.9%	162%
Stage II	Quasi-static average strength (MPa)	3.22	3.51	3.20	2.92	2.41	2.18	1.65
	Dynamic average strength (MPa)	4.01	3.88	3.71	3.56	3.43	2.86	2.45
	Dynamic enhancement rate	24.5%	10.5%	15.9%	21.9%	42.3%	31.2%	48.5%

(a)

(b)
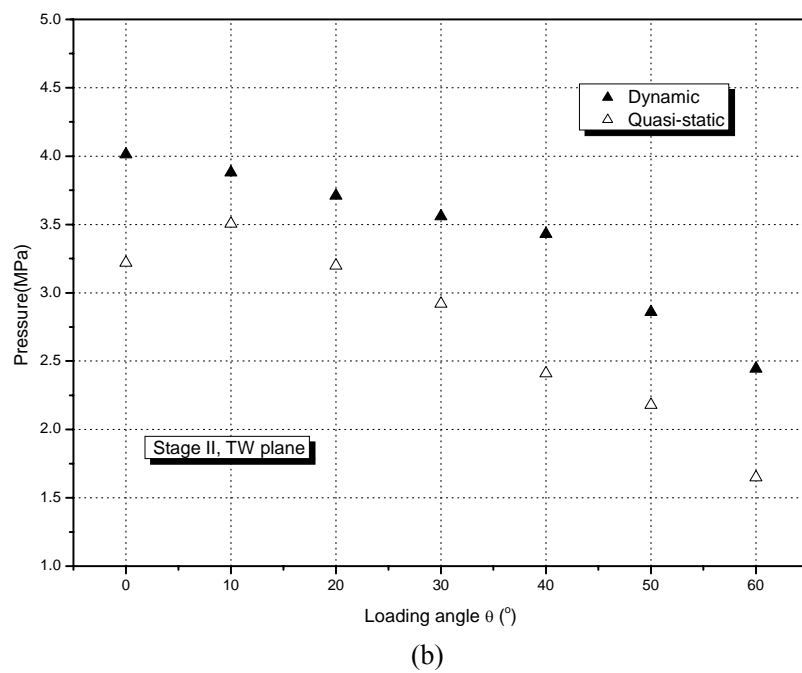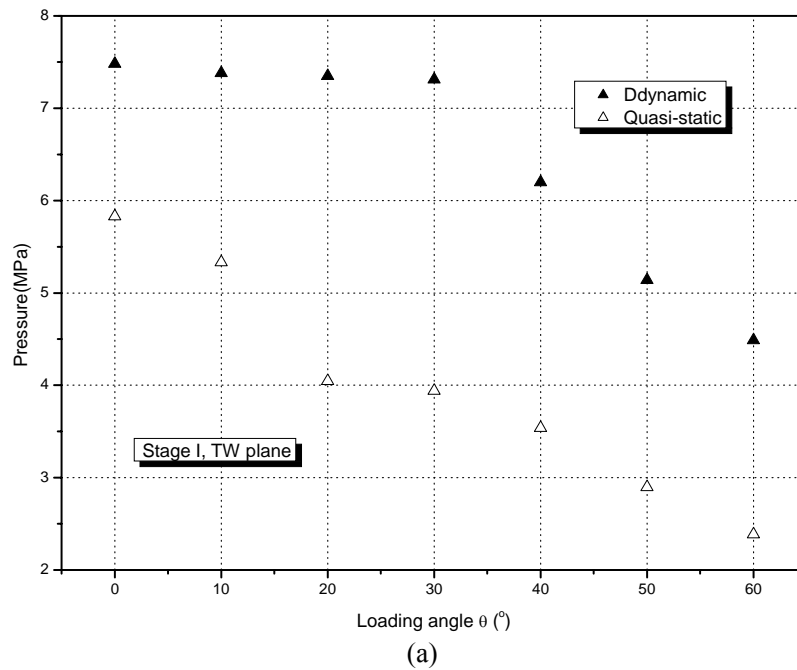
Figure 5.16 Comparison between dynamic and quasi-static results in Stage I (a) and Stage II (b) (TW plane)

5.2.4.2 TL loading plane

Similarly to the TW loading plane, the comparison between quasi-static and dynamic results in TL plane is also performed for both uniaxial compression and combined shear-compression. Figure 5.17 shows the quasi-static and dynamic

pressure/crush curves in TL plane at the loading angles of $\theta=0^o$ and $\theta=50^o$ and same dynamic enhancement effects are observed. All the initial peak values and average strengths at plateau stage are listed in Table 5.4 and drawn in Figure 5.18. The dynamic enhancement rate for initial peaks in Stage I is between 28.3% and 103.8% with large scatter, while, the average strength of Stage II is elevated from quasi-static loadings to dynamic loading much more evenly.
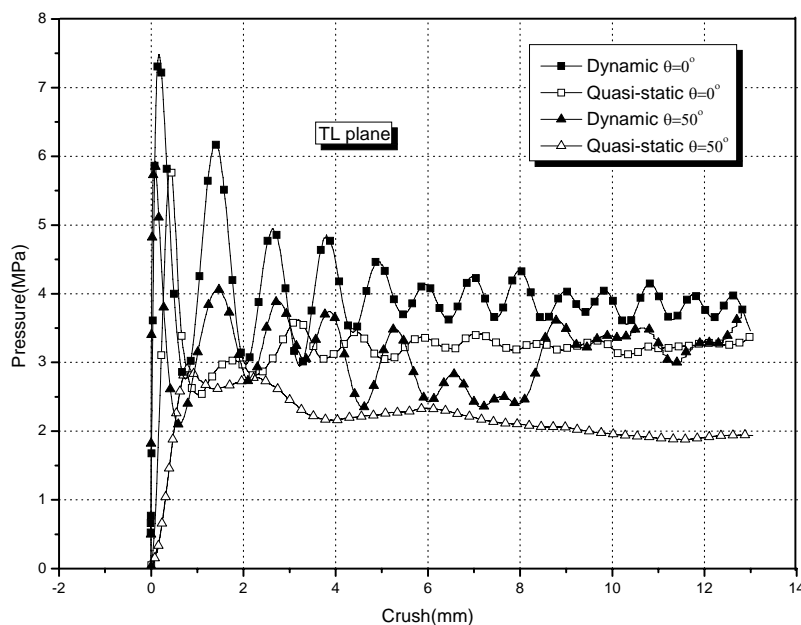
Figure 5.17 Quasi-static and dynamic pressure/crush curves in TL plane at $\theta=0^o$ and $\theta=50^o$

Table 5.4 Comparison between dynamic and quasi-static results at two loading stages (TL plane)

	Loading angles	0°	10°	20°	30°	40°	50°	60°
Stage I	Quasi-static initial peak value (MPa)	5.83	5.33	4.05	3.94	3.54	2.90	2.39
	Dynamic initial peak value (MPa)	7.48	7.26	7.10	7.08	6.46	5.91	3.83
	Dynamic enhancement rate	28.3%	36.2%	75.3%	79.7%	82.5%	104%	60.3%
Stage II	Quasi-static average strength (MPa)	3.22	2.95	2.78	2.70	2.64	2.17	1.80
	Dynamic average strength (MPa)	4.01	3.72	3.55	3.40	3.43	3.14	2.73
	Dynamic enhancement rate	24.5%	26.1%	27.7%	25.9%	29.9%	44.7%	51.7%
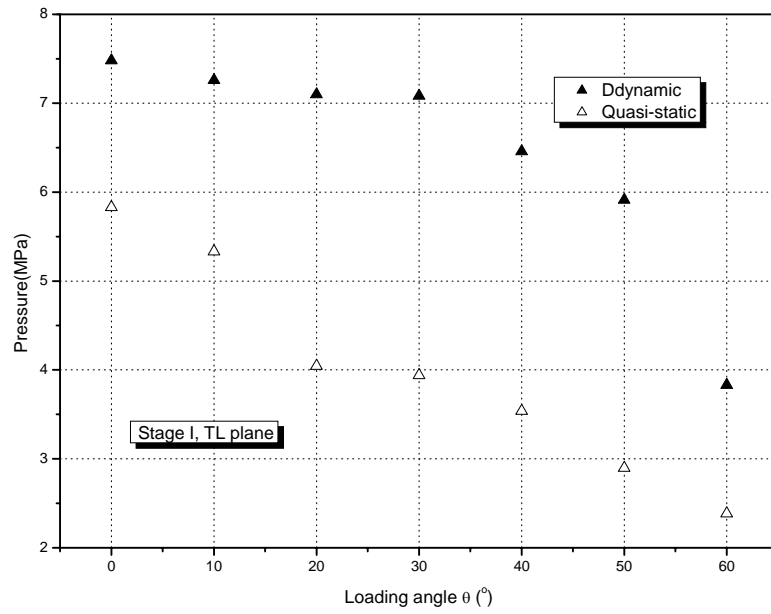
(a)
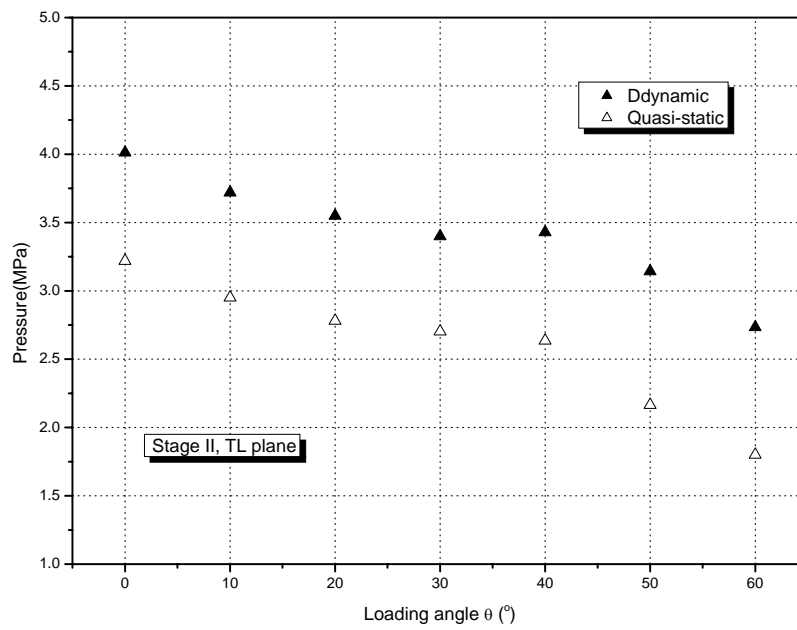
(b)

Figure 5.18 Comparison between dynamic and quasi-static results in Stage I (a) and Stage II (b) (TL plane)

5.3 Deformation pattern observations of honeycombs

5.3.1 TW loading plane

In our tests, the deformation process of honeycomb under combined shear-compression was captured by high-speed camera. The influence of biaxial loading state on the deformation pattern of honeycombs is investigated. According to the experimental observations on honeycomb deformation, two deformation mechanisms are proposed to explain the co-existing deforming modes of honeycombs under combined shear-compression.

Figure 5.19 presents a series of dynamic deforming patterns of honeycomb under both uniaxial compression and combined shear-compression at $\theta=30^{\circ}$. The first images of Figure 5.19 (a) and (b) correspond to the undeformed configurations. As the deformation continues, differences between the uniaixal compression and combined shear-compression are observed as follows: Firstly, the position of the initial collapse is different (as shown in the images at crush of 0.1mm). For the uniaxial compression, the collapse initiates at either the top or the bottom face evenly. Whereas for combined loading, it occurs simultaneously at the top and bottom faces but in a diagonally corresponding positions. Secondly, when the specimen deforms further, the cell axes of the honeycomb specimen under combined loading incline due to the presence of shear load, while the uniaxial compressive specimen keeps their cell-wall axes perpendicular to the loading surfaces.

It seems that the deformation of honeycombs under combined shear-compression is characterized by the incline of cell axis at the action of shear component. In fact, this inclined deformation mode (denoted as Mode I) was found in most of the combined shear-compression experiments including dynamic and quasi-static loadings. However, for a minority of the specimens under combined shear-compression (even with large loading angle), a deformation mode similar to uniaxial compression was also found. As shown in Figure 5.20, one of the specimens at $\theta=50^{\circ}$ was crushed from one end of the specimen with the cell-wall axes perpendicular to the loading faces. This deforming mode is denoted as Mode II, which enables a higher loading capacity.
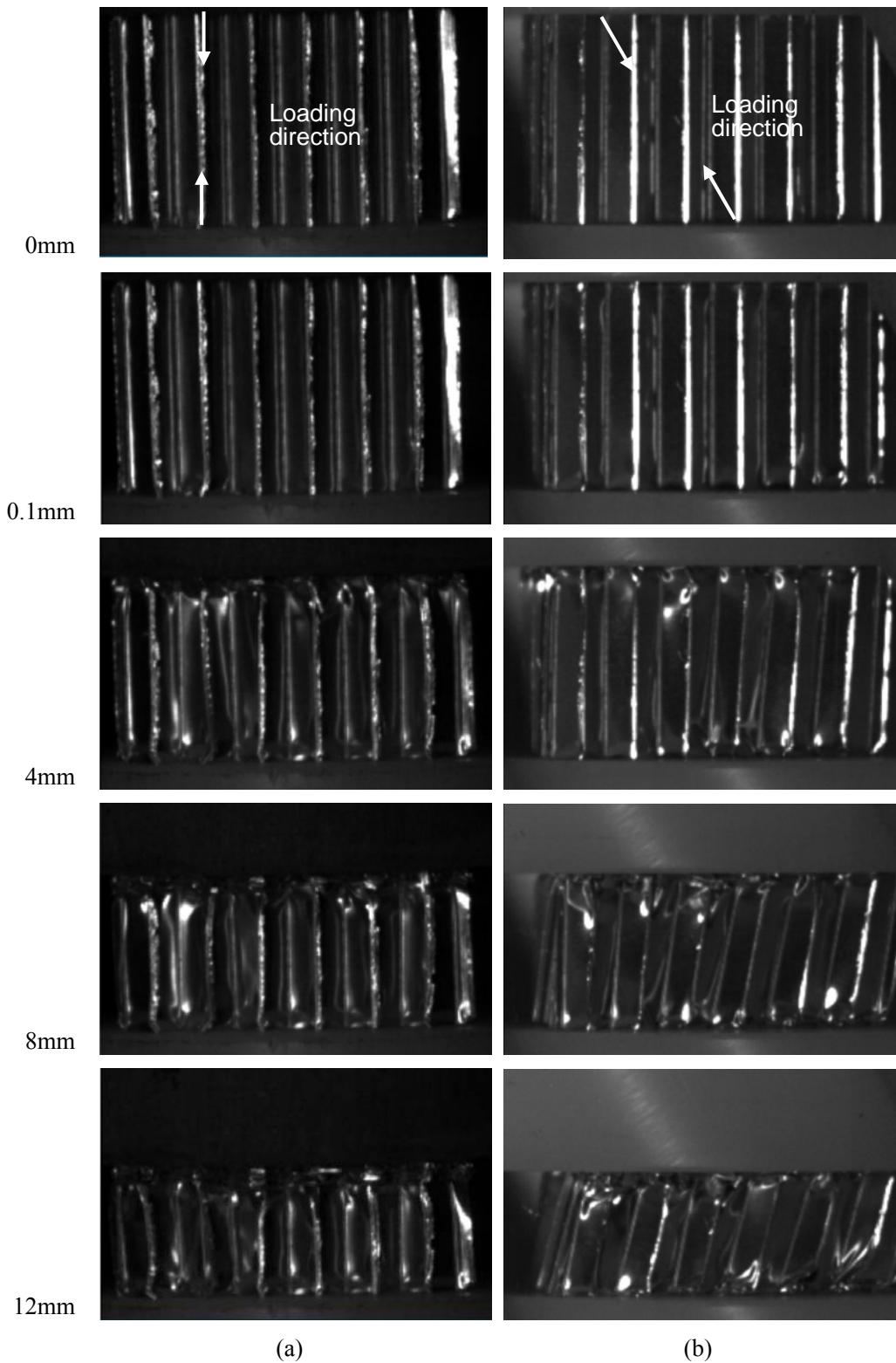
Figure 5.19 Dynamic deformation images under uniaxial compression (a) and combined shear-compression at θ=30° (b) at different crush value.
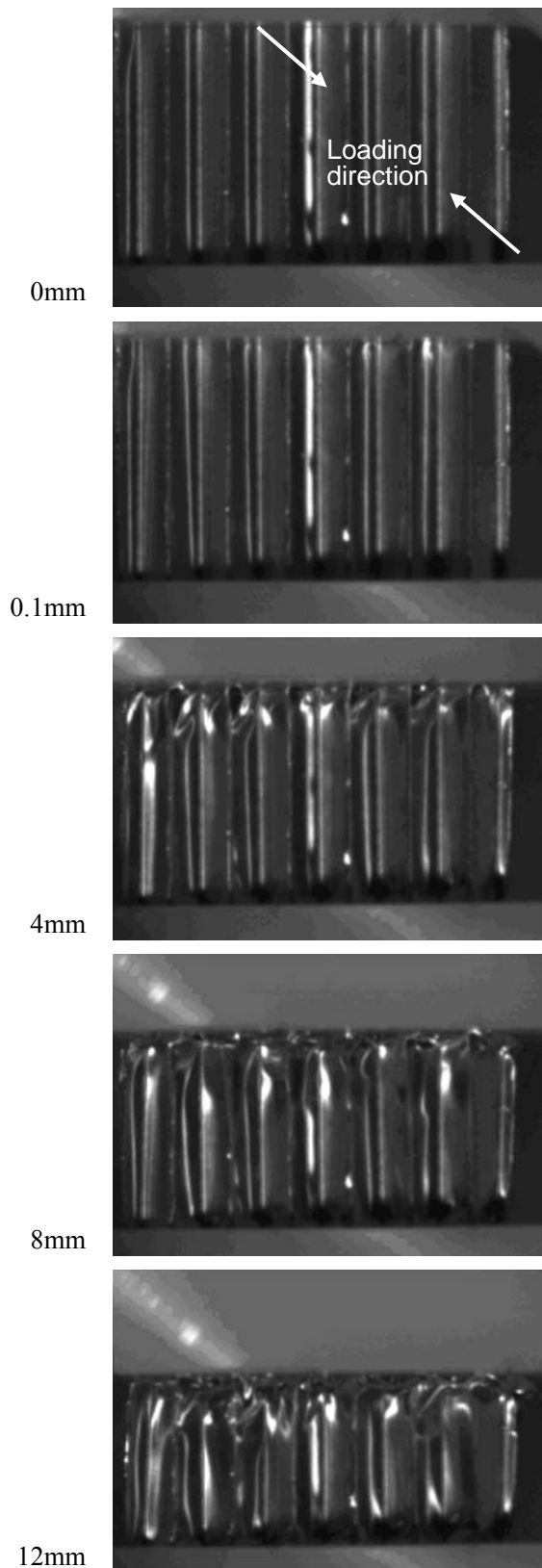
Figure 5.20 Deformation mode II of honeycomb under dynamic combined shear-compression found at θ=50°

The deformation process on honeycombs under combined quasi-static shear-compression is also examined and the same two deformation modes as in dynamic results are found for some individual specimens. Figure 5.21 presents the deformation process of honeycomb specimen under quasi-static combined shear-compression of θ=50°. Thereinto, Figure 5.21(a) shows the photo series of Mode I deformation and Figure 5.21(b) for Mode II.

12mm

| (a) Mode I | (b) Mode II |
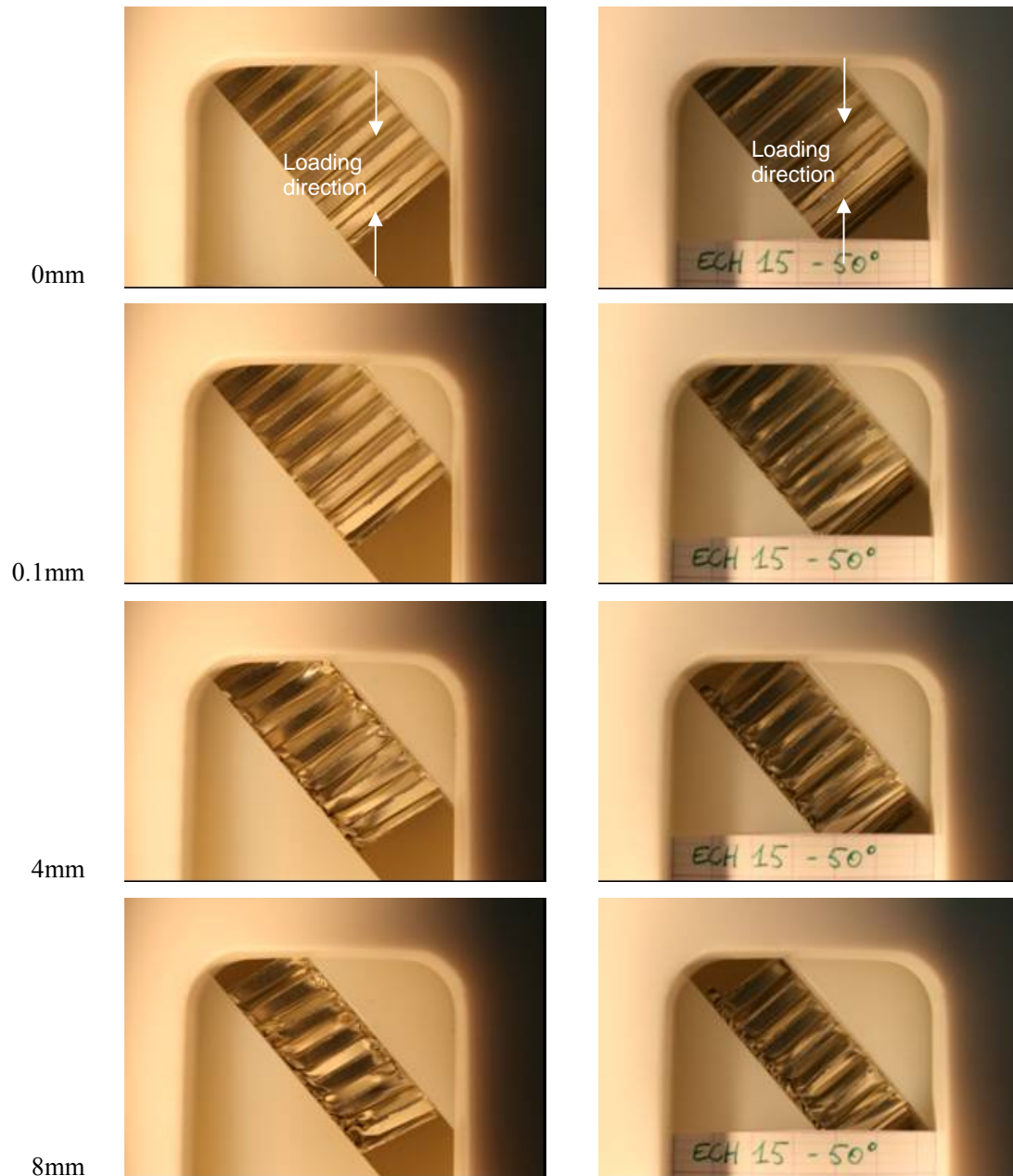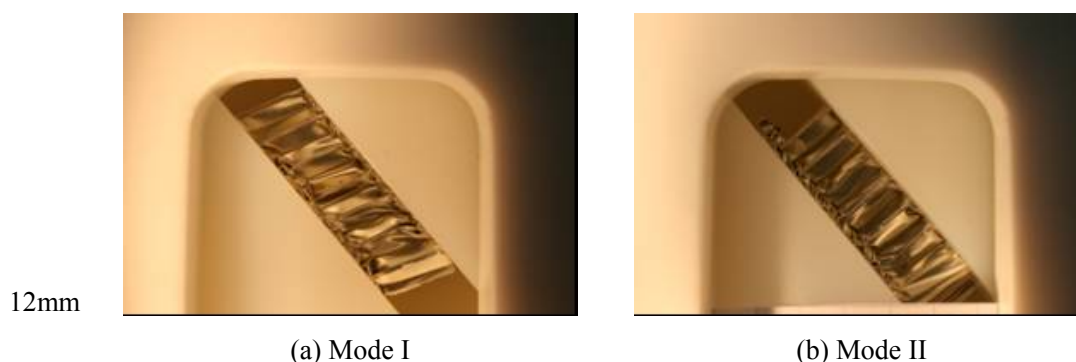
Figure 5.21 Two deformation modes of honeycombs under quasi-static combined shear-compression(TW plane)

In general, the deforming pattern under combined shear-compression might be summarized as follows: there co-exist two patterns allowing the honeycomb to cope with this prescribed shear-compression loading. One possibility is to allow the rotation of the central part, which is an off-axis local buckling mechanism so that the cells in the central part incline globally during the deformation (Figure 5.22(a)); Another possibility is to maintain the central part with no rotation as for uniaxial compression, but the shear loading induces an overall translation of the buckled cell relative to the non compacted cell (Figure 5.22(b)). There is a competition of those two different deforming modes during a test.
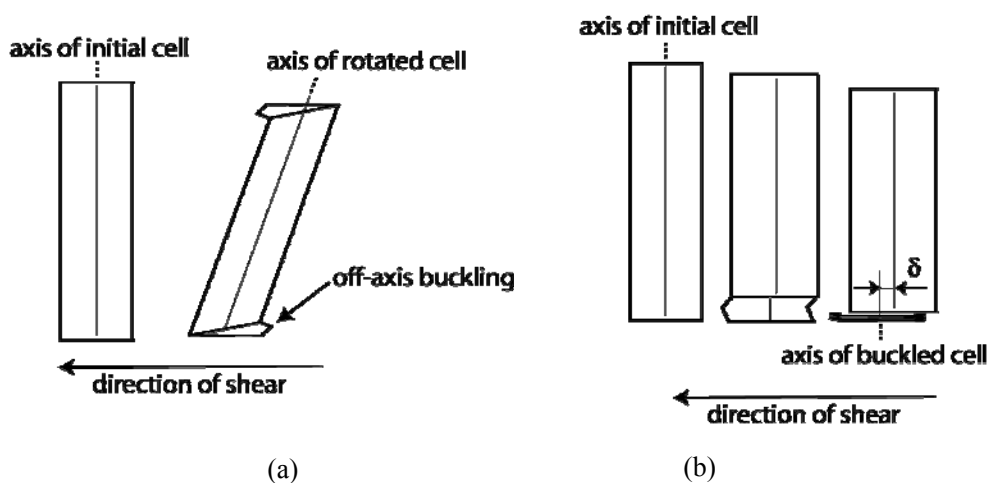
Figure 5.22 Scheme of deforming modes under combined shear-compression (a) rotation, (b) no rotation

Figure 5.23 presents the pressure/crush curves corresponding to this two different deformation modes of honeycomb specimens under the same loading condition (quasi-static, $\theta = 50^o$). It has been demonstrated that Mode I works with global incline of honeycomb cell walls, which leads to a lower loading capacity of

honeycomb at macroscopic level. It can be seen in Figure 5.23 that the pressure/crush curve of Mode I shows obvious softening behavior after initial collapse. While in Mode II, the buckling occurs very locally at the interface of the crushed part and the uncrushed part of honeycomb cells and the folding process develops in a successive way. Mode II deformation enables a higher loading capacity of honeycombs under combined shear-compression as shown in Figure 5.23.
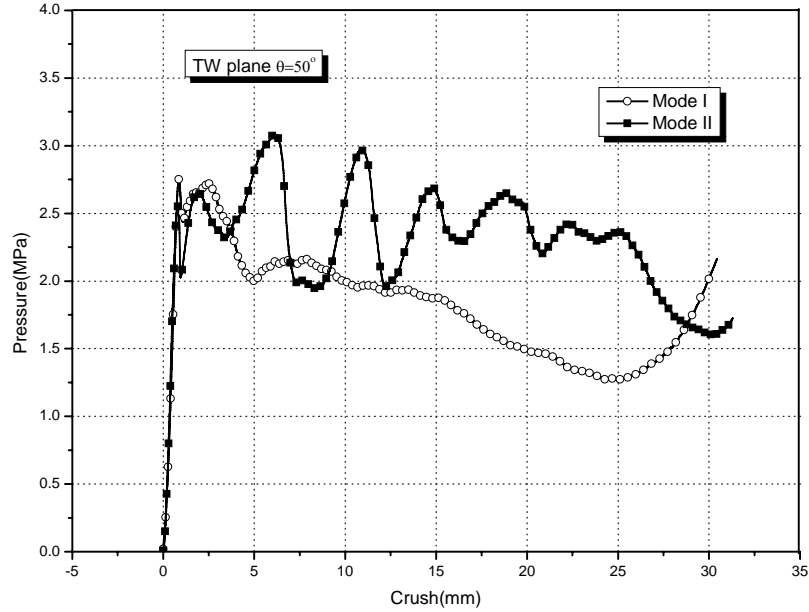
Figure 5.23 Pressure/crush curves of honeycombs with two different deforming modes

Actually, there is a competition between these two different deforming modes of honeycombs under combined shear-compression during a test. The final choice of honeycomb to deform in Mode I or Mode II have relations with the random initial imperfections in honeycomb structure. In order to obtain a general viewpoint of this competition of two deformation modes and especially the influence of the loading rate on it, a quantitative analysis is made by means of indicators taken from the image sequences acquired during experiments at various loading angles. The rotation angle β of the cells during crushing is represented by the angle between the initial orientation of cell axes (perpendicular to the faces of the bevels) and their current orientation. This rotation angle β is a function of mean compressive strain ε which can be defined as the relative variation of specimen length:

$$\varepsilon = (h_0 - h)/h_0 \qquad\qquad 5.2$$

where h and h_0 are respectively the distances of the two bevels before and after the deformation (as shown in Figure 5.24).
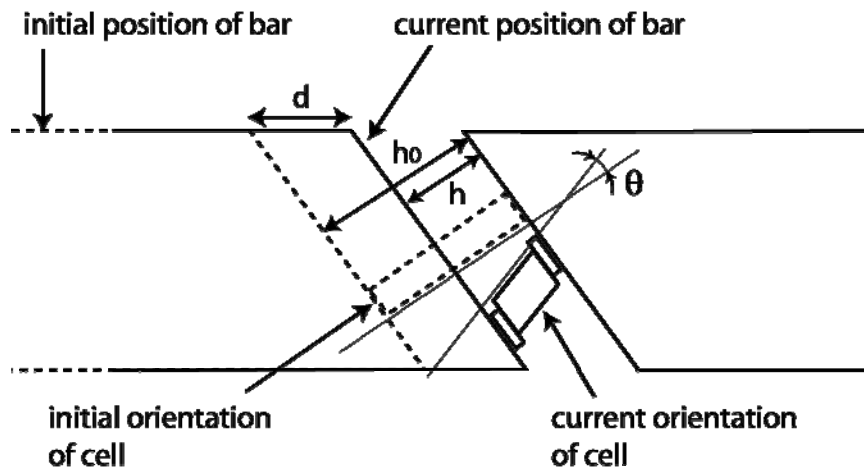
Figure 5.24 Scheme for the image analysis

Figure 5.25 collects all the rotation angles at ε=40% for all the loading angles under quasi-static and dynamic loadings. It confirms that there is a competition between those two deforming modes. Apart from the tests at 30°, it seems that, there are both possibilities to remain not rotated or rotate significantly under dynamic and quasi-static loadings. The larger the loading angle is, the more important the rotation angle becomes. Another rather clear trend is that the probability of rotation is much higher under quasi-static loading than under dynamic loading.
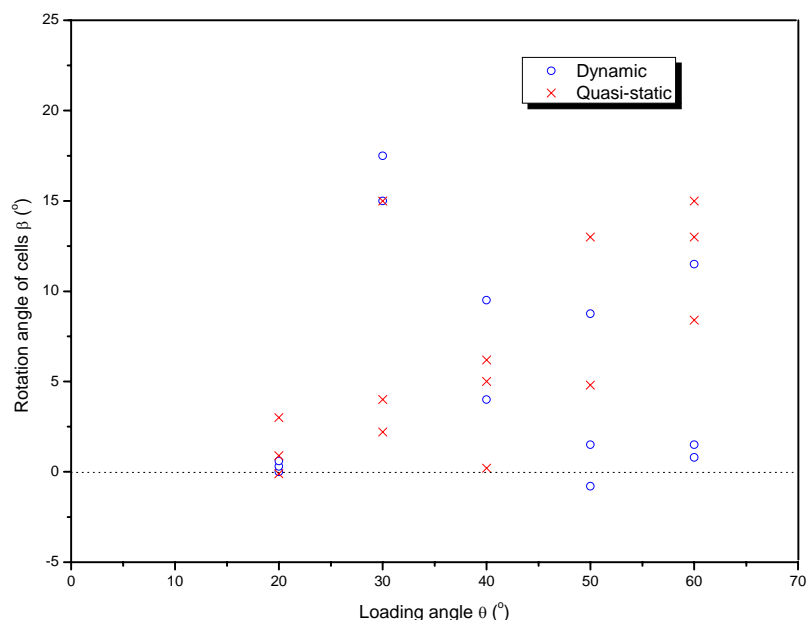
Figure 5.25 Rotation angle of cell axes at 40% compression (TW plane）

A close look of the case for a loading angle θ=60° (most important shear component) is shown in Figure 5.26. It shows that tests at θ＝60° under dynamic

loading mainly remain not rotated whereas tests under quasi-static loading mainly rotate and this is true at any state of crush. Such a difference of deforming modes between quasi-static and dynamic loading might provide an explanation of the enhancement of strength under combined impact shear-compression.
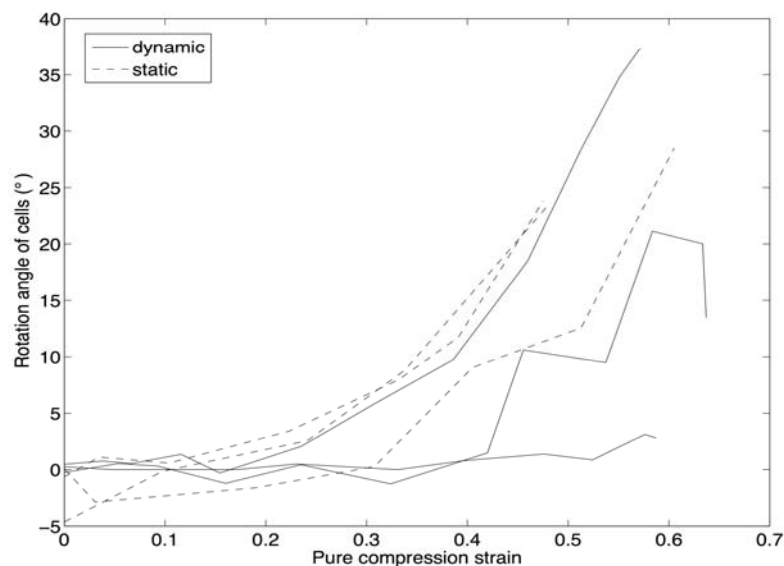
Figure 5.26 Rotation angles during tests at a loading angle of 60° (TW plane）

5.3.2 TL loading plane

Honeycombs under combined shear-compression in TL plane have the similar deformation patterns as in TW plane. Figure 5.27 shows the photo series of honeycombs deforming dynamically at $\theta=40^{o}$ in respectively Mode I (Figure 5.27 (a)) and Mode II (Figure 5.27 (b)).

0mm

0.1mm

4mm

8mm

12mm

(a) Mode I   (b) Mode II
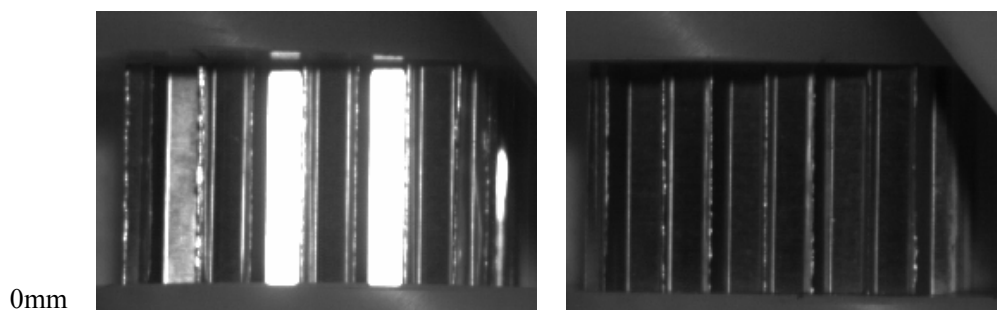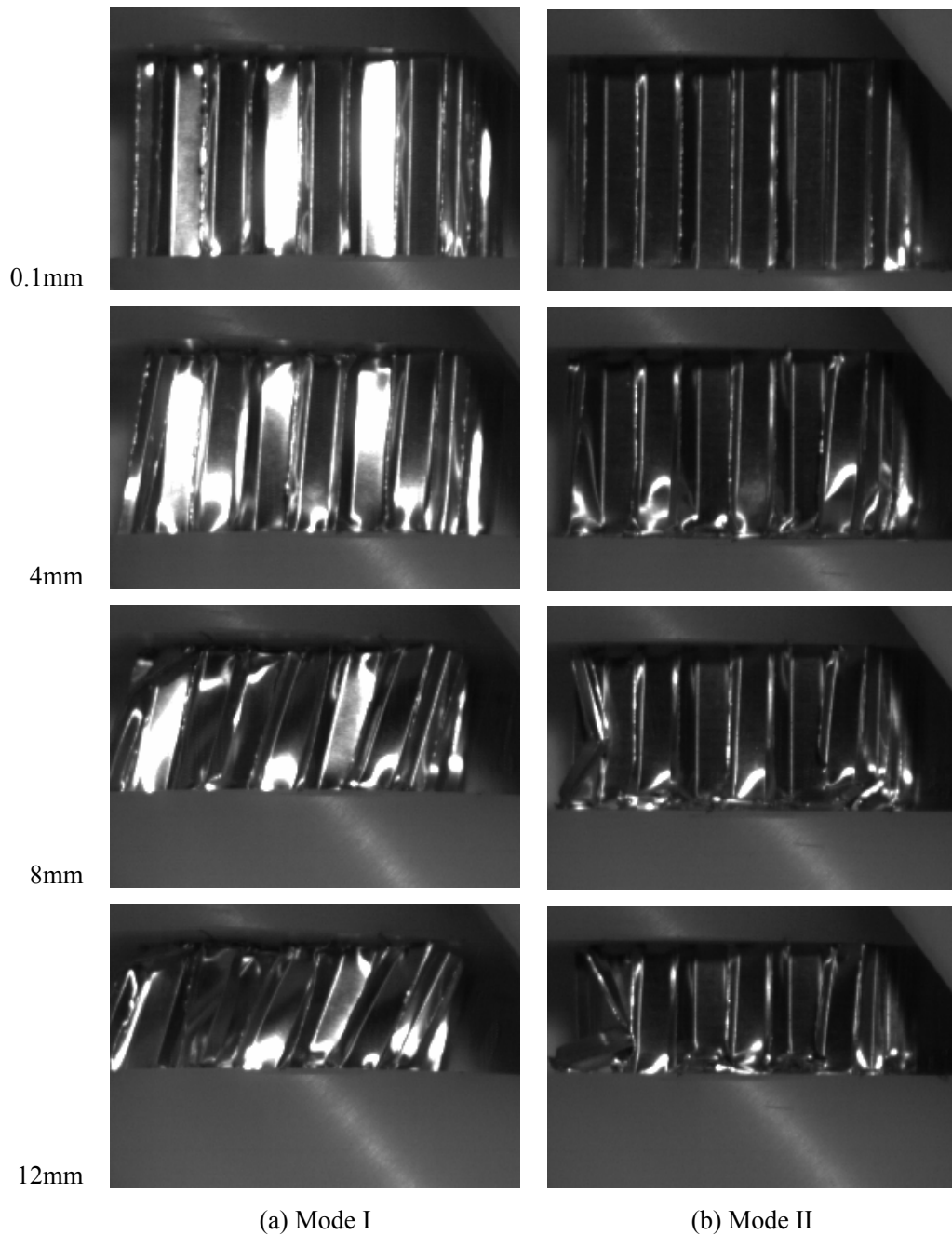
Figure 5.27 Two deformation modes of honeycombs under dynamic combined shear-compression(TL plane)

It has been shown that the pressure/crush curves of honeycomb in TW plane and in TL plane are with almost the same levels, which means that the honeycomb strength under out-of-plane biaxial loading is rarely influenced by the loading directions. As to the deformation details, honeycombs have different micro-structure in this two in-plane directions, which will introduce differences to the deformation process on folding wave length or folding direction for both the thin-walls or the thick-walls of honeycomb structure. The deforming configurations of honeycomb in

126

TW and TL loading planes are displayed in Figure 5.28. For each case, two deformation modes are all displayed.

$\theta=50^{o}$
Mode I

$\theta=10^{o}$
Mode II

TW plane   TL plane

Figure 5.28 comparion between deformation mode of honeycombs in TW and TL planes

Figure 5.29 collects all the rotated angles for honeycombs under combined shear-compression in TL plane. Despite of data scatter effect, most of the specimens are involved into mode I deformation pattern and only a few specimens deform in Mode II. Similar to the results in TW loading plane, it can be concluded in general for the TL loading plane that the possibility for honeycomb cell axes to rotate increases with increasing loading angle θ, and the rotated angle β becomes also more important with larger loading angle θ. Moreover, the probability of rotation is higher under quasi-static loading than under dynamic loading.

Figure 5.29 Rotation angle of cell axes at 40% compression(TL plane）

5.4 Limitation of the combined shear-compression device

It is worthwhile to reiterate that the tests conducted above do provide a combined shear-compression loading because of the friction between introduced beveled bars and the tested specimen. The results show that the decrease of the strength with loading angle is rather obvious, however, the measured strength in axis direction (X_3) is not simply equal to the projection of the honeycomb strength under pure compression in this direction. For example, the measured value at $\theta=60°$ is not the half of that at $\theta=0°$ (Table 5.4).

In fact, the present testing method provides a new way for obtaining the overall behavior of honeycombs under combined shear-compression at various loading angles, which are of much importance for engineering applications. However, further investigation of the multi-axial behavior of cellular materials requires to study the normal and shear behaviors separately. Unfortunately, the normal and shear information on the specimen faces can not be obtained directly from the present testing set-up. The relationship between the measurable quantities and the normal and shear data on specimen faces are examined hereby.
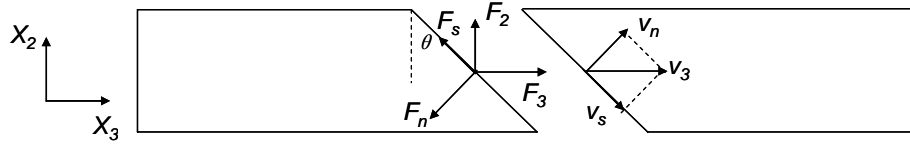
Figure 5.30 Scheme of the force balance and the decomposition of velocity

In Figure 5.30, we denote the force and velocity components in global coordinate F_i and V_i (i=1, 2 and 3). The pressure bars provides F_3 and V_3 in the axial direction. Denoting F_n, V_n and F_s, V_s respectively the forces and velocities applied to specimen faces in normal and shear directions. They are related as follows:

$$V_1 = 0$$

$$V_2 = 0$$

$$V_3 = V_n / \cos\theta = V_s / \sin\theta \qquad\qquad 5.3$$

$$F_1 = 0$$

$$F_2 = F_n \sin\theta - F_s \cos\theta$$

$$F_3 = F_n \cos\theta + F_s \sin\theta \qquad\qquad 5.4$$

Under the assumption of identical movements of the beveled ends which was validated in FEM simulations, V_n and V_s can be calculated from a simple expression obtained from the decomposition of V_3. However, the use of the supports in the combined shear-compression device results in the emergence of a transverse reaction force F_2 which is not measurable in the experimental design. Thus, F_n and F_s can not be calculated from Equation 5.4 without the knowledge of F_2. Since normal and shear forces applied to the specimen faces are not separable, it is then impossible to determine the multi-axial constitutive relation directly using the present biaxial loading device.

In order to solve this problem, we are going to install a numerical model of detailed honeycomb structure in next chapter to reproduce the combined shear-compression experiments virtually and the separation of normal and shear behaviors of honeycombs under combined shear-compression is achieved basing on the calculating results.

5.5 Summary

By using the combined shear-compression loading device presented in Chapter 4, the dynamic and quasi-static multi-axial behavior of honeycombs under combined shear-compression were investigated experimentally in this chapter. Two loading planes of TW and TL, and seven loading angles ranging from $\theta=0^o$ to $\theta=60^o$ were included. Good reproducibility was confirmed for both dynamic and quasi-static loading cases. The main conclusions from the experimental results can be summarized as follows:

Firstly, the obtained dynamic and quasi-static pressure/crush curves show that both the initial peak value and the average plateau strength decrease significantly with increasing loading angle.

Secondly, the behaviors of honeycombs under combined shear-compression in respective TW and TL planes are close to each other.

Thirdly, an obvious enhancement of both the initial peak value and the average plateau strength is found for dynamic curves comparing with quasi-static ones at every loading angle. Moreover, this enhancement is more significant at larger loading angle, which can reach 50%.

Finally, from high-speed photographs, the difference of the deformation mode under combined shear-compression from the one under uniaixal compression is identified. Two co-existing deformation modes under combined shear-compression are determined and the influence of loading rate on the competition of these two deforming modes is also included.

The combined shear-compression loading device presented in this paper provides an overall behavior of cellular materials under these multi-axial loading conditions but it cannot give directly the separated normal and shear components of the behavior. A numeric method will be presented in Chapter 6 of this thesis in order to overcome this difficulty.

Chapter 6 Numerical study on honeycomb behaviors under combined shear-compression

In this chapter, a numerical virtual model of honeycomb specimen as a small structure is used to simulate its combined shear-compression behavior under impact loading. With ABAQUS/Explicit code, the response of such a structure made of shell elements is calculated under prescribed velocities as those measured in the combined shear-compression tests presented in Chapter 5 of this thesis. Section 6.1 installs three FE models at different simplifying levels and the consistency of these models are checked. The simulated results displayed in Section 6.2 are compared with the experimental ones in terms of overall pressure/crush curves and deformation modes. In Section 6.3, the normal behavior and shear behavior of honeycomb specimen under dynamic combined shear-compression is separated and investigated individually. A crushing envelope in normal strength vs. shear strength plane was obtained on the basis of these simulations. The numerical method presented in this chapter works as a complementary means to the combined shear-compression experiments performed in Chapter 5 for investigating the biaxial behavior of honeycombs.

6.1 Installation of FE models

Since the study is focused on the behavior of honeycombs under a combined out-of-plane shear-compression, the modeling of the whole testing environment is not necessary. Thus, only detailed honeycomb structures were modeled here and the loading environment was modeled by two rigid planes moving at the velocities measured during real tests. Commercial FEM code of ABAQUS/Explicit was employed for this simulation work.

6.1.1 Complete model

The honeycomb structure studied here has the same geometry as the hexagonal honeycomb used in the experiments in Chapter 5. It is composed of single-thickness walls (or thin walls) and double-thickness walls (or thick walls), and the main geometric parameters were as follows: single wall thickness t=76μm, expansion angle

$\alpha=30^o$, and the minimum cell diameter S=6.35mm (as shown in Figure 6.1(a)). The rectangular specimens are with dimensions of $25 \times 40 \times 40$mm in T W and L directions respectively (as shown in Figure 6.1(b)) and includes 39 complete honeycomb cells in the cross section.

t=76μm
S=6.35mm
α=30o

(a)   (b)
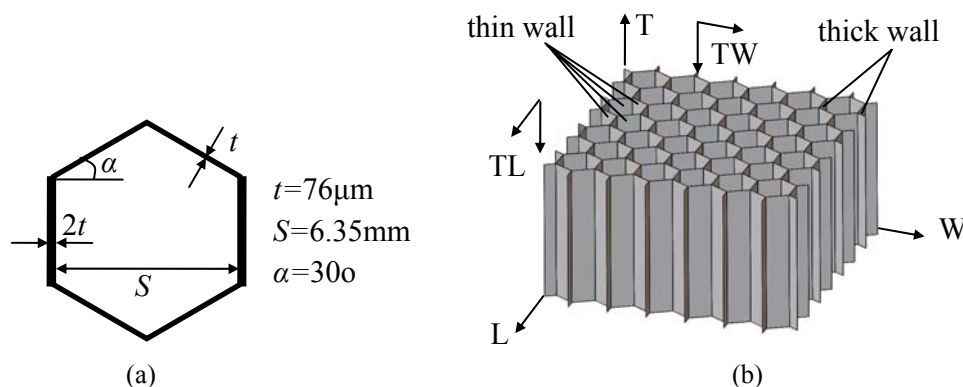
Figure 6.1 The geometry of unit cell (a) and the constructed honeycomb specimen (b)

We firstly build a complete-model which possesses the same size as honeycomb specimens used in the experiments in Chapter 5. The thick walls in a real honeycomb are typically made of two single-thickness thin walls which are bonded together. In this model, we ignore the rare delamination of the bonded interfaces and consider the strength of the adhesive bond as infinite. Thus, the simulations are carried out for a monolithic honeycomb, where the thick walls are represented by a single shell element layer but with a doubled thickness value.

The model is meshed with 4-node doubly curved thick shell elements with a reduced integration, finite membrane strains, active stiffness hour-glass control (S4R) and 5 integration points through the cell-wall thickness. In order to determine the appropriate element size, a convergence study was performed among element sizes of 1mm, 0.5mm, 0.25mm and 0.125mm. It seems that the results converge when the element size is equal to or below 0.25mm. With the chosen element size of 0.25mm, our complete-model has totally 232600 elements.

The numerical specimen is placed between two rigid planes moving with prescribed velocities. The combined shear-compressive loading is realized by applying the real input and output velocities (denoted as V_{input} and V_{output} in Figure 6.2) measured in the combined shear-compression experiments reported in Chapter 5 of this study. In this model, general contact with frictionless tangential behavior is defined for the whole model excluding the contact pairs of rigid planes and tested

honeycomb specimen, which are redefined by surface-to-surface rough contact to make sure that no slippage occurs.
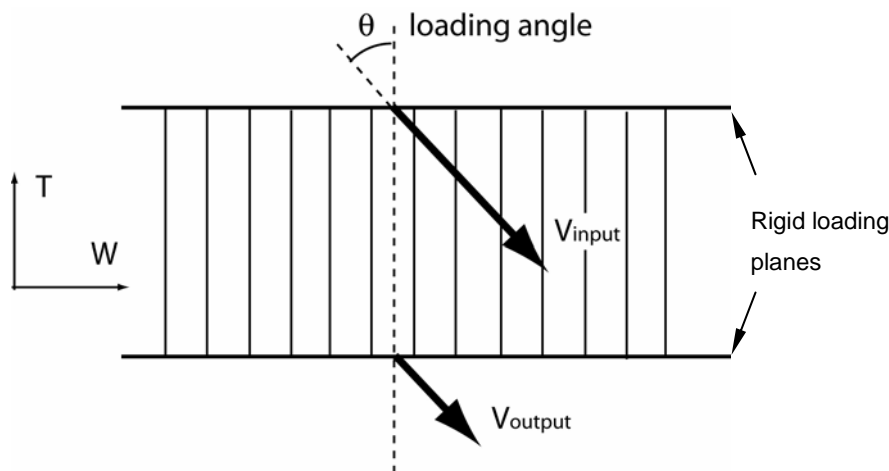
Figure 6.2 Scheme of loading velocities

It is well known that a real honeycomb is always far from perfect; it includes all kinds of imperfections which affect the initial peak value, but have little influence on the crush behavior at a large strain. These imperfections are due to various reasons, like irregular cell geometry, uneven or pre-buckled cell walls, wall thickness variation etc. In this work, we generated the imperfections with different method from the one used in Chapter 2 basing on pre-buckling analysis of the square tube or unit cell models. Here, we preload the perfect specimen uniaxially by 0.1 mm before applying the prescribed experimental velocities. The value of 0.1 mm is chosen to make sure that the simulated initial peak is same as the one from experimental curve at uniaxial compression.

As mentioned before in Chapter 2, the simulations on quasi-static analysis of honeycomb deformation process are completed by ABAQUS/Explicit with the employment of mass scaling technique. Here for the simulations on honeycomb deformation under combined shear-compression by using complete-model, the complex nonlinear effects, e.g. the geometrical and material nonlinearity, the complex contact conditions as well as the local instability during crush are more significant. The adoption of ABAQUS/Standard is more impossible. An alternative is to use also ABAQUS/Explicit + Mass scaling technique for quasi-static problems. The time increment is enlarged to be 100µs, which is larger than the one used in Chapter 2 for sake of calculating efficiency of this large size completed-model. The quasi-static

loading conditions are guaranteed by ensuring the ratio of the kinetic energy to the strain energy as a small value (of the order of 10^{-4}) with the chosen time increment.

A bilinear elasto-plastic material model was employed to describe the cell wall material of this aluminium honeycomb. Because it is difficult to obtain the real foil behavior of honeycomb cell walls, the model parameters of the base material such as yield stress and hardening modulus were determined then by fitting the calculation result of uniaxial compression to the result from experiment (Table 6.1). It should be noticed that the yield stress of the employed bilinear behavior means the intersection of two lines in this model and is different from the usual definition of yield stress from a classical experimental curve. Figure 6.3 shows the comparison between experimental and simulated pressure/crush curves, which validates the parameters of this bilinear material model.

Table 6.1 Bilinear material parameters of 5052 aluminium alloy

Mateiral	Density ρ (kg/m^3)	Young's Modulus E (MPa)	Poission's Ratio v	Yield Stress σ_s (MPa)	Hardening Modulus E_t (MPa)
5052 Aluminium	2700	70	0.35	380	500
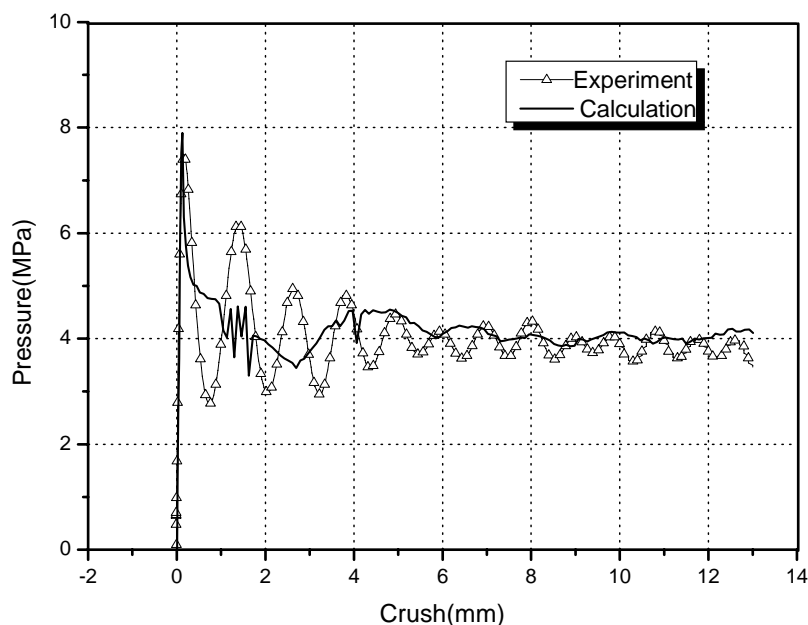
Figure 6.3 Comparison between numerical and experimental results under dynamic uniaxial compression

6.1.2 Simplified models

In order to reduce the calculation cost with this complete honeycomb model, numerical models with various simplifications can be also used. For example, some researchers[1,2] used one-dimensional beam elements with different micro-sections for the simulation of the in-plane behavior, while some others employed one layer of shell element according to the repeated behavior in cell axis direction[3]. As to the out-of-plane behavior, honeycomb specimen was usually simplified into a unit cell or a row of cells because of its periodicity[4]. However, these simplifications may introduce some imprecisions to the numerical model. In order to check the potential errors, two simplified models were also established. By comparing the results of these three models under uniaxial out-of-plane compression, the accuracy of the simplified numerical models will be evaluated.

The so called row-model is made up of a row of cells based on the periodicity of honeycomb specimen in L direction (as shown in Figure 6.4) and will be used to investigate the combined shear-compression behavior of honeycombs in TW plane. The most simplified model consists of three conjoint half walls in *Y* configuration (denoted as cell-model as in Figure 6.4) and can be used only in uniaxial compression to make a comparison with the other two models. The cell-model has been employed in Chapter 2 for investigating the dynamic enhancement of honeycombs, however, it has shortages in appropriately simulating the boundary conditions. Here, it is included in the simulating works to make a comparison with the other two large size models to reveal these shortages. Both of the two simplified models have a length of 25mm in T direction, and the same element size of 0.25mm as in the complete model. The numbers of elements for row-model and cell-model are 28500 and 2100 respectively.

The simplified models work with symmetric boundary conditions. These displacement constraints are applied to the row-model on the two boundaries in L-direction (as shown in Figure 6.4). For the cell-model, symmetric boundary conditions are performed on the three non-intersecting edges of each cell wall in local y-direction (as shown in Figure 6.4). The same method is employed to introduce imperfections into these simplified models.
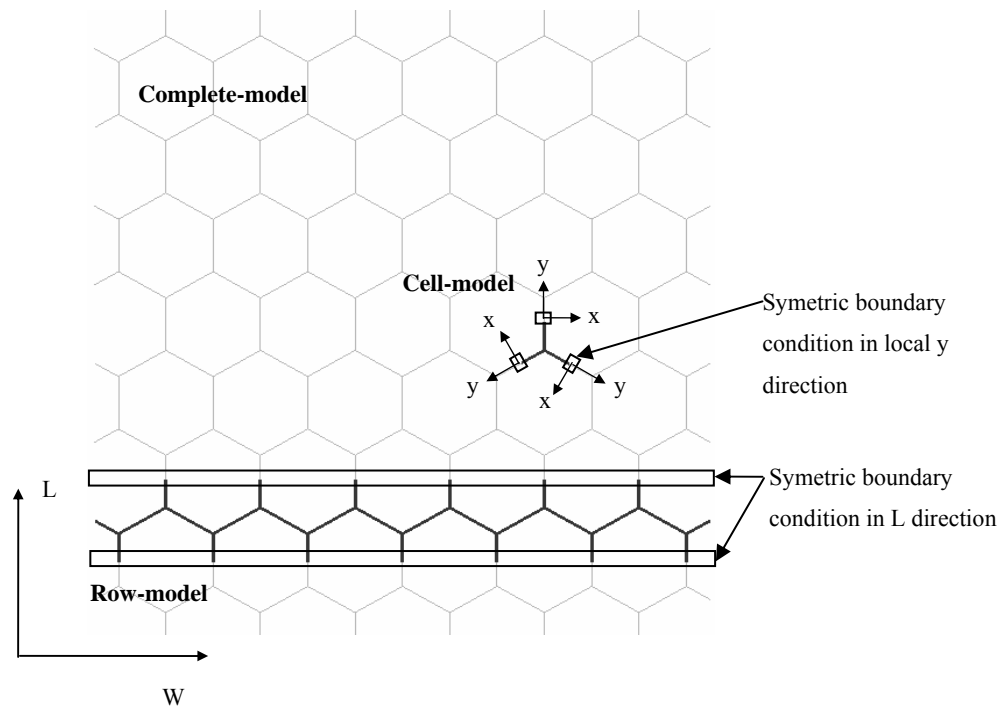
Figure 6.4 Scheme of complete and simplified models
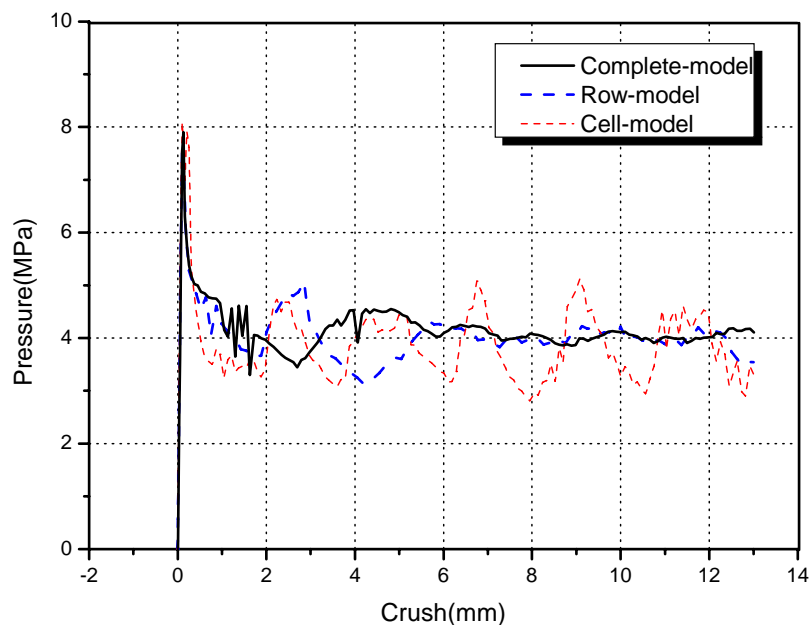
Figure 6.5 Comparison between the calculating results from three models

Figure 6.5 shows the comparison of the pressure/crush curves from three models. The row-model shows a good agreement with the complete-model while the cell-model exhibits significant fluctuations at the plateau stage which is probably due to the application of excessive symmetric boundary constraints. Actually, it is well

known that the crushing behavior of honeycombs under out-of-plane compression is regulated by the successive folding procedure of honeycomb cell walls. With the symmetric boundary condition on three non-intersecting edges, the cell-model is actually equivalent to a honeycomb specimen consisting of repeated cells with identical deforming procedure, which results in strictly simultaneous collapse of all the honeycomb cells. Thus, in the pressure/crush curve, each fluctuation represents one fold formation of the cell wall in honeycomb microstructure. For the large size model, the neighboring cells interact with each other while forming the folds and reach their local peak value at different instants, which makes the macroscopic resulting curves smoother.

As a conclusion, the cell-model has some shortages in properly simulating the boundary conditions and fails to calculate the honeycomb multi-axial behavior. The use of this model in Chapter 2 aims at understanding the deformation process of basic *Y* configuration in honeycomb and at the explanation of the dynamic enhancement mechanism. Thus, the effects of boundary conditions are less concerned. Although an ideal model should be of the same dimensions as the tested specimen, considering the contributions of simplified models in reducing the time-expense of calculation, we finally chose the row-model for the subsequent calculations on the biaxial behavior of honeycombs under combined shear-compression.

6.2 Comparison between numerical and experimental results

In this section, the results of honeycomb under combined out-of-plane shear-compression (in TW plane) simulated with row-model are presented. It includes four loading angles of 30°, 40°, 50° and 60° and both dynamic and quasi-static loading cases. A good agreement between the calculating results and the experimental one in terms of overall pressure/crush curves and deformation patterns is found for most of the loading cases.

6.2.1 Comparison on pressure/crush curves

6.2.1.1 Definitions

The overall pressure/crush curves are obtained from the calculated results in order to make a comparison between the experiments and the simulations. It is worth emphasizing that the variable *crush* is defined in Chapter 5 as the relative displacement component of the two moving bevels in X_3 direction and the *pressure* as the X_3 force component divided by specimen cross-sectional area S_s. As a consequence, in the case of numerical combined shear-compression test, the pressure $P(t)$ is calculated by dividing the contact force component in the rigid planes moving direction (X_3 direction in Figure 6.6) with specimen area S_s. Its relationship with the directly obtained normal and shear contact forces is as follow:

$$P(t) = (F_n(t)\cos\theta + F_s(t)\sin\theta)/S_s \qquad 6.1$$

where θ is the loading angle as defined in Chapter 4, $F_n(t)$ and $F_s(t)$ are respectively the normal and shear contact forces at the interfaces of honeycomb specimen and rigid loading planes.

The overall crush $\Delta(t)$ is derived from the relative resultant displacement of the two reference points on rigid planes (Figure 6.6). It has simple relationship with the normal and shear crushes (denoted as $d_n(t)$ and $d_s(t)$), which is:

$$\Delta(t) = d_n(t)/\cos\theta = d_s(t)/\sin\theta \qquad 6.2$$
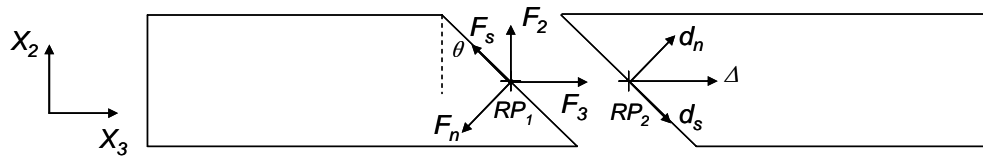
Figure 6.6 Scheme of the decompositions of force and crush

6.2.1.2 Comparison of dynamic results

Figure 6.7 presents the experimental and calculated pressure/crush curves under dynamic uniaxial compression and combined shear-compression for a loading angle $\theta=50^o$. Each curve has two distinct stages. During stage I (from the beginning of zero crush to the position of the initial peak as defined in Chapter 5), the slopes of elastic segment are in good agreement for the calculations and the experiments. In addition, with the employed magnitude of imperfection, the initial peak of the calculated curve also agrees well with the experiment. During stage II (defined as the following crush

period after stage I to 13mm crush), the experimental curves have more fluctuations than the calculated ones, but the average strength is rather correct.
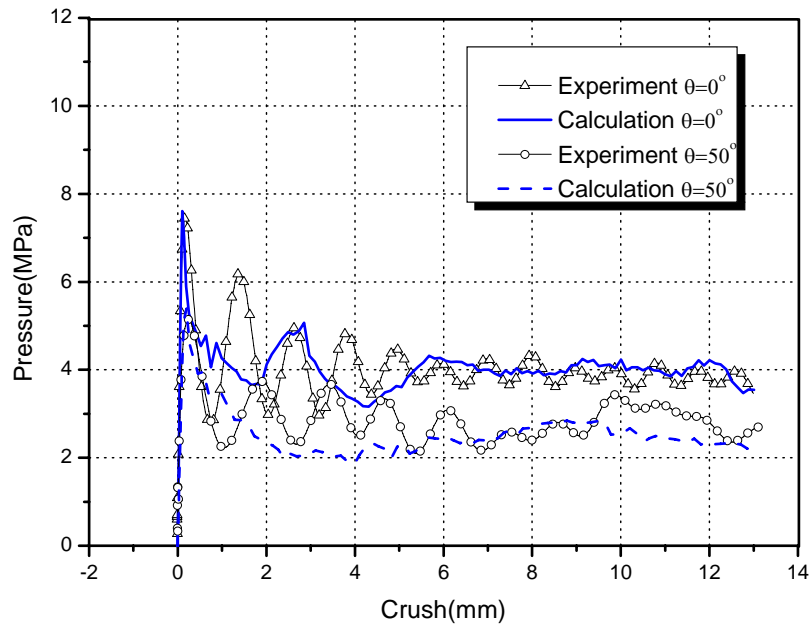
Figure 6.7 Comparison of the dynamic pressure/crush curves from calculations and experiments

A comparison between the initial peak value as well as the average strength for every loading angle is described in Figure 6.8. The average strength is defined as the curve area (absorbed energy) of this plateau stage divided by the corresponding crush length (the same formulas as used for experimental curves (Equation 5.1 in Chapter 5):

$$\overline{p} = \frac{1}{\delta_{max} - \delta^*} \int_{\delta^*}^{\delta_{max}} p d\delta \qquad 6.3$$

where δ^* denotes the crush value at the initial peak for each of the overall pressure/crush curve. δ_{max} is the maximum crush.

A maximum difference of 4.9% between the simulation and the experiment is found for the initial peak at loading angle of 50°. For the average strength, the deviation from experiment is a little more significant at larger loading angles.
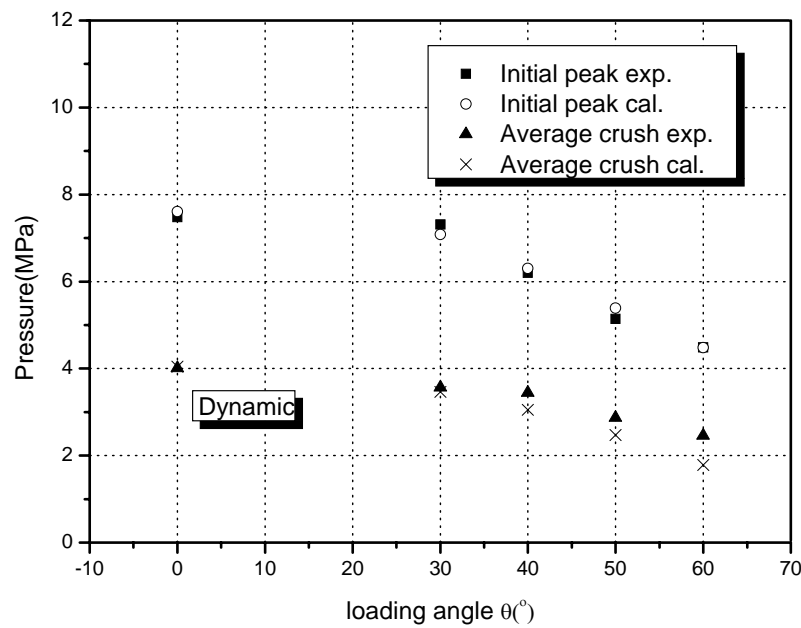
Figure 6.8 Comparison of the initial peak and average strength between dynamic calculations and experiments at various loading angles

6.2.1.3 Comparison of quasi-static results

The quasi-static virtual testing results for uniaxial compression and combined shear-compression at loading angle $\theta=50^{o}$ are compared in Figure 6.9 together with the experimental curves. The numerical results show a good correlation with the experimental ones at the crushing stage II. The average strengths are calculated for all the loading angles and listed in Figure 6.10. The maximum difference of 13.2% is found at loading angle of 40°. Nevertheless, during stage I of the curves, a clear difference is found for both the ascending segment slope and the initial peak value that can be attributed to a slight slippage between specimen and bevels at the beginning of the experiment.
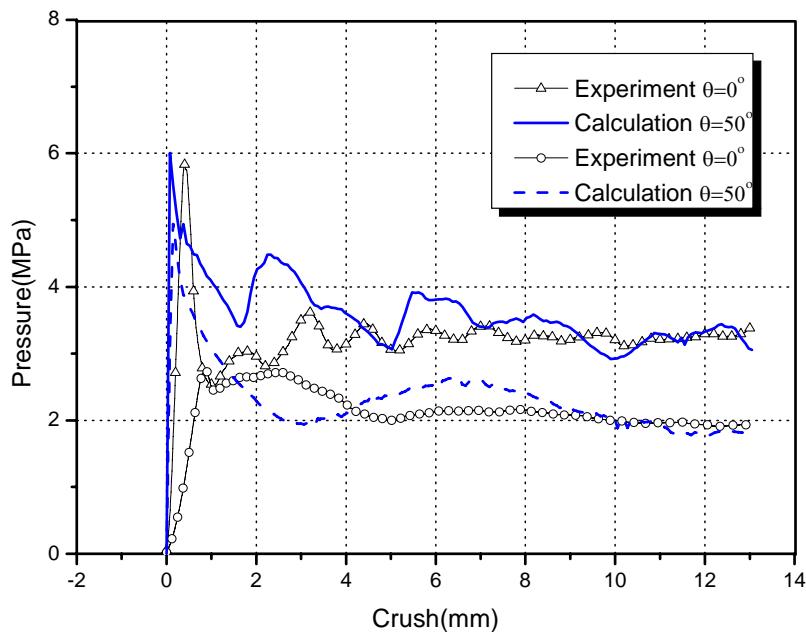
Figure 6.9 Comparison of the quasi-static pressure/crush curves from calculation and experiments
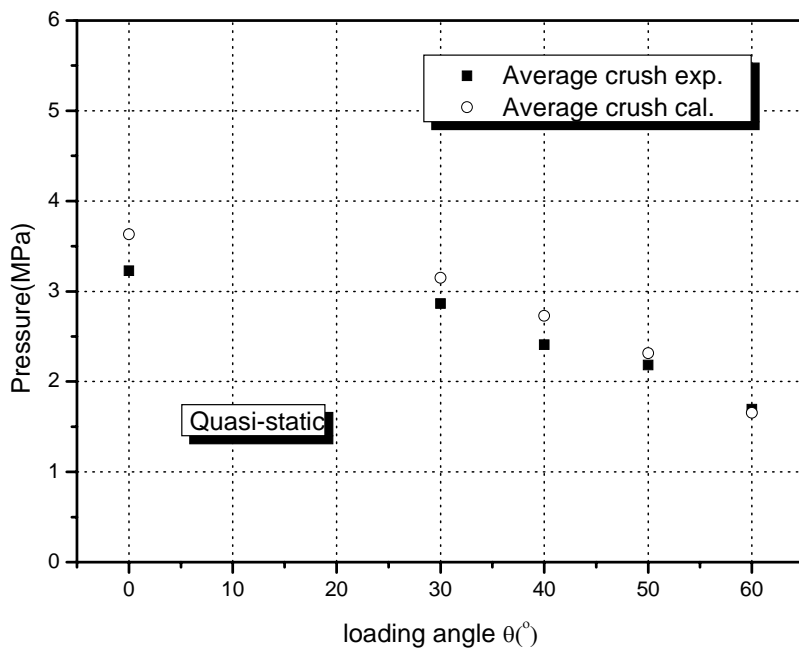
Figure 6.10 Comparison of average strength between quasi-static calculations and experiments at various loading angles

6.2.2 Comparison on deformation patterns

Furthermore, the simulated deforming pattern of honeycombs under combined shear-compression during stage II is also compared with the experimental observations obtained with high speed camera. Figure 6.11(a) and (b) show the specimens at dynamic loading of $\theta=30^o$ and at crush of 12mm, and Figure 6.11 (c) and (d) for the quasi-static loading of $\theta=50^o$. It can be seen that the cell wall axis of all the displayed specimens incline during the crushing processes, and the inclined directions of the virtual and real specimens are in parallel to each other for the two different loading angles. Besides, the phenomenon of two-side folding system is also found in the numerical results as discovered for most of the experimental shear-compression specimens.
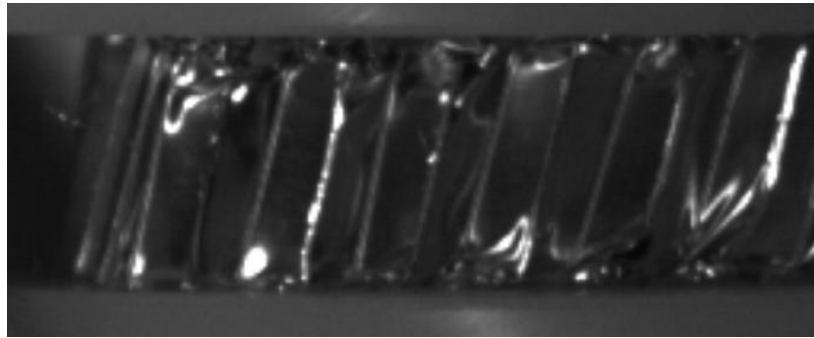
(a)
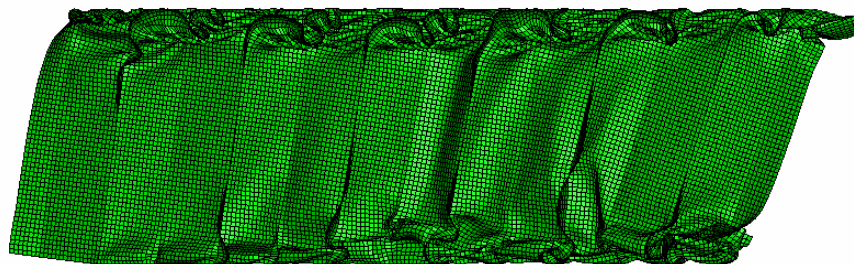
(b)
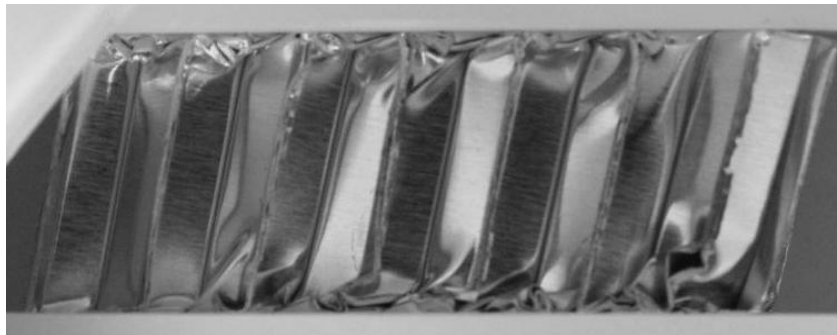
(c)
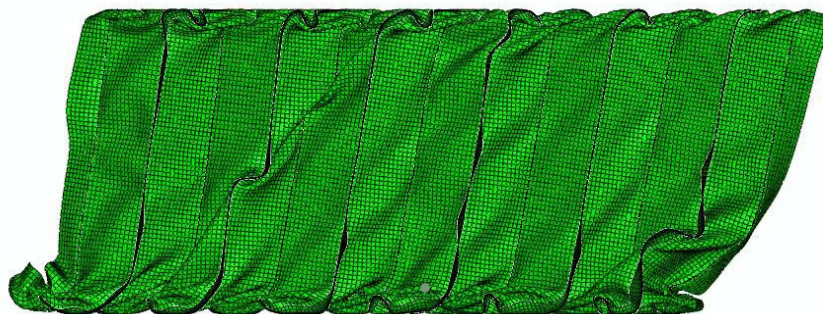
(d)

Figure 6.11 Comparison of deformation configurations of experimental ((a) and (c)) and calculating ((b) and (d)) honeycomb specimens under dynamic (θ=30° (a) and (b)) and quasi-static combined shear-compression.

In the combined shear-compression experiments for honeycombs in Chapter 5, we found two co-existing deformation modes (rotation of cell axis or not) even for the same loading conditions. However, the numerical result can not cover at the same time the two deforming modes as in experiments. Figure 6.12 illustrates the rotation angle β at 40% nominal compressive strain for every loading angle. It appears that our numerical specimen have a clear preference for the deforming mode with significant cell axis rotation.
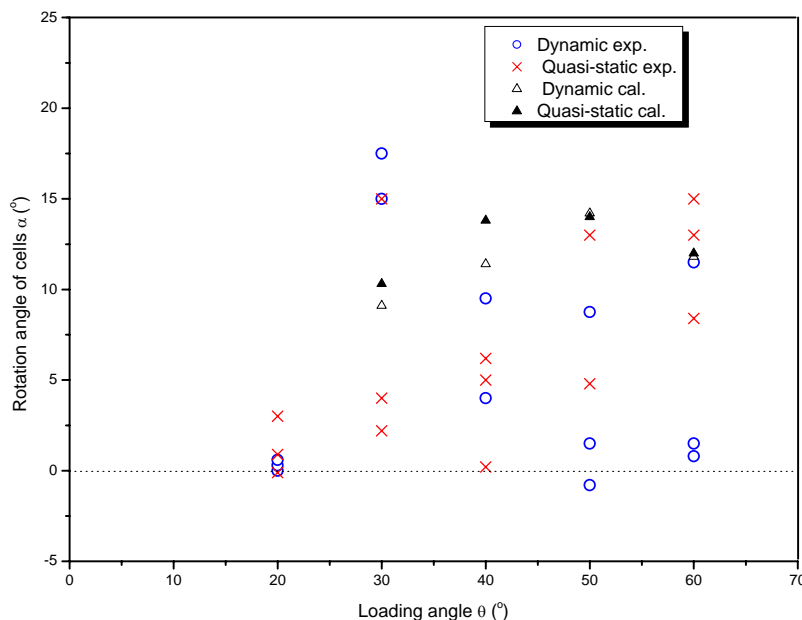
Figure 6.12 Comparison of the cell axis rotation at every loading angle from both experiments and simulations

6.3 Biaxial behavior of honeycombs under combined shear-compression

6.3.1 Normal and shear behaviors

The validation of the simulation work in Section 6.2 shows that the virtual testing results can represent well the experimental ones with the exception of quasi-static initial peak values. These virtual combined shear-compression tests provide more information than the real experiments and enable us to study separately the normal and shear behaviors of honeycombs.

The separated normal and shear pressure/crush curves under dynamic loading are shown in Figure 6.13(a) and (b) respectively. It is noted that the normal and shear pressures are calculated from the normal and shear contact forces ($F_n(t)$ and $F_s(t)$) at the interfaces between rigid loading planes and honeycomb specimen. For the sake of clarity, only 0° (not included in shear behavior), 40° and 60° are displayed.

It is observed in Figure 6.13(a) that the level of normal pressure/crush curves decreases when the loading angle increases. The shear behaviors are generally weaker than the normal ones (as shown in Figure 6.13(b)) and their initial peak becomes inconspicuous with respect to the succeeding plateau. The level of the shear curves at the plateau stage increases with increasing loading angle, which shows an opposite trend to normal behavior.

It is worthwhile to recall that the change of the loading angle in experiment modifies not only the ratio between normal and shear loadings but also the measured axis force component. Here in this numerical test, such an ambiguity is eliminated because we measured directly the normal and shear strengths. The results shown in Figure 6.13 do mean a lower resistance of honeycomb structure to compression under an increasing additional shear.
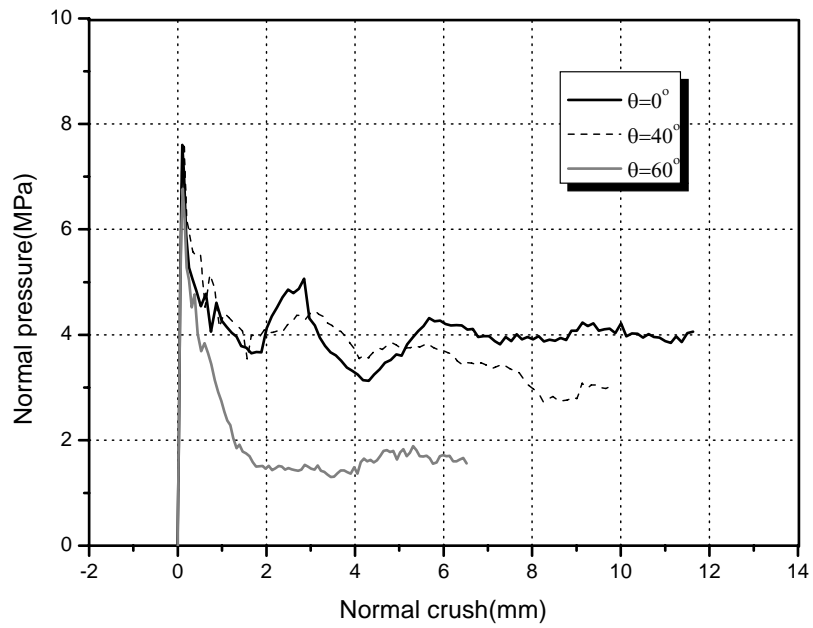
(a)
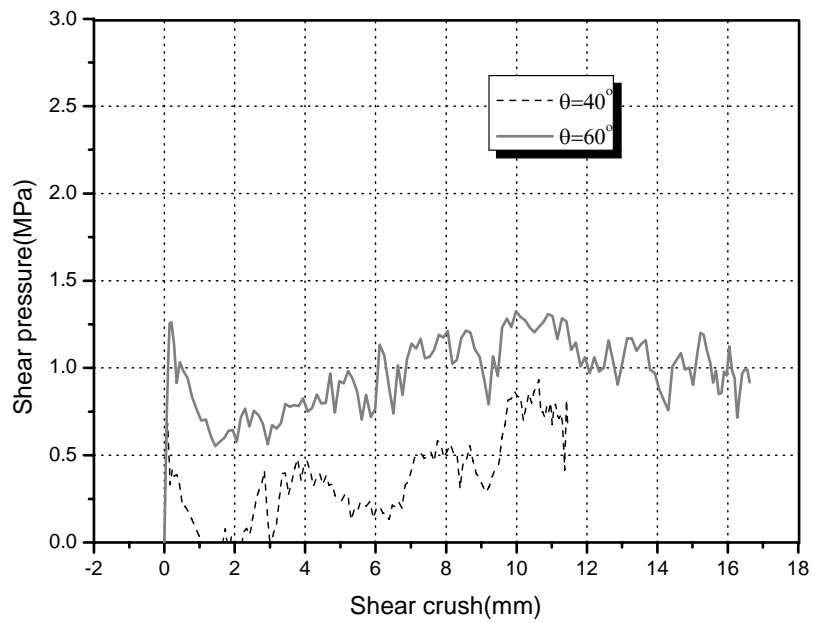
(b)

Figure 6.13. Normal (a) and shear (b) behaviors of honeycomb under dynamic combined shear-compression

6.3.2 Dynamic enhancement of normal and shear behaviors of honeycombs

Under quasi-static loading, the normal and shear pressure/crush curves show a great similarity to the dynamic ones, i.e. the normal strength decreases with the loading angle whereas the shear strength increases.

It is recalled that the dynamic enhancement of honeycombs under uniaxial compression has been investigated in detail both numerically and experimentally in Chapter 2 and Chapter 3. The overall pressure/crush curves of honeycombs under combined shear-compression shows also an obvious enhancement at higher loading velocity. Here, for the separated normal and shear behaviors of honeycombs, a comparison between the quasi-static and the dynamic curves shows that the loading rate will also affect the normal and shear behaviors of honeycombs under combined shear-compression. Figure 6.14 displays the dynamic and quasi-static normal and shear curves at θ=40$^\text{o}$ and an enhancement is found for both of the two groups of curves.
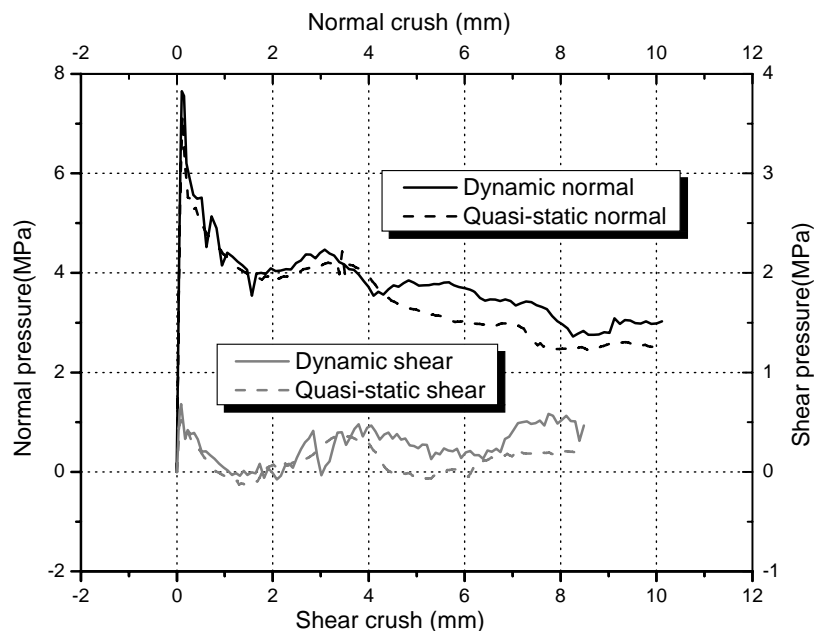
Figure 6.14 Comparison between dynamic and quasi-static normal and shear pressure/crush curves at loading angle of 40$^\text{o}$

The average strengths of normal and shear behaviors were calculated for both dynamic and quasi-static loading at every loading angle. All these average values are

collected in Figure 6.15, which shows clearly the change of the normal and shear strengths along with the loading angle as well as a strength enhancement under impact loading for every loading angle.
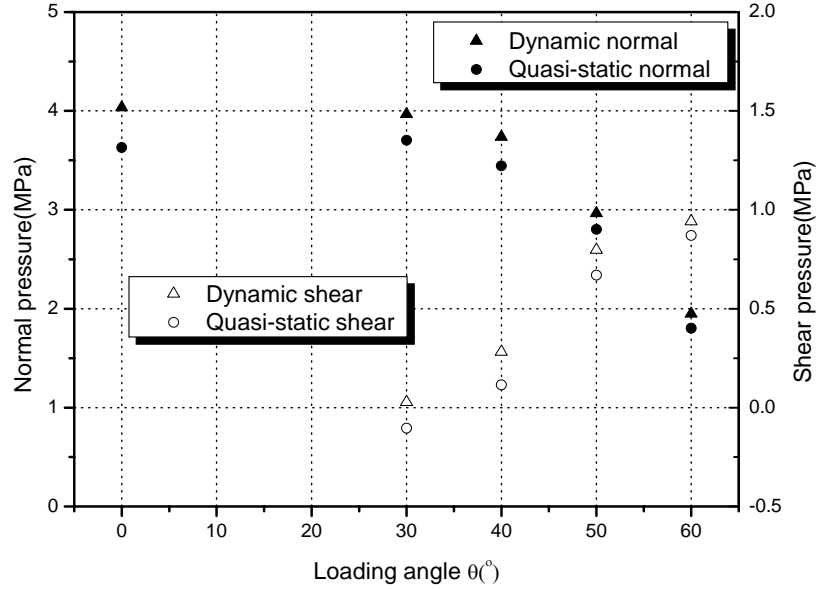
Figure 6.15 Comparison between dynamic and quasi-static normal and shear pressure vs. loading angle

6.3.3 Macroscopic yield envelop estimation

Figure 6.16 shows the distribution of calculated honeycomb biaxial behavior during stage II on the normal average strength vs. shear average strength plane. An elliptical shape is found for both the quasi-static and dynamic loading cases (Equation 6.4).

$$\left(\frac{\sigma}{\sigma_0}\right)^2 + \left(\frac{\tau}{\tau_0}\right)^2 = 1 \qquad\qquad 6.4$$

where σ_0 and τ_0 are respectively the normal strength under uniaxial compression and the shear strength under pure shear loading. By fitting the data with Levenberg-Marquardt algorithm (LMA), these two parameters are identified to be 3.98MPa and 1.11MPa under dynamic loading and 3.57MPa and 1.02MPa under quasi-static loading.

It is found in Figure 6.16 that the expansion of the crush envelope from the quasi-static loading to the dynamic loading is almost isotropic, even though the normal strength/shear strength ratio for a given loading angle is different under quasi-static and dynamic loading. It means that the dynamic biaxial strength for this honeycomb might be derived by using the enhancing ratio of uniaxial compression and the quasi-static crush envelope.
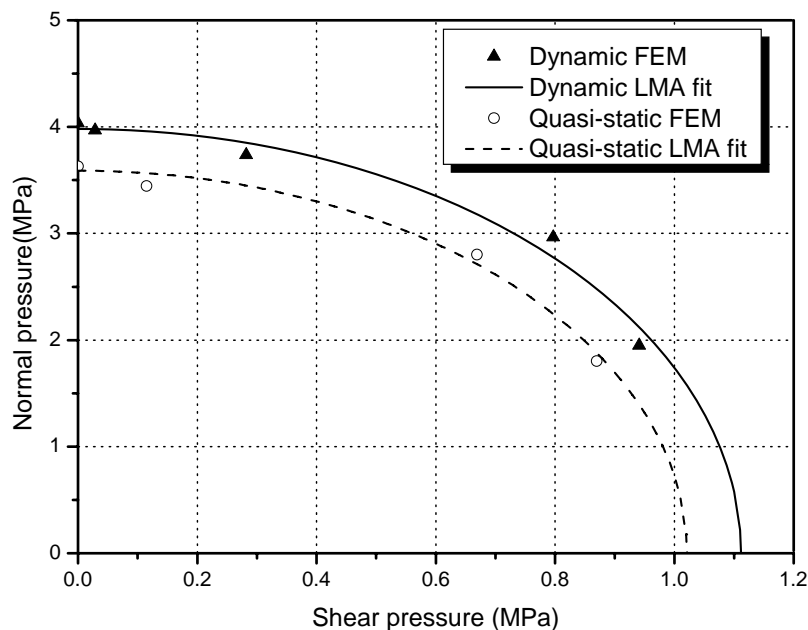
Figure 6.16 Crushing envelopes of honeycomb in normal strength vs. shear strength plane

6.4 Summary

This chapter reproduced the combined shear-compression experiments of honeycombs in Chapter 5 by means of FEM.

In Section 6.1, three numerical models with different simplifications were presented and compared. Row-model with reasonable calculating expense and accurate boundary simulation was finally chosen to perform the combined shear-compression virtual experiments of honeycombs in TW loading plane.

Section 6.2 presented the calculating results of row-model at every loading angle under both dynamic and quasi-static loadings. The calculating results are in good agreement with the experimental ones in terms of deforming mode and the overall pressure/crush curves, which are the final information obtained from the new designed combined shear-compression experiments.

Such numerical virtual tests enabled to separate the normal and shear behaviors of honeycombs as done in Section 6.3. It shows that the strength of honeycombs under compression is largely affected by the additional shear loading and exhibits a significant decrease while increasing shear loading. An obvious enhancement is also observed at dynamic loading for both normal and shear behaviors with respect to the quasi-static case at every loading angle. In order to describe the dynamic and quasi-static biaxial behaviors of honeycombs at macroscopic level, an elliptical criterion in the plane of normal strength vs. shear strength can be derived with a set of parameters obtained by fitting the data with Levenberg-Marquardt algorithm. The expansion of the crush envelope with loading rate happened to be isotropic for this studied honeycomb in combined out-of-plane shear-compression.

The numerical method proposed in this chapter works as a complementary means to the experiments presented in Chapter 5. It overcomes the limitation of experimental method in separating normal and shear behavior and provide a new method for investigating the multi-axial behavior of cellular materials with the combination of experimental study and FEM analysis.

References

[1]   S. D. Papka, S. Kyriakides. In-plane biaxial crushing of honeycombs-Part II: Analysis. Int. J. Solids Struct. 36, 4397-4423 (1999).

[2]   A. Hönig, W. J. Stronge. In-plane dynamic crushing of honeycombs. Part I: crush band initiation and wave trapping. Int. J. Mech. Sci. 44, 1665-1696 (2002).

[3]   Z. Zou, S. R. Reid, P. J. Tan, S. Li, J. J. Harrigan. Dynamic crushing of honeycombs and features of shock fronts. Int. J. Impact Eng. 36, 165-176 (2009).

[4]   D. Mohr, M. Doyoyo. Deformation-induced folding systems in thin-walled monolithic hexagonal metallic honeycomb. Int. J. Solids and Struct. 41, 3353-3377 (2004).

Chapter 7 Conclusions

This study performed a series of investigations on the dynamic response of honeycombs under combined shear-compression, in order to address the energy absorbing problems in accidental crash or impact events in aerospace and automobile industries,

The whole study mainly consists of two parts. The first part aims at the dynamic enhancement mechanism of honeycomb strength under uniaixial compression. Chapter 2 and Chapter 3 are involved in this part.

In Chapter 2, we installed three thin-walled models for investigating their dynamic enhancement, and the adaptability of an inertia effect model in the micro-size thin-walled structures is validated. The main idea for the inertia effect model in enhancing the strength of thin-walled structure under dynamic loading is summarized as follow: the plastic collapse of thin-walled structure is an unstable buckling deformation process, which will be delayed by lateral inertia effect under dynamic loading. In this delayed duration, the structure is compressed further in axial direction, and results in a higher strain before the collapse occurs; moreover, if the base material is with strain hardening behavior, the stress as well as the loading capacity of the thin-walled structure will be elevated. The influence of base material strain hardening exponent on the dynamic enhancement rate is investigated, and an increasing trend is found in the micro-size tube model, which is in good agreement with the proposed mechanism. The geometric parameters such as cell-size and cell-wall thickness of honeycomb also have influences on the dynamic enhancement.

Chapter 3 studied the phenomenon of dynamic enhancement of honeycombs under moderate impact velocity experimentally. The influences of geometric parameters (including cell-size and cell-wall thickness) and the strain hardening behavior of base material on the strength enhancement of honeycombs under dynamic loading were investigated. It is found that the change of cell-size affects the dynamic strength enhancement for the tested honeycombs, and the fact that the dynamic enhancement rate of large cell honeycomb is much higher than the one of small cell is mainly due to the decrease of honeycomb strength by enlarging the cell-size. The thick wall honeycomb has much bigger strength enhancement $\Delta \overline{p}$ than the one of thin wall honeycomb, however, considering the higher strength of thick cell-wall

honeycomb, the dynamic enhancement rate as illustrated before shows no big difference for these two cases. Beside, the base material has also significant influence on the dynamic enhancement of honeycombs.

The second part of this study refers to a new designed biaxial loading device with the use of a large-diameter Nylon Split Hopkinson Pressure Bar system (SHPB). The biaxial behavior of honeycombs under combined shear-compression is investigated with the combination of experimental works and simulations. Chapter 4, 5 and 6 are included in this part.

In Chapter 4, the new designed dynamic biaxial loading device was presented as well as the validating work by full-size FEM simulation of the loading process. Two short beveled bars were introduced into the classical SHPB system to achieve the combined shear-compressive loading. The validation work by means of FEM analyses indicated that the force and velocity components in the axial direction of the pressure bar for foam-like specimen under combined shear-compression can be well measured from Hopkinson bar and the possible errors induced by the bevels is rather small to be neglected.

Chapter 5 showed the experimental results on 5052 aluminium honeycombs by using this biaxial loading device. The biaxial behaviors and deformation modes of honeycombs under different combined shear-compression loading states were obtained and the influences of loading angle on honeycombs biaxial loading response and deformation mechanism were analyzed. The main conclusions of these combined shear-compression tests are summarized: (1) The obtained dynamic and quasi-static pressure/crush curves show that both the initial peak value and the average plateau strength decrease significantly with increasing loading angle. (2) The behavior of honeycombs under combined shear-compression in respective TW and TL planes are close to each other. (3) An obvious enhancement of both the initial peak value and the average plateau strength is found for dynamic curves compared to quasi-static ones at every loading angle.

Chapter 6 tried to describe the biaxial behavior of honeycombs by FEM simulations. Row-model with reasonable calculating expense and accurate boundary simulation could be chosen to perform the combined shear-compression virtual experiments of honeycombs in TW loading plane. The calculating results from the detailed honeycomb models were ensured to be in good agreements with the experimental results in terms of overall pressure/crush curves and defamation modes.

Basing on the calculation results, the separated normal and shear behaviors of honeycomb under combined shear-compression as well as the macroscopic crush envelope were obtained. It shows that the strength of honeycombs under compression is largely affected by the additional shear loading and exhibits a significant decrease while increasing shear loading. An obvious enhancement is also observed at dynamic loading for both normal and shear behaviors with respect to the quasi-static case at every loading angle. An elliptical criterion in the plane of normal strength vs. shear strength can be derived with a set of parameters obtained by fitting the data with Levenberg-Marquardt algorithm. The expansion of the crush envelope with loading rate happened to be isotropic for this studied honeycomb in combined out-of-plane shear-compression.